ROYAUME DU MAROC
Université Mohammed V
- RABAT -
جامعة محمد الخامس
– الرباط –
Faculté des sciences
كلية العلوم

CENTRE D'ETUDES DOCTORALES - SCIENCES ET TECHNOLOGIES

N° d'ordre :3354

THESE

En vue de l'obtention du : ***DOCTORAT***

Structure de Recherche : **Laboratoire de Matière Condensée et Sciences Interdisciplinaires**
Discipline : Physique
Spécialité : Sciences et ingénierie des matériaux

Présentée et soutenue le 24/10/2020 par :

YASSINE RAOUI

Computational Design of Organic-Inorganic perovskite solar cells through drift-diffusion simulation and processes fabrication.

JURY

Abdelilah BENYOUSSEF	PES, FS, Université Mohammed V, Rabat	Président
Hamid EZ-ZAHRAOUY	PES, FS, Université Mohammed V, Rabat	Directeur de Thèse
Abdallah EL KENZ	PES, FS, Université Mohammed V, Rabat	Rapporteur /Examinateur
Abdelmajid AINANE	PES, FS, Université Moulay Ismaïl, Meknes	Rapporteur /Examinateur
Ismail ESSAOUDI	PES, FS, Université Moulay Ismaïl, Meknes	Rapporteur /Examinateur
Noureddine MASAIF	PES, FS, Université Ibn Tofail, Kénitra	Examinateur

Année Universitaire : 2020-2021

Dedicate

This work dedicated to my lovely brother, **Bouchaib**, who has been a constant source of support and encouragement. I am genuinely profoundly thankful to my God for having you in my life. This work is dedicated to **my parents,** who have loved me unconditionally, especially my **lovely mother,** who has taught me to work hard and be patient to achieve my goals.

Remerciements

Ce travail a été réalisé au sein du Laboratoire de Matière condensé et sciences interdisciplinaire de la Faculté des Sciences de Rabat-Maroc sous la direction de Monsieur le professeur HAMID EZ-ZAHRAOUY en collaboration avec le Basque Centre on Material, applications and Nanostructures-Spain.

Je tiens tout d'abord à exprimer ma gratitude la plus profonde au professeur **HAMID EZ-ZAHRAOUY,** Professeur de l'Enseignement Supérieure à la Faculté des Sciences de Rabat, pour avoir accepté la direction de ma thèse et ses efforts durant mon travail.

Je suis très sensible à l'honneur que m'a fait Monsieur **ABDELILAH BENYOUSSEF** , Professeur de l'Enseignement Supérieur à la Faculté des Sciences, Université Mohammed V, Rabat , en acceptant la présidence du jury .

J'aimerais ensuite remercier Monsieur **ABDALLAH EL KENZ** pour l'intérêt qu'il a porté à ce travail et aussi pour avoir de consacré une partie de son temps à l'analyse de mon travail en tant que rapporteur et examinateur.

Je tiens à remercier Monsieur **ABDELMAJID AINANE**, Professeur d'enseignement supérieur à l'Université Moulay Ismaïl Meknès– Maroc, d'avoir accepté de participer à ce jury , en tant que rapporteur et examinateur.

Je tiens à remercier Monsieur **ISMAIL ESSAOUDI**, Professeur d'enseignement supérieur à l'Université Moulay Ismaïl Meknès– Maroc, d'avoir accepté de participer à ce jury , en tant que rapporteur et examinateur.

Je tiens à remercier Monsieur **NOUREDDINE MASAIF**, Professeur d'enseignement supérieur de la faculté des Sciences Kénitra-Maroc, d'avoir accepté de participer à ce jury , en tant que examinateur.

Je tiens aussi de remercier le Ikerbasque Professeur **SHAHZADA AHMED** et Dr.**SAMRANA KAZIM** à BCMaterials pour leur orientations afin de développer mon travail et leur remarques et qualités professionnelles et humaines.

Je tiens aussi de remercier Dr.**OMAR EL BOUNAGUI** et Dr.**NAJIM TAHIRI** à la faculté des sciences de Rabat pour leur soutien durant mon travail.

Enfin, je ne saurais oublier mes collègues du Laboratoire de Matière Condensée et Sciences Interdisciplinaires au Maroc ou du l'institut BCMaterials à l'Espagne.

Je veux aussi remercier ma famille pour m'avoir constamment soutenue tout au long de ces années.Un grand merci pour tout qui m'ont aidé de soutenu et j'omis de citer les noms.

Merci encore à tous.

YASSINE RAOUI

Acknowledgments

First and foremost, I am thankful to ALLAH, the most beneficent and the Most Merciful, who helped me by gracing his blessing on me.

This work was carried out within the Laboratory of Condensed Matter and Interdisciplinary of Sciences at Faculty of Sciences -Rabat-Morocco under the direction of Professor **HAMID EZ-ZAHRAOU**Y in collaboration with the Basque Center on Material, Applications and Nanostructures -Bilbao- Spain.

I would like to express my sincere gratitude to my supervisor Professor **HAMID EZ-ZAHRAOUY** for his inspiration, continuous support, advice, and guidance to achieve my goals during my work.

I am thankful for the honor made to me by Professor **ABDELILAH BENYOUSSEF** for accepting the presidency of the jury.

I would then like to thank Professor **ABDALLAH EL KENZ**, as rapporteur an examiner for my work, and also for having devoted part of his time to the analysis of my work.

I would like to thank Professor **ABDELMAJID AINANE**, for agreeing to participate in this jury, as rapporteur and examiner.

I would like to thank Professor **ISMAIL ESSAOUDI**, for agreeing to participate in this jury, as rapporteur and examiner.

I would like to thank Professor **NOUREDDINE MASAIF**, for having accepted to participate in this jury, as rapporteur and examiner.

I warmly thank the Professor **SHAHZADA AHMAD** from BC-Materials-Spain for his support, help, and motivation, for his encouragement to face the challenges and mentoring how to deal with it.

I am deeply thankful to Dr. **SAMRANA KAZIM** from BC-Materials-Spain for her motivation, guidance, and her help in revising my papers during my Ph.D. Her continues support for my research and critical and constructive comments polished my knowledge and research skills. She has always been very cooperative during my whole study.

I would like to thank Dr.**OMAR EL BOUNAGUI** and Dr.**NAJIM TAHIRI** at Faculty of Sciences - Rabat for their support.

I cannot forget my colleagues from the Laboratory of Condensed Matter and Interdisciplinary of Sciences in Morocco or from the Institute of BCMaterials in Spain.

Thanks to all,

Yassine RAOUI

ABSTRACT

A major global issue that the world is facing today is the upcoming depletion of fossil fuels and the energy crisis. The development of a clean source of renewable energy for harvesting light energy to electricity becomes an urgent need. Perovskite solar cells (PSCs) have attracted tremendous attention during the last ten years; the power conversion efficiency has seen a vast improvement from 2.2 % to more than 25 %. However, the performance is far from the Shockley-Queisser Limit.

The first part of this thesis focuses on the drift-diffusion simulation of organic-inorganic PSCs based on $MAPbI_3$ as harvest light. The second part of this work investigated the decreasing recombination rate at interface layers of PSCs by designing a new optimum band offset, which could deliver 26.56% efficiency using $(FAPbI_3)_{0.85}(MAPbBr_3)_{0.15}$ as absorber layer with the fabrication process of all layers.

The third line of this work concentrated on boosting the performance of inorganic PSCs using $CsPbI_2Br$ and $CsSnI3_{-x}Br_x$ as inorganic and ecofriendly active layers, respectively, for the first time through drift-diffusion simulation.

This thesis proposed an experimentally efficient electron transport layer based on SnO_2: Cs_2CO_3 to address the challenge of misalignment in PSCs. The fabrication processes of P-i-N all-inorganic PSCs based on $CsPbI_2Br$ and drift-diffusion simulation have also been investigated.

Keywords: Devise Simulation, Drift-Diffusion, Perovskite Solar Cells, $MAPbI_3$, $(FAPbI_3)_{0.85}(MAPbBr_3)_{0.15}$, $CsSnI_{3-x}Br_x$, $CsPbI_2Br$, Device Fabrication.

Résumé

L'épuisement imminent des conductibles fossiles constitue actuellement un véritable problème auquel le monde entier doit y faire face. Les cellules solaires à base de matériaux pérovskites (PSCc) ont attiré vivement l´attention de plusieurs chercheurs à travers le monde au cours de la dernière décennie.

Cette thèse a pour objectif principal de proposer la mise en œuvre d'une couche efficiente pour le transport des électrons dans les PSCc afin d'éviter le désalignement dans les cellules photovoltaïque à base de pérovskites. De même, sur la base de la simulation numérique des courants de dérive et de diffusion, considérée comme première au monde, nous fabriquons une cellule solaire P-i-N à base de matériau inorganique type $CsPbI_2Br$.

La première partie porte sur la simulation des courants de dérive et de diffusion connue sous le nom ‘‘drift-diffusion model’’ en utilisant le logiciel SCAPS pour étudier et analyser l'efficacité des PSCc à base de $MAPbI_3$ comme absorbeur de la lumière.

La deuxième partie est axée essentiellement sur l'étude de la diminution du taux de recombinaison au niveau des couches d'interface des PSCc, qui pourrait fournir une efficacité de 26 .56% en employant $(FAPbI_3)_{0,85}(MAPbBr_3)_{0,15}$ comme couche absorbante. Un procès de fabrication des couches est adapté également dans cette étude.

La troisième partie est réservée à la simulation numérique du modèle ‘’drift-diffusion’’ afin d'augmenter le rendement des inorganiques PSCc, en utilisant $CsPbI_2Br$ et $CsSnI_{3-x}Br_x$ comme des couches actives.

Mot clés : Simulation ,Drift-diffusion ,SCAPS, Cellules solaires , Matériaux pérovskites (PSCs), $MAPbI_3$, $(FAPbI_3)_{0,85}(MAPbBr_3)_{0,15}$, $CsSnI_{3-x}Br_x$, $CsPbI_2Br$, Fabrication

Résumé détaillé

L'épuisement imminent des conductibles fossiles constitue actuellement un véritable problème auquel le monde entier doit y faire face. Ainsi, le développement d´une source propre d´énergie renouvelable permettant la conversion directe photons-électrons devient une nécessité urgente. Les cellules solaires à base de matériaux pérovskites (PSCc) ont attiré vivement l´attention de plusieurs chercheurs à travers le monde au cours de la dernière décennie. En effet, plusieurs travaux théoriques et expérimentaux, allant du massif au nanoparticule, ont été développés pour l'amélioration du rendement de la cellule photovoltaïque. Ces travaux ont donné lieu à une amélioration importante du rendement allant de 2.2 % à plus de 25% dans les dix dernières années. Cependant, malgré les efforts énormes déployés par la communauté scientifique dans ce domaine, ils existent encore des problèmes à résoudre, tels que la minimisation du cout, stabilisation des matériaux utilisés, augmentation de la durée de vie de la cellule, amélioration du rendement et ajuster le dimensionnement.

Cette thèse a pour objectif principal de proposer la mise en œuvre d'une couche efficiente pour le transport des électrons dans les PSCc afin d'éviter le désalignement dans les cellules photovoltaïque à base de pérovskites. De même, sur la base de la simulation numérique des courants de dérive et de diffusion, considérée comme première au monde, nous fabriquons une cellule solaire P-i-N à base de matériau inorganique type $CsPbI_2Br$.

Pour ce faire, le travail de cette thèse est composé de trois parties essentielles:

La première partie porte sur la simulation des courants de dérive et de diffusion connue sous le nom ‘‘drift-diffusion model’’ en utilisant le logiciel SCAPS pour étudier et analyser l'efficacité des PSCc à base de $MAPbI_3$ comme absorbeur de la lumière , on comparant le rendement des couches de transport des électrons (TiO_2 , ZnO et SnO_2) et aussi des couches de transport des trous (Spiro-OMeTAD ,P3HT,CuO_2,$CuSbS_2$ et CuSCN).

La deuxième partie est axée essentiellement sur l'étude de la diminution du taux de recombinaison au niveau des couches d'interface des PSCc, qui pourrait fournir une efficacité de 26 .56% en employant $(FAPbI_3)_{0,85}(MAPbBr_3)_{0,15}$ comme couche absorbante. Nous avons montré aussi l'effet de la band de conduction de couche du transport des électrons et la band de valence de couche du transport des trous .Un procès de fabrication des couches est adapté également dans cette étude.

La troisième partie est réservée à la simulation numérique du modèle ‘’drift-diffusion’’ afin d'augmenter le rendement des inorganiques PSCc, en utilisant $CsPbI_2Br$ SnO_2 comme

couches active et de transport des électrons respectivement pour étudier l'effet de la band de conduction on utilisant diffèrent couches de transport des trous selon le schéma suivante :

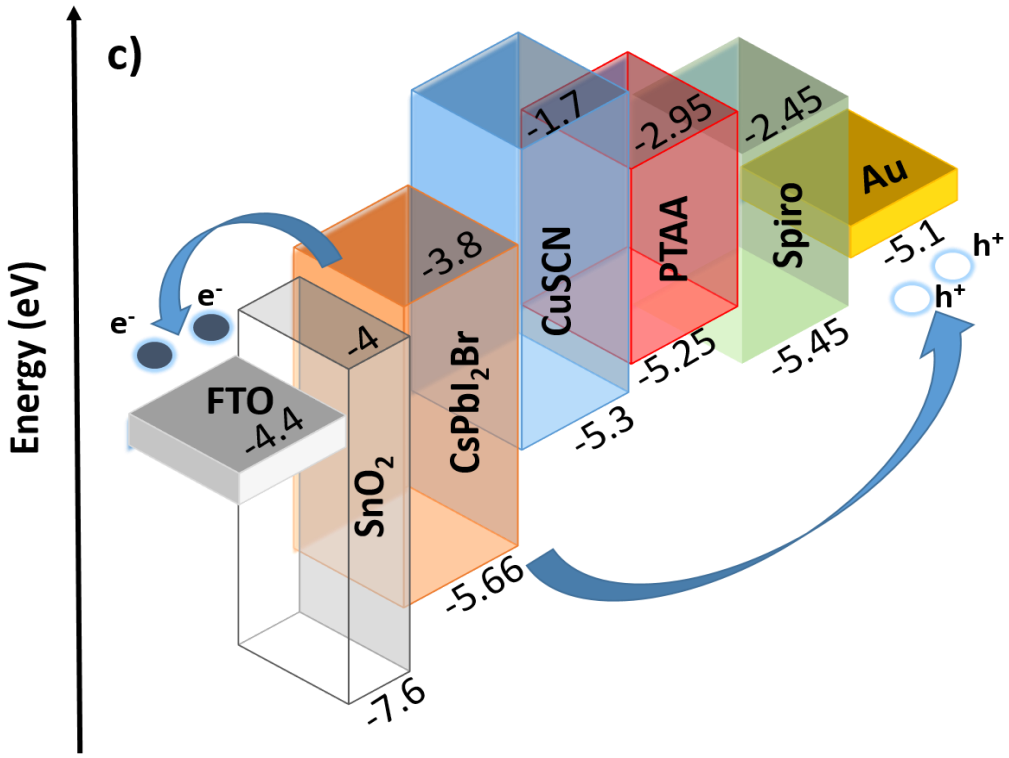

Nous avons proposé aussi l'utilisation des cellules solaire qui respectent l'environnement à base de $CsSnI_{3-x}Br_x$ comme couche active. On adaptant aussi une méthode de synthèses et préparation pour fabriquer une cellule photovoltaïque à base de matériaux inorganique pérovskite.

List of figures

List of Tables

List of Abbreviation :

CB	Conduction band
CuSbS2	Copper antimony sulfide
CuSCN	Cuprous thiocyanate
DMF	Dimethyl Formamide
DMSO	Dimethyl Sulfoxide
DSSC	Dye Sensitised Solar cells
E_c	Conduction Band
E_f	Fermi Level
E_g	Band Gap
EQE	External Quantum Efficiency
ETL	Electron transport Layer
eV	Electron Volt
E_v	Valence Band
FF	Fill Factor
FTO	Fluorine doped Tin Oxide
h	Plank's Constant
HOMO	Highest Occupied Molecular Orbit
HTL	Hole Transport layer
I	Intensity
J_{rec}	Recombination Current Density
J_{sc}	Current Density
J-V	Current Voltage
L_D	Diffusion length
LUMO	Lowest Occupied Molecular Orbit
N_A	Acceptor density
N_c	Density of charges at the conduction band

N_D	Donor Density
N_t	Defect density
N_v	Density of charges at the valence band
IGCC	Integrated gasification combined cycle
P3HT	Poly(3 hexylthiophene-2,5-diyl)
PCE	Power Conversion Efficiency
PCSs	Perovskite solar cells
PTAA	Poly(bis(4 phenyl)(2,4,6-trimethylphenyl)amine)
PV	Photovoltaics
R	Resistance
R_{rec}	Recombination Resistance
RT	Room temperature
SCAPS	Solar cell Capacitance Simulator Software
SEM	Scanning Electron Microscopic
Spiro-OMeTAD	(Spiro) 2,2',7,7 tetrakis (N,N-pdimethoxyphenylamino)-9,9'- pirobifluorene;
TCO	Transparent Conducting Oxide
t	Goldschmidt tolerance factor
V	Votl
VB	Valence band
VBM	Valence band Maximum
V_{oc}	Open Circuit Voltage
XRD	X-ray Diffraction
α	Alpha (absorption coefficient)
ε_r	Dielectric constant
ν	Frequency of Light
χ	Electron Affinity
μm	Micrometer
μ_n	Electron Mobility
μ_p	Hole Mobility

List of publication :

1. **Yassine Raoui**, Hamid Ez-Zahraouy , Najim Tahiri, Omar El Bounagui , Samrana Kazim ,Shahzada Ahmad. "Performance analysis of $MAPbI_3$ based perovskite solar cells employing diverse charge selective contacts: Simulation study." Solar Energy 193 (2019): 948-955.

DOI: https://doi.org/10.1016/j.solener.2019.10.009

2. **Yassine Raoui**, Hamid Ez-Zahraouy , Samrana Kazim , Shahzada Ahmad. " Energy level engineering of charge selective contact and halide perovskite by modulating band offset: Mechanistic insights ": (Journal of Energy Chemistry)

DOI: https://doi.org/10.1016/j.jechem.2020.06.030

3. **Yassine Raoui,** Hamid Ez-Zahraouy , Samrana Kazim , Shahzada Ahmad. "Unravelling of theoretical window for high performance inorganic perovskite solar cells".(in peer-reviewed process)

List of communication

1. **Yassine Raoui**, Hamid Ez-Zahraouy , Najim Tahiri, Omar El Bounagui , Samrana Kazim ,Shahzada Ahmad. Influence of $MAPbI_3$ thickness on ZnO/ $MAPbI_3$/Spiro-MeOTAD solar cell performance. International Conference on Photovoltaic Science and Technologies ,METU, Ankara – TURKEY , July 4-6,2018.
2. **Yassine Raoui**, Hamid Ez-Zahraouy , Samrana Kazim ,Shahzada Ahmad. Improve the performance of inorganic Sn-based pb free perovskite solar cells: Synergies between the computational modelling and experimental studies. Training School-Pearl PV- [COST] Action CA16235- Reliability and Durability of P.V. -MCAST, Malta, Oct 15-18,2019.
3. **Yassine Raoui**, Hamid Ez-Zahraouy , Samrana Kazim ,Shahzada Ahmad. Performance analysis of $MAPbI_3$ based perovskite solar cells employing diverse charge selective contacts: Simulation study ,Conference of Young Researchers in Atomic and Molecular Physics (J2IFAM), UPV-SPAIN, March 3-6th,2020.
4. **Yassine Raoui**, Hamid Ez-Zahraouy , Najim Tahiri, Omar El Bounagui , Samrana Kazim ,Shahzada Ahmad. Influence of $MAPbI_3$ thickness on ZnO/ $MAPbI_3$/Spiro-MeOTAD solar cell performance. 2nd International Materials Science and Engineering for Green Energy Conference, April 25-27,2018, Rabat-MOROCCO.
5. **Yassine Raoui**, Hamid Ez-Zahraouy , Samrana Kazim ,Shahzada Ahmad. Best ePoster Content and Discussion. Designing high efficient eco-friendly lead-free perovskite solar cells: Drift-diffusion Simulation. NanoGeMeetup-TinPero,23 June,2020.
6. **Yassine Raoui**, Hamid Ez-Zahraouy , Samrana Kazim ,Shahzada Ahmad. Performance analysis of $MAPbI_3$ based perovskite solar cells employing diverse charge selective contacts: Simulation study. Workshop - New Materials for a Better Life: Advanced devices and Materials as Key Enabling Technologies for Sustainable Environment/EHU Science Park, SPAIN-Leioa, Nov 27, 2019.

List of award :

1. Best ePoster Content and Discussion

https://twitter.com/nanoGe_Conf/status/1276115422878654465

Chapter 1: General Introduction

''I'd put my money on the sun and solar energy. What a source of power! I hope we don't have to wait until oil and coal run out before we tackle that.''

--Thomas Edison

1 Background

Looking deeply at Edison's message, utilizing renewable energy is vital for the sustainable development of society. The fossil energy sources play a massive part in our daily consumption of electricity. The limitation of the reserve of the fossil energy source is still under debate. Even the storage of oil or coal is always at a high level, but their consequences are already started, pollution and climate change are an example of those consequences. As Barak Obama said, clean energy becomes urgent in the '' The irreversible momentum of clean energy '' [1]. Considering Edison's message, the solution to these issues will come without a doubt from the alternative source energies. Take a look at the electricity production, as shown in Figure 1, the renewable energies are still far from the world's predictions.

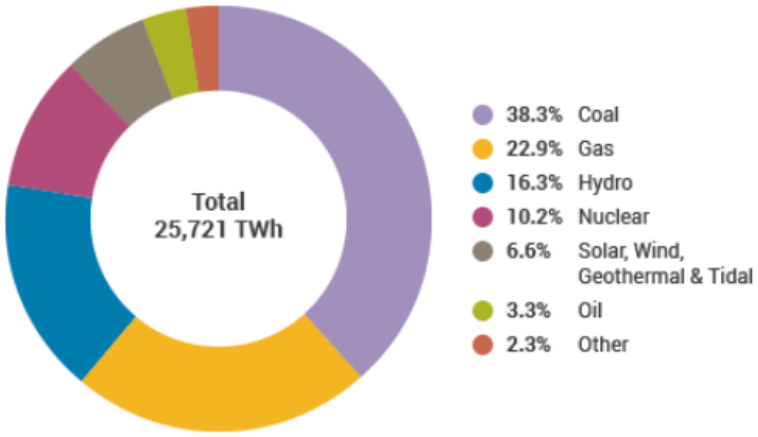

Figure 1: Word electricity production by source 2017[1]

Solar energy is predicted as typical renewable energy to replace fossil fuel supplies to resolve the increasingly severe energy crisis and environmental problems. A solar cell is one critical technique of converting solar energy directly into electric power. Presently, the utility-scale solar power has become cheaper and cost-competitive compared with electricity from traditional energy sources like coal, nuclear, natural gas, and integrated gasification combined cycle(IGCC) power plants and therefore has grown to a massive contribution to the global economy.

However, promising solar cell industrialization that is adequate to resolve the global energy problems remains a considerable challenge. It requires low cost using abundantly available materials and environmentally friendly upstream industries, which call for the state-of-art R&D of new generation solar cells to promote their fast speed industrialization. Dye-sensitized solar cells (DSSc) and perovskite solar cells (PSCs), often regarded as the third generation photovoltaic technology, have

[1] IEA electricity information 2019 /https://www.world-nuclear.org/

gained worldwide interest due to their low cost, environmental-friendly fabrication process, and high energy conversion efficiency. The basic physic behind the emergence of solar cells is inevitable to boost their performance.

2 Solar radiation

The Sun is the central star of our solar system; it contains mainly the hydrogen and helium .the total proprieties of this fantastic start illustrate in Table 1.

Table 1: Properties of Sun

The distance from the Earth	**149,600,000 Km**
Diameter	1,392,000 Km
Volume	1.4E27 cube meter
Mass	1.993E27 kg
Pressure	Over 1 billion atmospheres
The temperature at the center / the surface	About 15,000,000 k/6000 K
Energy radiation	3.8E26 W
The Earth receives	1.7E18 W

The condition at the center of the Sun leads to the operation of nuclear fusion take place with the significant atomic reaction; the proton-proton result according to several steps; four protons react to produce :

- One helium core (two protons and two neutrons),
- Two positrons (the anti-particles of electrons);
- Two neutrinos,
- Electromagnetic radiation.

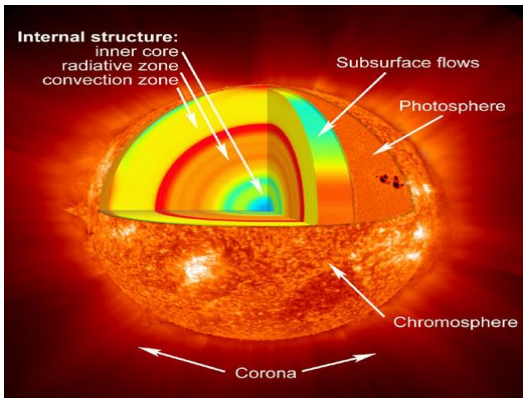

Figure 2:The layer structure of the Sun (obtained from NASA)[2]

The helium core mass is less than that of four protons; the energy difference is converted into energy using Einstein's equation discussed above. The total power is about 3.8E26 W. The center of the Sun is very dense, and solar radiation cannot travel freely. It is still continuously absorbed and re-

emitted, such take to 170 000 years to move to the solar surface. The photosphere (surface of the Sun) is the solar radiation source that hits the Earth. We refer to the solar constant as the total irradiance of the solar radiation at the mean Earth-sun distance on a plane perpendicular to the Sun's direction, outside the Earth's atmosphere, 1361 W/m².

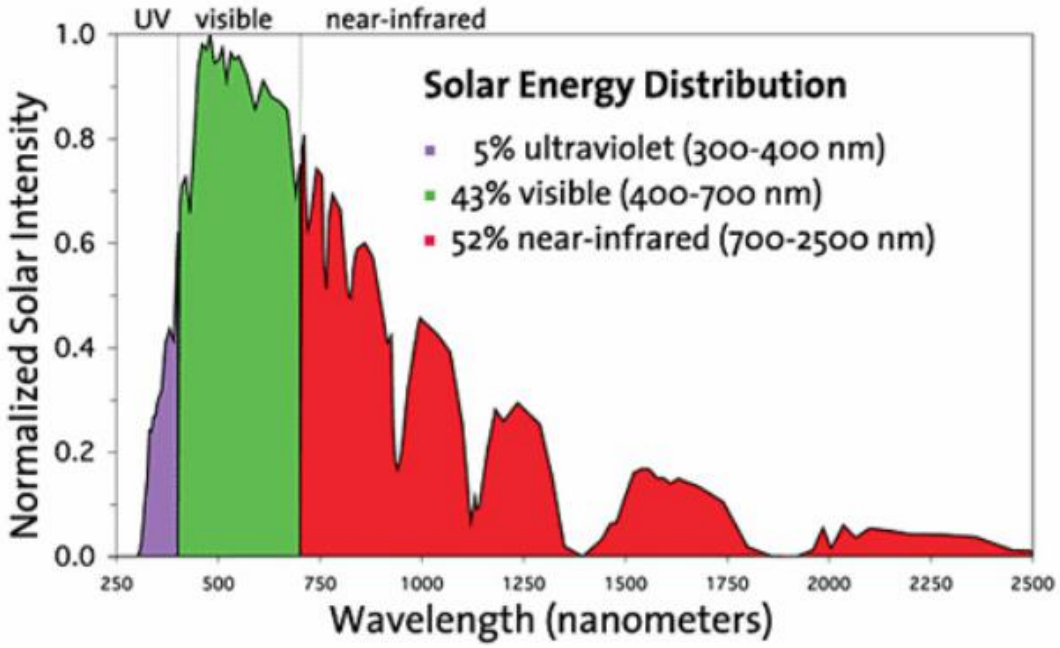

Figure.3: Solar energy distribution vs. wavelength[3]

The spectral distribution of solar radiation is the number of photons of particular energy as a function of the wavelength. The spectrum outside the atmosphere of Earth is called the AM0 spectrum. The irradiance at AM0 is Ie(AM0)=1361 W/m². The irradiance attenuated after passes through the atmosphere of Earth, it is. The Sun's position on the sky and the distance to the surface of Earth have a significant effect on solar radiance when the Sun is at the zenith, in which the shortest distance is called AM0 from the ratio of the optical air mass.

3 Milestones of the photovoltaics :

1839: Alexander -Edmund Becquerel, a young experimental physicist in France, discovered the photovoltaic effect at the age of 19 while assisting his father, experimenting with electrolytic cells made up of two metal electrodes.

1873:W.Smith, working in the U.K., discovered selenium's photoconductivity, which led to the invention of the photoconductive cell.

1883: Ch. Frits, an American inventor, described the first solar cell made from Se selenium wafers.

1887: H.Hertz discovered in Germany that ultraviolet light altered the lowest voltage capable of causing a spark between two metal electrodes.

1888: Ed. Weston receives the first patent for solar cells (U.S. 389124 and US3891-25).

1904: W. Hallwachs discovered the photosensitivity in a copper/cuprous oxide pair.

1904: A.Einstein publishes his pioneering theoretical work on the photoelectric effect (Noble Prize in 1921).

1916: R.A Millikan provides experimental proof of the photoelectric effect.

1916: Y. Czochralski (Polish scientist) develops a new method to grow single-crystal Silicon.

1930:W. Schottky discovers a new cuprous oxide photoelectric cell.

1931: A.F. Ioffe guides a project at the physical-Technical Institute in St.Petersburg on thallium sulfide photocells, which reach a record efficiency at that time of more than 1%.He submitted a proposal to the Soviet government concerning the use of solar P.V. roofs for providing electricity.

1932: Audobert and Stora discover the photovoltaic effect in CdS.

1948: W.Schottky presents the first theoretical concept for semiconductor P.V.

1951: at Bell Labs, the first p-n junction was grown in germanium

1953: D. Trivich publishes the first theoretical calculations on the conversion efficiency of the solar spectrum with materials of different bandgaps.

1953: G. Pearson at Bell abs begins research of Li-doped Si solar cells.

1953: D. Chapin, C. Fuller, and G. Pearson realized a two cm^2 Si solar cell with 4 % efficiency.

1954: D. Chapin, C. Fuller, and G. Pearson improve a-Si Cell's efficiency to 6 %.

1954: At Siemens in Germany, G . Spenke and his team develop an efficient method for poly-Si growth: Scientists and experts from Wacker and T.U. Munich participates in this work as part of a joint team with Siemens. The so-called Siemens Method is the primary technology for the production of solar and Semiconductor grade Si.

1954: J.J. Loferski and Jenny at RCA reported a pronounced P.V. effect in CdS.

1954: The International Solar Energy Society (ISES) was founded in Phoenix, AZ, USA.

1957-1959: Hoffmann Electronics achieves 8,9 and 10 % efficiency and develops the grid contact, significantly reducing the device's series resistance.

1970: Its headquarters later moved to Melbourne, Australia, and in 1995 it was moved again to Freiburg, Germany.

1978: R. Hezel introduced Silicon Nitride as an antireflection and passivation layer, which presently applied for almost all Commercial Silicon Solar Cells.

1980: M.Riel starts the famous 1000 solar roof program in Zurich, Switzerland

1980: B.P. enters the solar business.

1981: The Fraunhofer Institute for Solar Energy ISE in Freiburg, Germany, was founded by A. Goetzberger.

1983: P.V. production worldwide exceeds 20 M.W., and sales exceed 250 million USD.

1983: International Science and Engineering Conference (The Asian ISE-Conference) started.

1985: M. Green at the University of New South Wales, Australia, breaks the 20 % efficiency barrier for c-Si Solar cells under one Sun in the research lab.

1985: R. Hezel and K. Jaeger introduced Aluminum Oxide as a passivation layer for a new generation of Silicon Solar Cells.

1986: ARCO Solar releases the first commercial thin-film power module.

1987: The Institute for Solar Energy Research (ISFH) was founded in Hamelin /Emmethal, Germany.

1991: M. Graetzel invents the dye-sensitized electrochemical solar cell. The efficiency of more than 10 % was obtained within five years after the discovery.

1994:NREL develops and demonstrates a two-terminal, high-efficiency GaInAsP/GaAs solar cell, which under 180 suns shows more than 30 % efficiency. The third generation CPV was born.

1994: David Mitzi et al. reported a conducting layered tin iodide with a perovskite structure.

1997: The biggest P.V. roof with more than 3 M.W. installed in Munich, Germany.

1999: M.A. Green and J.Zhao achieved a record efficiency of 24.7 % for laboratory c-Si Solar cells.

1999: Total P.V. power installed worldwide exceeds 1 G.W.

2002: Photon in Munich, Germany organized the first Solar Silicon Conference dealing with the Si feedstock crisis.

2007: SunPower and Sanyo announced the highest efficiency for the mass-produced solar cell under one sun solar radiation of 22 %.

2007: UN-conference devoted to climate change takes place in Bali.

2009: T.Miyaska et al. demonstrated first Perovskite cells with 3.8 % efficiency

2010: Oxford P.V. Ltd. Founded to develop and commercialize Perovskite photovoltaics

2010: ZSW announced an efficiency record of 20.1 % for CIGS cells (0.5 cm^2)

2012: H. Snaith and M. Lee demonstrated the first solid-state perovskite P.V. cell.

2013: perovskite P.V. cells reach 15 % (O.Malinkiewics and J.Burshka)

2014: Nam Joong Jeon et al. used the solvent -engineering to deposit very dense perovskite layers on mesoporous titania to enhance the efficiency.

2014: Perovskite cells reached 20.1 % efficiency at KRCT (Korea).

2015: Sauletech, Poland pioneered first ink-jet printed perovskite P.V.

2015:EPFL IN Switzerland reports 21 % world record efficiency for Perovskite cells.

2016: kaneka Corporation achieved 26.33 % world record with a heterojunction cell.

2016: First manufacturing site of Oxford P.V. for c-Si/Perovskite tandem cells and modules, located in Germany.

2016: UNIST (South Korea) reached 22.1 % efficiency with Perovskite cells.

2016: UC Berkeley and Stanford reported first graded junction all perovskite P.V.

2017: First industry-sized perovskite /silicon tandem cells produced at Oxford P.V. in Germany.

2018: Anita Ho-Baillie developed a two-step deposition method that enables the conformal coating of textured surfaces with perovskite films.

2019: new world record of perovskite solar cell at 25.2 % by KRICT/MIT.

2019: the 10th anniversary of work by Tsutomu Miyasaka and colleagues pioneering hybrid halide perovskites in photovoltaics.

2020: 25.5 % efficiency of single PSCs and 29.15 % efficiency is the new world record for a tandem solar element with perovskite and Silicon developed by Lithuanian and German researches.

2021: can we see 30% in efficiency????

3.1 Technologies of photovoltaic

Based on the progress of photovoltaic conversion chronology, the design of this technology illustrated in the following figure :

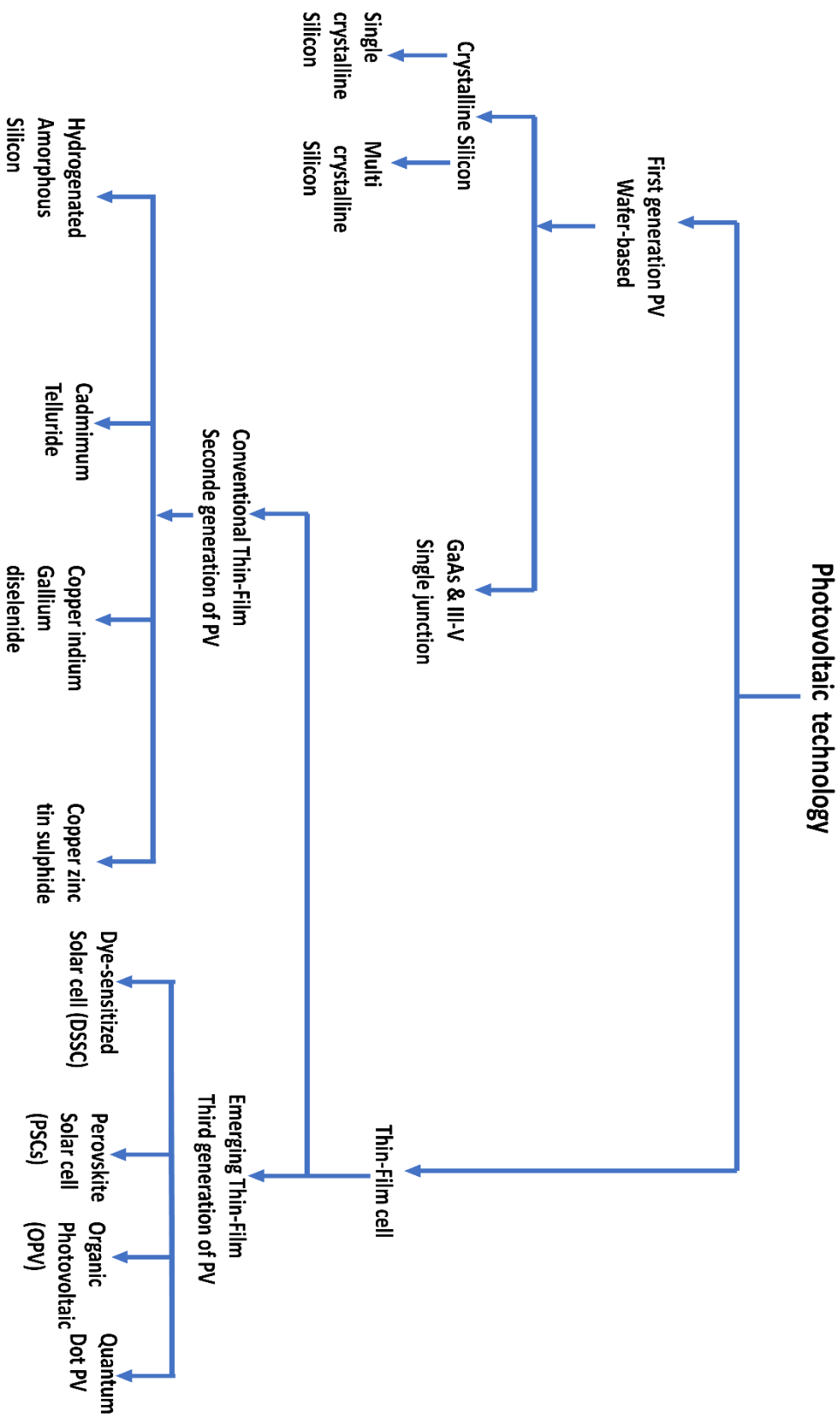

Figure 4: Classification of photovoltaic technologies

Recently, there have been many interesting academic and industrial laboratories on Perovskite materials as harvest light in solar cells. The power conversion efficiency (PCE) of perovskite solar cells has reached 25.2 % in 2020, which was 6 % in 2010. The efficiency value of PSCs has surpassed the certified PCE of 22.2 % for thin-film crystalline silicon solar cells from Solexel (USA) in 2014, 22.1

% CdTe solar cells from First Solar (USA) in 2017, 22.6 % for CIGS solar cells from ZSW (Germany) in 2016.

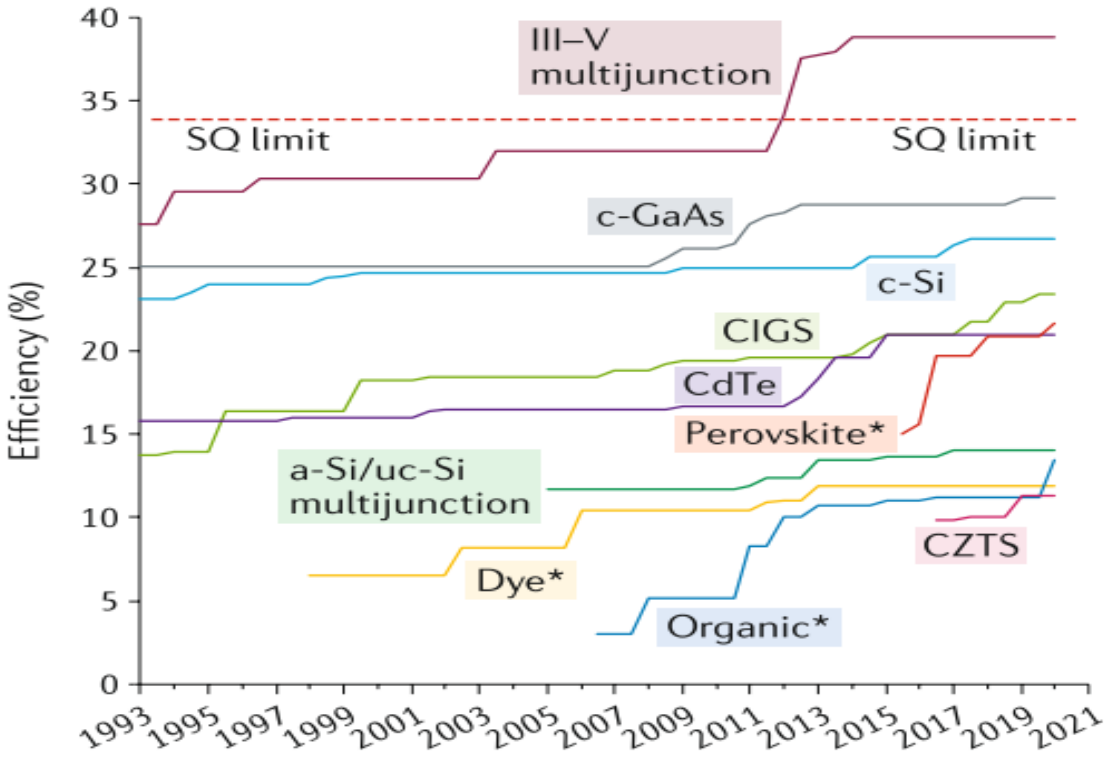

Figure 5:Best cart research efficiencies[4]

Today most researchers in the field of solar cells are focusing on the PSCs as a promising technology in single junction or tandem technologies [5]. The perovskite semiconducting materials have attracted massive attention due to its low binding energy, long diffusion length, long carrier lifetime, and intense light absorption with a direct tunable bandgap 1.2-2.7 eV [6–8]. As far we know, the efficiency of PSCs has reached 25.2 % [5], and the first cell based on perovskite material published in 2009 by Miyasak and his group was 9% [9]. This fast improvement of efficiency is a result of the optimization of perovskite composition, deposition procedures, design structures, charge extraction, efficient selective layer[10–14]. But the device modeling and simulation of PSCs presents just a sliver compared to the experimental studies of the field. Later a few studies have demonstrated the efficient macroscopic device model of PSCs to answer the issues of these promising technologies. Those studies have focused on optimizing perovskite thickness, doping, and electrical parameters [15]. Also, the matter of misalignment of layers in the solar cell [16], either building new efficient structures. The basic concept of PSCs is sketched in Figure 6. We have p-i-n or n-i-p configuration; the i-layer is a semiconductor perovskite material as the harvest light. Also, two selective layers, one as electron transport layer (ETL) and the other as the hole transport layer (HTL), are added to the back and front contacts.

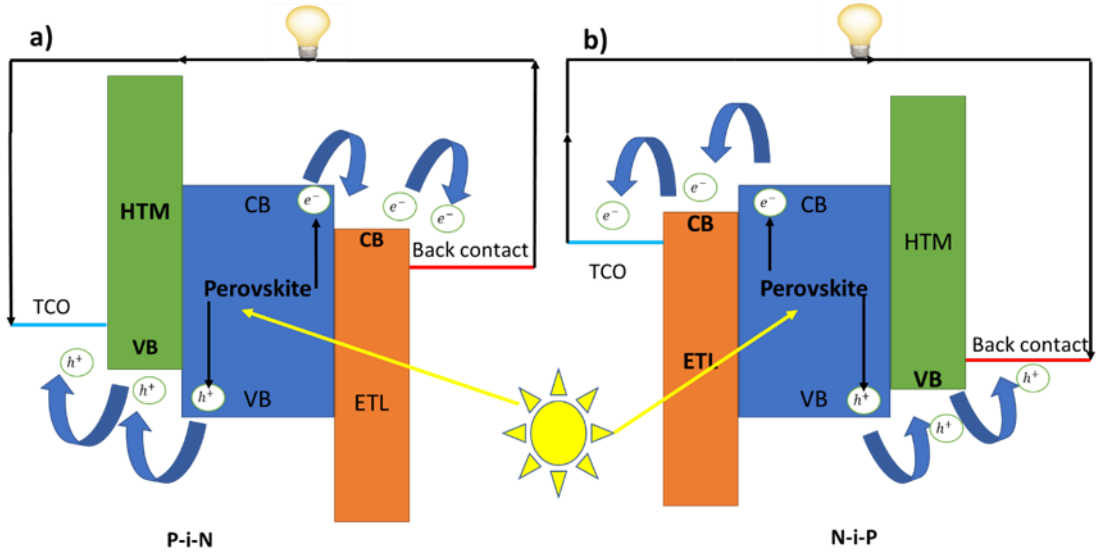

Figure 6:Basic principal of PSCs based on. a)p-i-n .b)n-i-p

4 Device structures

The configuration of perovskite solar cells is divided into four structures; PSCs use a thin perovskite absorber layer between an ETL and HTL. The collection of the electrons or holes made at the conducting substrate (Transport conduction oxide, TCO); the PSCs can be classified as n-i-p or p-i-n device, respectively.

The ETL, perovskite, and HTL can be made from different materials, as illustrated in Figure 7 depends on the energy alignment between the layers, which will facilitate the transfer of electrons and holes outside the cell.

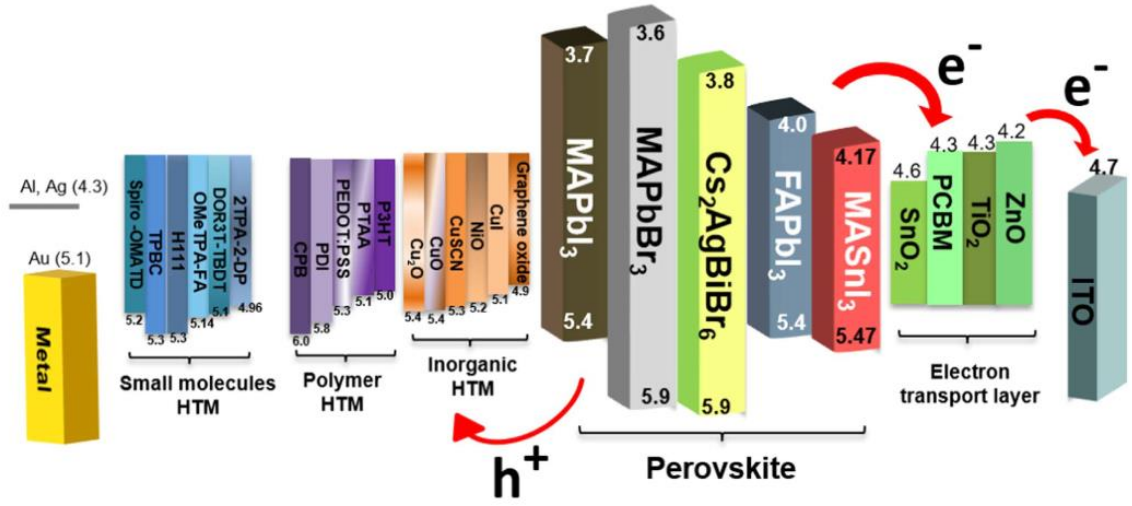

Figure 7:Energy level alignments of different layers in PSCs [16]

5 State of the art numerical simulation of PSCs

Since the beginning of perovskite photovoltaics, tremendous experimental efforts have been made to push the PCE, wish reached incredible numbers. This continuous improvement in PCE results

from a colossal optimization in all layers of the cell, such as film deposition, deposition procedures, and device design. In parallel to this experimental outline success, there is a weakness investigation in device modeling and simulation, which means it should be an eye on developing a comprehensive device model with available tools to match the common problem in the experimental field.

"The device model is a powerful tool for predicting the characteristics of the thin device from organic to perovskite. By linking the observable current-voltage curves directly to each of the relevant microscopic physical processes, the method exhibits a concept of computer-assisted design of the thin-film solar cells. The device model simulation will be helpful in the mass production of the versatile structural thin film devices". A review published in Advances Sciences Journal in 2019.[17]

6 Research aim and objectives

This paragraph is taken from a particular section of a review published in Science journal opened for PSCs in 2017 ."PSCs face challenges such as long-term durability that prevent them from competing with established technologies. However, advancement in materials processing during the past 2 years have yielded remarkable progress in long-term material and device stability , enabling the research community to better identify intrinsic versus extrinsic degradation mechanisms, some of which are summarized here. Despite the rapid improvement in the performance, there is still room for tailoring charge carrier recombination, both in the perovskite and at the interfaces within the device, to increase PCEs. Major challenges to long-term stability also remain."[18]

The balance of The PSCs becomes dense to win the other photovoltaic technologies, but even that, this alternative technology suffers from tremendous problems that stop its commercialization. The following lines review the significant challenges of PSCs which the community of research should focus on solving them :

- Poor stability and the high cost of selective organic layers.
- High-temperature process electron transport layer
- The theoretical limit of Shockley Queisser Efficiency
- Misalignment between the absorber layer and selective layers
- Stability issue under environmental conditions.
- Toxicity of lead element in the traditional efficient PSCs.
- High-cost electrode materials

In this regards, the objective of this thesis will focus on using physical device modeling to address those issues with the main points :

- Starting the basic simulation model with 1D SCAPS software utilizing the absorption of layers extracted from our experimental fabrication.
- The proposition of alternative cheap and efficient selective layers
- The proposition of low-cost electrode materials as back contact of PSCs.
- Optimization of structure through diverse parameters such as thickness, doping, and alignment
- Deeply understand the misalignment between the ETL and perovskite material and HTL.
- Enhance the performance of organic lead and lead-free PSCs.
- Fabrication of efficient perovskite materials and ETLs

7 Planning of the thesis

7.1 SCRUM method

The planning of my work is organized by the SCRUM method to manage the time and be more productive by making a plan of three years and working with ‘’To Do ‘’, ‘’ In progress ‘’ and ‘’ Done” to assigned the tasks every week.

Figure 8: SCRUM method

7.2 Thesis Outline

The thesis is composed of seven themed chapters.

Chapter 1 describes a brief introduction of the thesis by figure out the art state of energy source and the spectrum solar as a source for generating the electricity, also will open the door to the technology of perovskite solar cell by their basic architecture, performance compared to other photovoltaic technologies and the main challenge are faced this promising technology.

Chapter 2 will give a comprehensive survey on the theory of physic of Semiconductor as it is the stone foundation of solar cells, and also a description of the working principle of a solar cell. The second part will focus on the review of perovskite solar cells by showing the structure and different materials used in a cell from the absorber layer to the electron transport layer and hole transport layer as well, the fabrication processes of the divers layer in PSCs.

Chapter 3 is the research method and materials adapted to perform this thesis. The SCAPS software, as the tool used for numerical simulation of PSCs, is explained through its interface. The technique used to fabricate different layers of cell and characterization techniques is outlined.

In **chapter 4,** the performance analysis of MAPbI3 based perovskite solar cells employing diverse charge selective contacts: Simulation study is discussed. This work has been published in Solar Energy Journal.

Chapter 5 will be on the study of Energy level engineering of charge selective contact and halide perovskite by modulating band offset: Mechanistic insights, by investigating the advantage of band offset on the performance of PSCs through numerical study starting by experimental fabrication of layers. This work has been published in the Journal of the energy of chemistry.

Chapter 6 focused on the Unraveling of the theoretical window for high-performance inorganic perovskite solar cells. This study has demonstrated, for the first time, the performance of inorganic lead and lead-free PSCs and suggested some tips to push the efficiency of inorganic PSCs. The eco-friendly PSCs is investigated by drawing a proper manner to promote the efficacy of this promising solar cell in term of efficiency or protection of the environment. This work has been submitted for publication in the PCCP journal.

Chapter 7 will describe the experimental investigation which has been done during this thesis about the fabrication of efficient Electron transport layer, organic-inorganic perovskite materials, and also the process fabrication of inorganic perovskite solar cells.

The thesis concluded**,** and the future prospect of this work was also discussed.

Chapter 2: Theory of Semiconductor & Perovskite Solar Cell

1 Introduction

This chapter will design an idea about the importance of using semiconductors in solar cells and a full description of Perovskite Solar cells.

2 Types of materials

The distance between the valence band and the conduction band in materials defines the electrical proprieties which design three classifications of materials, Insulator, conductor, and Semi-conductor [19].

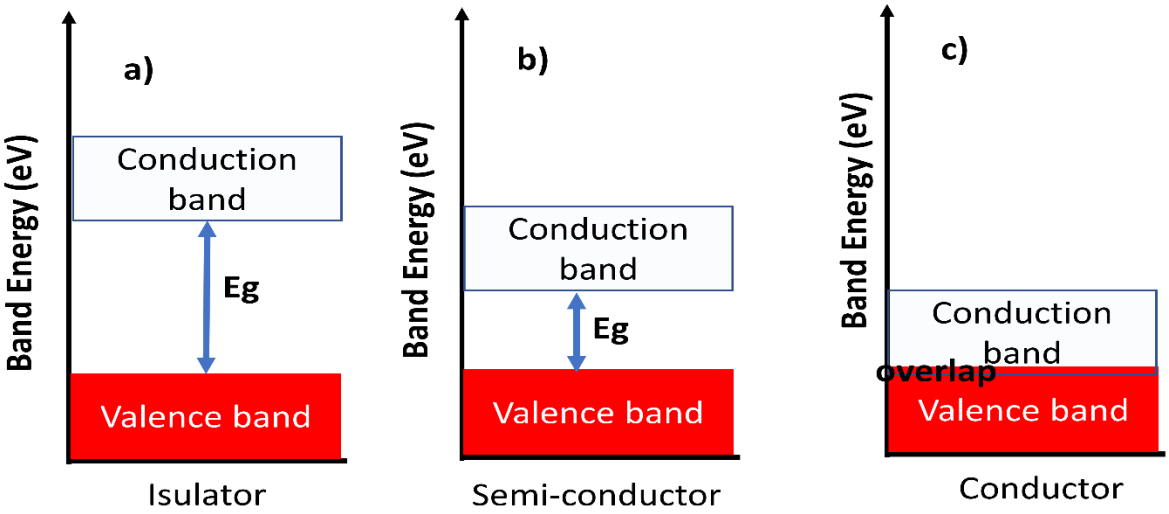

Figure 9: energy band diagram of a)insulator) Semiconductor, C) Conductor

In insulators Figure 9-a, they are a type of material not conducting the electrical current in the normal situation and have a high resistivity. The conduction band is empty contract to the valence band, i.e., no free charges present, with a large band gap[20]. The second type of material is Semi-conductor Figure 7-b, which comes between Insulator and Conductor. At 0K, the valence band is full, and the conduction band is empty; just a few increments of temperature lead to some electrons to jump to the valence band due to the small-large of the band gap, i.e., the conductivity increased with temperature. The third type of material is the conductor Figure 9-c, which has an overlap conduction band and valence band, an-cd many of free charges in the conduction band which efficiently conduct the electrical current.

The next lines of this work will focus on Semiconductors as an excellent absorber to convert solar radiation into electricity.

3 Theory of Semi-conductor

3.1 Definition

Semiconductor are materials whose electrical proprieties lie in between conductor and insulator, in term of band gap, which controlled from the valence band edge (E_v) and the conduction band edge (E_c)

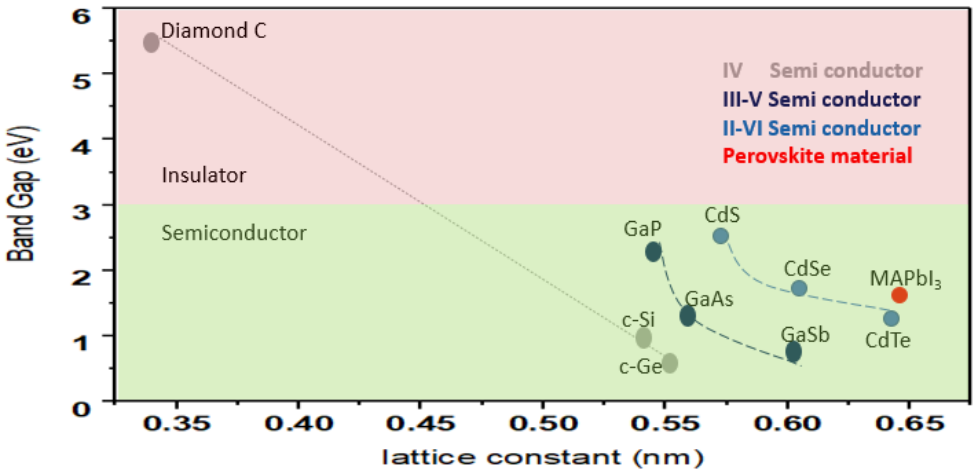

Figure 10: The relation between the lattice constant and band gap for different categories of materials.

The Semiconductor can be made from single elements like Si and Ge, or from mixed materials, GaP, CdS, CdTe, and $MAPbI_3$, as shown in Figure *10*. The lattice constant can control the band gap, which can differ the proprieties of semiconductors

3.2 Intrinsic semiconductors

3.2.1 Band diagram

At a temperature of zero kelvin, Figure *11-a* is an accurate representation of a silicon crystal lattice. All valence electrons are fixed in the lattice, forming covalent bonds, and are therefore immobile. However, at a temperature above absolute zero, thermal energy is supplied to the Semiconductor, and some of the valence electrons are released from the covalent bonds; these excited electrons are mobiles that can move around in the materials, allowing the semiconductor material to conduct electricity as shown in *Figure 9-b.*

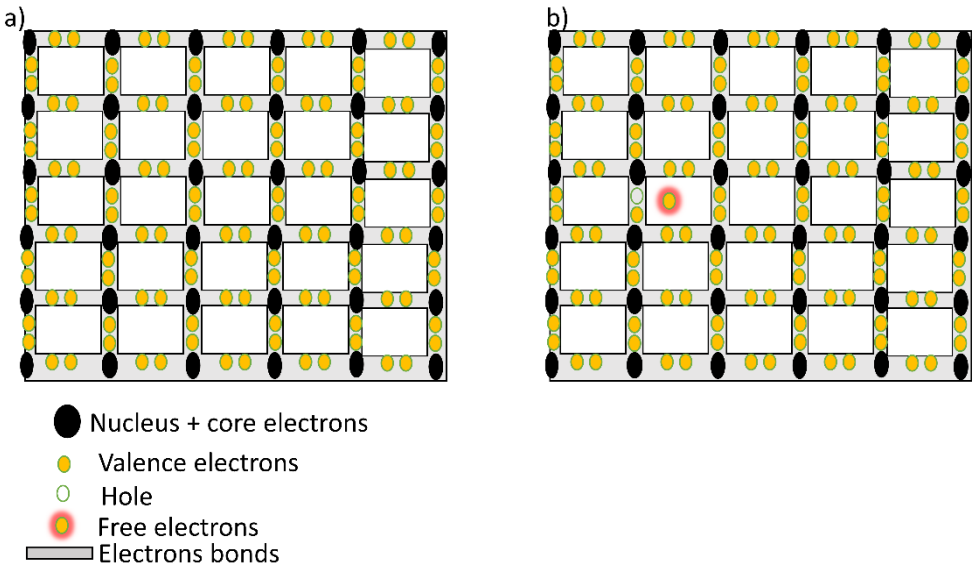

Figure 11:The bonding model for c-Si, a) No bond is broken. b) A bond is broken between two Si atoms

The valence band comprises the energy levels of all valence electrons in a semiconductor material at absolute zero. When a valence electron receives additional energy, either from a photon or through thermal vibrations, it can become mobile. The band of allowed energy states for these conduction electrons is known as the **conduction band**.

The band gap energy, indicated by E_g, is equal to the difference between the conduction band edge and the valence band edge.

The materials **semiconductors** have a valence shell that is about half full. On the other hand, the elements have a vast band gap, and the valence electrons require a considerable amount of energy to be released from the valence shell, which means have a relatively small amount of mobile electrons at room temperature and therefore conduct electricity very poorly, there are called **insulators**. The third type of element is **Metals**, which have only 1 or 2 electrons in their valence shell, which are very loosely bound.

3.2.2 Semiconductors under thermal equilibrium

At room temperature (300 K), the band gap of $MAPI_3$ as a type of semiconductors is 1.56 eV or crystalline silicon 1.12 eV; the energy band diagram is a plot of the allowed electron energy states as a function of position as illustrated in Figure *12-a*.

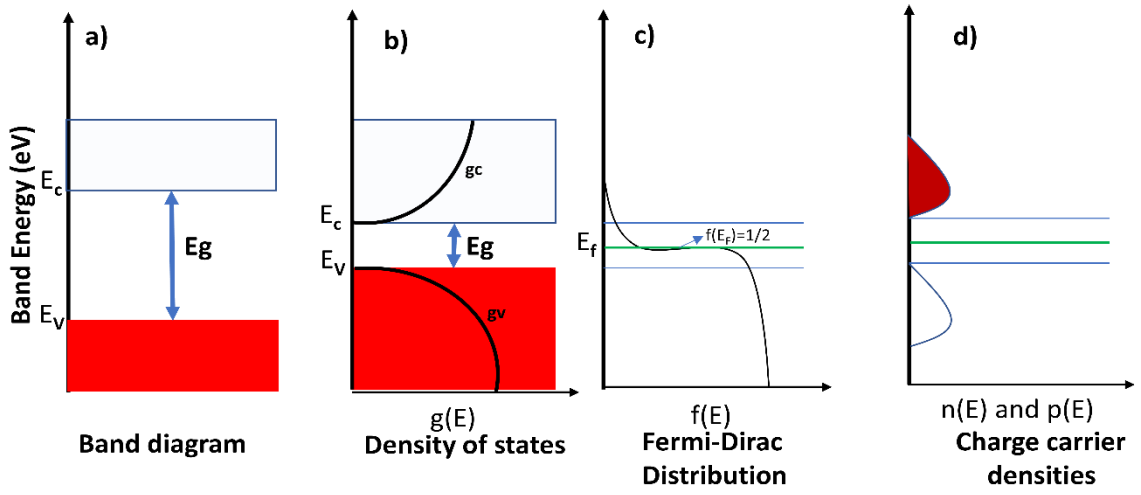

Figure 12:a) Basic band energy diagram .b) the density of states (DOS) functions in the valence band and conduction band. c) The fermi Dirac distribution. d) The electron and hole densities in valence and conduction band.

The density of energy states at an energy E in the conduction band close to E_c and the valence band close to E_v is given by :

$$g_c(E) = 4\pi \left(\frac{2m^*_n}{h^2}\right)\frac{3}{2}\sqrt{E - E_c} \quad (1)$$

$$g_V(E) = 4\pi \left(\frac{2m^*_p}{h^2}\right)\frac{3}{2}\sqrt{E_c - E} \quad (2)$$

g_c : DOS in the conduction band

g_V : DOS in the valence band

E: Electron energy

E_c : The lowest energy level of C.B.

E_V: The highest energy level of V.B.

$m*_n$: Effective masses of electrons

$m*_p$: Effective masses of holes

The Fermi -Dirac distribution function is given by :

$$f(E) = \frac{1}{1+\exp(\frac{E-E_f}{k_B T})} \quad (3)$$

E: Electron energy

k_B : Boltzmann's constant, k_B=1.38E-23 J/K

E_f : Fermi Energy

$k_B T$: Thermal energy, at 300 k

The Fermi energy, also called the Fermi level, is the electrochemical potential of the electrons in a material. In this way, it represents the average energy of electrons in the bulk material.

The carriers that contribute to charge transport are electrons in the conduction band and holes in the valence band. The concentration of electrons in the conduction band and the valence band is found by multiplying the density of state function with the distribution function and integration across the whole energy band, as illustrated in Figure *12-b-c-d.*

- Electrons in the conduction band

$$\mathrm{n(E)} = g_c\ (E) f(E) \quad n = \int_{Ec_c}^{E_{top}} n(E)dE \qquad (4)$$

- Holes in the valence band

$$\mathrm{p(E)} = g_V\ (E)\lfloor 1 - f(E) \rfloor\ p = \int_{E_{bottom}}^{E_V} n(E)dE \qquad (5)$$

Where N_C and N_v are the effective densities of the conduction band states and the valence band states, respectively, they are defined as

- Effective densities of conduction band state:

$N_c = 2\ (\frac{2\pi m*_n\ k_B T}{h^2})^{3/2}$ *at 300 K in c-Si* $N_c = 3.22E19\ cm^{-3}$*(6)*

- Effective densities of valence band state:

$N_v = 2\ (\frac{2\pi m*_p\ k_B T}{h^2})^{3/2}$ *at 300 K in c-Si* $N_v = 3.22E19\ cm^{-3}$*(7)*

3.2.2.1 Fermi level

In intrinsic Semiconductor in equilibrium, we have $n=p=n_i$

$$np = n_i^2 = N_c N_v exp\left(-\frac{E_g}{k_B T}\right) (8)$$

we may write :

$$E_{Fi} = \frac{E_c - E_v}{2} + \frac{k_B T}{2} \ln\left(\frac{N_v}{N_c}\right) (9)$$

The Fermi level E_{Fi} lies close to the mid-gap; a slight shift is due to the difference in the densities of the valence and conduction band.

In the intrinsic semiconductor the concentration of electrons is equal to those of holes .In intrinsic Silicon at room temperature[1] approximately 1.5 E10 cm^{-3} broken bonds are present , i.e , $n=p=n_i$= 1.5 E10 cm^{-3} .

3.3 Proprieties of semiconductors in non-equilibrium conditions

3.3.1 Photo-generation

the photoelectric effect, where electrons are emitted from a material that has absorbed light with a frequency above a material-dependent threshold frequency. As Albert Einstein found in 1905 [21]; the energy of such a photon is given by ;

$$E = hv (10)$$

$$v = \frac{c}{\lambda} (11)$$

E: photon of energy

h: Planck's constant

v:frequency

C: speed of light

λ: Wavelength

Absorption is a process in which the electromagnetic radiation interacts with atoms of a semiconductor, particularly with the valence electrons. The photo-generation results in the generation of electron-hole pairs, however, this excitation not always happen, if we look to the band gap of $MAPI_3$ as perovskite semiconductor is equal 1.56 eV, the generation of electron-hole pair can happen only if the photon energy is equal or higher than the energy of the band gap, e.i, x nm is the wavelength of the electromagnetic radiation corresponding to this energy value, compared to the Silicon which has 1110 nm.

This photo-generation under non-equilibrium conditions creates two new fermi level inside the Semiconductor called Quasi Fermi levels E_{Fn} and E_{Fp} as designed in Figure.*13.*

In contrast to the equilibrium conditions, a net electrical current flows through a semiconductor device under operational conditions. The electrical current is generated in a semiconductor due to the

transport of charges by electrons and holes. The two underlying transport mechanisms in a semiconductor are drift and diffusion.

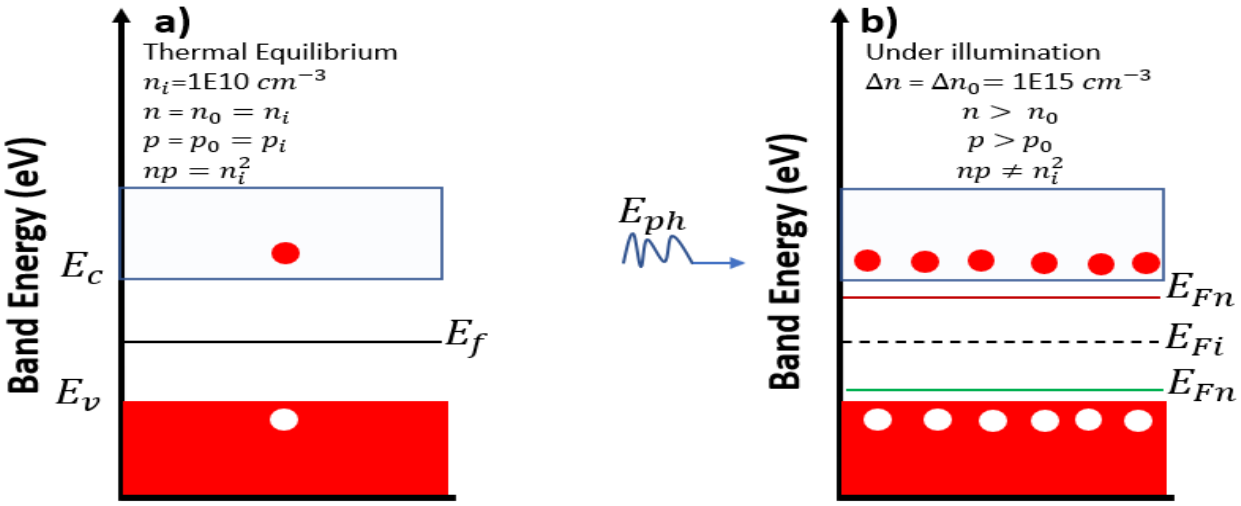

Figure.13: The position of Fermi level (a) in thermal equilibrium (b) under illumination.

3.3.2 Transport properties

3.3.2.1 Drift

Drift is charged particle motion in response to an electric field. In an electric field, the force acts on the charged particles in a semiconductor, which accelerates the positively charged holes in the direction of the electric field and the negatively charged electrons in the opposite direction.

$$J_{drift} = q(p\mu_p + n\mu_n)\,\xi \quad (12)$$

ξ/electric field

3.3.2.2 Diffusion

Diffusion is a process whereby particles tend to spread out from regions of high particle concentration into low particle concentration areas as a result of random thermal motion. The driving force of diffusion is a gradient in the particle concentration.

$$J_{diff} = q(D_n\nabla_n - D_p\nabla_p)\,\xi \quad (13)$$

3.3.2.3 Poison equation

The poison equation is related to the density of electric charges ρ (r) to the electrical potential V (r) :

$$\frac{d}{dx}\left(\varepsilon(x)\frac{d\Psi}{dx}\right) = q[\,p(x) - n(x) + N_D^+(x) - N_A^-(x) + p_t(x) - n_t(x)\,] \quad (14)$$

3.3.2.4 Continuity equation

The charges are a conserved quantity. The continuity equation takes drift, diffusion, and recombination as well as generation processes into account :

$$\frac{1}{j}\frac{\mathrm{d}J_p}{\mathrm{d}x} + R_p(x) - G(x) = 0 \quad (15)$$

$$-\frac{1}{j}\frac{\mathrm{d}J_n}{\mathrm{d}x} + R_n(x) - G(x) = 0 \quad (16)$$

3.4 Generation and recombination in a Semiconductor

The generation and recombination of free charge carriers are at the heart of any semiconductor device mechanism, including solar cells.

3.4.1 Conductivity

the electrical conductivity of a semiconducting material quantifies the ability of that material to conduct electrical current

$$\sigma = e\ \mu_n\ n + e\mu_p\ p \ (17)$$

3.4.2 Generation and recombination

Generation is the process in which free charge carries are created, with the emphasis on free and recombination is the process in which free charge carries are annihilated. At thermal equilibrium, the carrier concentration at a given temperature is constant as a function of time, that in case the generation rate of charge carriers is spatially uniform, the recombination rate should balance this, and that this recombination rate is proportional to the thermal equilibrium majority carrier concentration of the semiconducting material.

3.4.2.1 **Recombination processes**

There are four types of recombination processes, Radiative, Auger recombination, Shockley-Read-Hall, and surface recombination.

3.4.2.1.1 Radiative recombination

In radiative recombination, the energy of the recombination process between an electron and a hole is emitted as a photon after recombination, which its energy is a bit higher than the energy of the band gap of the semiconductor material, and radiative recombination rate is :

n-type :

$$R_d = \beta n_0(p - p_0) \ (18)$$

p-type :

$$R_d = \beta p_0(n - n_0) \ (19)$$

B : is a proportionality factor

Radiative recombination is important for direct band gap semiconductor.

Another concept should explain it, the lifetime of minority carrier :

For minority carrier holes in an n-type semiconductor :

$$\tau_p = \frac{1}{\beta n_0} \quad (20)$$

For minority carrier electrons in a p-type semiconductor :

$$\tau_n = \frac{1}{\beta p_0} \quad (21)$$

When we don't have an uniform carrier generation, we introduce the diffusion length :

p-type material : $$L_n = \sqrt{D_n \tau_n} \quad (22)$$

n-type material : $$L_p = \sqrt{D_p \tau_p} \quad (23)$$

D : diffusion coefficient

3.4.2.1.2 Auger Recombination

Auger recombination, becomes important in indirect band gap semiconductor, in this type of recombination, momentum, and energy of the recombining hole and electron is conserved by transferring energy and momentum to another electron or hole. If the third part is an electron, it is excited electron higher into higher levels in the electronic band .this excited electron relaxes again, transferring its energy to vibrational energy to vibrational energy of the lattice or phonon modes, and finally heat. Similarly, if the third particle is a hole, it is excited into deeper levels of the valence band, from where it rises back to the valence band edge by transferring its energy to phonon modes.

The recombination rates for electron-electron-hole (eeh) and electron-hole-hole (ehh) processes are given by :

$$R_{eeh} = C_n n^2 p \quad (24)$$

$$R_{ehh} = C_p n p^2 \quad (25)$$

$$R_{Aug} = C_n n^2 p + C_n n^2 p \quad (26)$$

3.4.2.1.3 Shockley Read Hall recombination

In the Shockley-Read-Hall (SRH) recombination process, which illustrated in Figure.*14,* the recombination of electrons and holes does not occur directly from bandgap to bandgap.it is caused by an impurity atom or lattice defects. Their concentration is usually small compared to the acceptor or donor concentrations. These recombination centers introduce allowed energy levels (E.T.) within the forbidden gap, so-called trap states. An electron can be trapped at such a defect and consequently recombines with a hole that is attracted by the trapped electron. It is the dominant recombination-generation process in semiconductors in most operating conditions. The process is typically non-radiative, and the execs energy is dissipated into the lattice in the form of heat. The name is a reverence

to William B.Shockley, William T.Read, and Robert N.Hall, who published the theory of this recombination mechanism in 1952 [22,23].

There are two kinds of traps, as sketched in Figure *15;* first, donor-type traps that are neutral when they contain an electron and positively charged when they do not. Secondly, acceptor-type traps that are negatively charged when they include an electron and neutral when they do not.

The SRH process is based on four operations that are involved in recombination in a single-electron trap :

- r1: capture of an electron from the conduction band ;
- r2:emission of an electron to the conduction band ;
- r3:capture of a hole from the valence band ;
- r4:capture of an electron from the conduction band ;

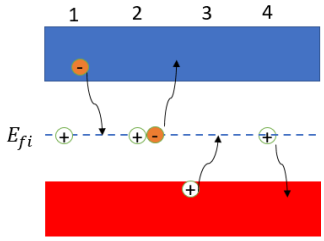

Figure.14: Schematic illustration of the processes in SRH recombination.

Figure 15 : Type of traps inside a semiconductor

3.5 Extrinsic Semiconductors

3.5.1 Atomic structure

The atomic number of Silicon is 14; the Kohn-sham orbital gives Si 4 atoms in the outermost shell that can interact with other atoms via forming chemical bonds (Valence electrons). Two Si atoms are bonded together when they share each other's valence electrons, which called covalence bond between two electrons. At room temperature always there is a probability of presence valence bond broken, which can liberate an electron (mobile/free) in the crystal lattice leads to create a positive charge is referred to a hole as explained in Figure : *16.*

At high 0K temperature, the bonds start to break due to the absorption of thermal energy. This process results in the creation of free electrons and its missing place so-called hole. When a bond is broken, and a hole created, a valence electron from the neighboring bond can "jump" into the empty spot and restore the bond.

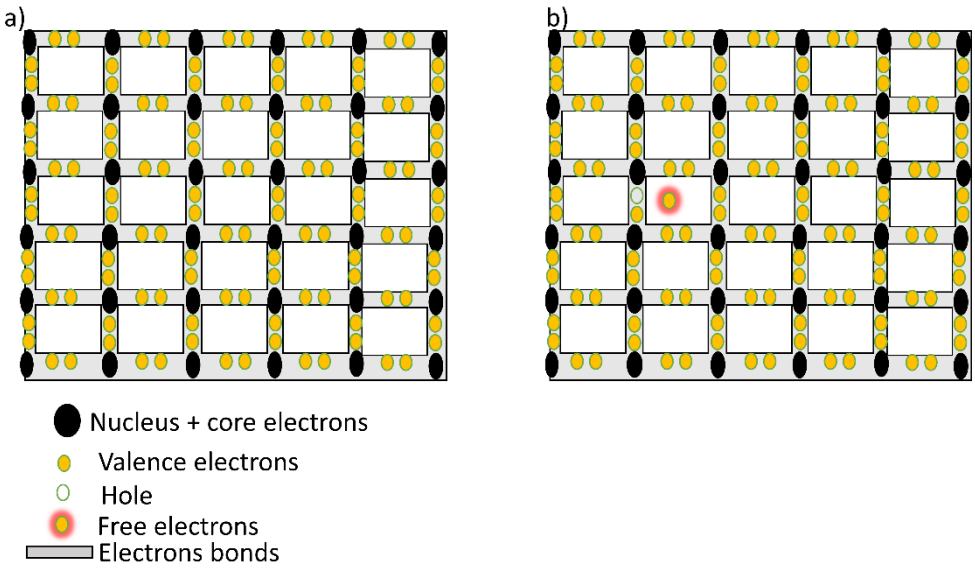

Figure : 16 the bonding model for c-Si, a) No bond is broken. b) A bond is broken between two Si atoms

3.5.2 Doped intrinsic Semiconductor

It can be manipulated the concentration of holes and electrons in intrinsic Semiconductors, which have high resistance, by the concept of doping to make them extrinsic. The conductivity is changed by the number of impurity atoms that will substitute the intrinsic material. Therefore, extrinsic semiconductors are the most materials used for the manufacturing of electronic devices such as transistors and diodes. If we look in the case of Silicon, the possibility to make it extrinsic is by using pentavalent materials or trivalent materials. Pentavalent materials have five valence electrons in their outermost orbit, such as antimony (Sb), phosphorus (P), and arsenic (As). The trivalent material has three valence electrons in their outermost orbit, namely, Indium (In), Bor (B), aluminum (Al) and gallium (G), those impurities can classify the semiconductors in two categories, P-type and n-type [3]

3.5.2.1 **P-type material**

P-type material is created when we use the trivalent elements to dope Si or Ge. The Si has 4 atoms in outermost shell that can interact with other atoms (Valence electrons). With the aid of bonding, the model can quickly figure out the process of doping. An atom with three valence electron such as (B) cannot form a bond with five valence electron of Si, it can "accept" an electron from a nearby Si-Si bond by the help of thermal energy present in the Si lattice which leads to creating a hole that can move around the lattice. Here we use the term of concentration of acceptor $N_{.A.}$ that makes the intrinsic Si, P-type material Figure.*17-b*.

3.5.2.2 **N-type material**

N-type material is created when we use the pentavalent elements to dope Si or Ge. An atom with five valence electron such as (P) can form a bond with the four valence electron of Si; the fifth atom cannot take place in the process and by the help by the help of thermal energy present in the Si lattice at room temperature it can easily liberate from the phosphorus atom. One the electron is free can move

throughout the lattice" donor." Here we use the term concentration of donors N_D to illustrate to the impurity atoms that make the intrinsic Si, N-type material Figure.*17-a*.

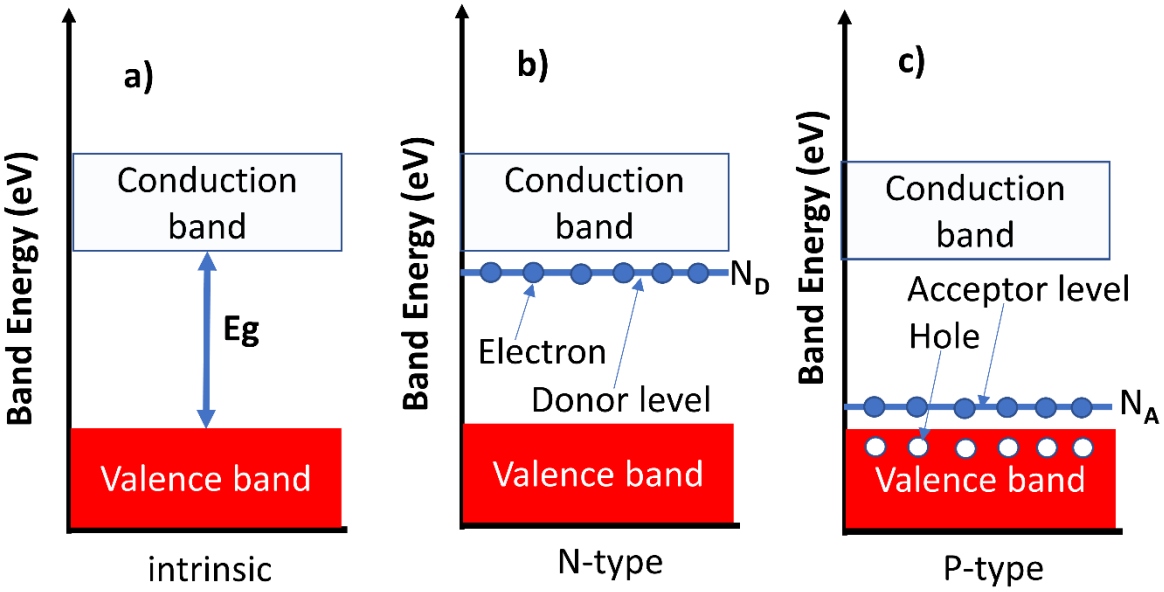

Figure.17: Energy band diagram. a)intrinsic Semiconductor. b)N-type Semiconductor. c) P-type semiconductor

4 Semiconductor junctions

The central concept of all solar cells is around the design of junctions by constructing different materials.

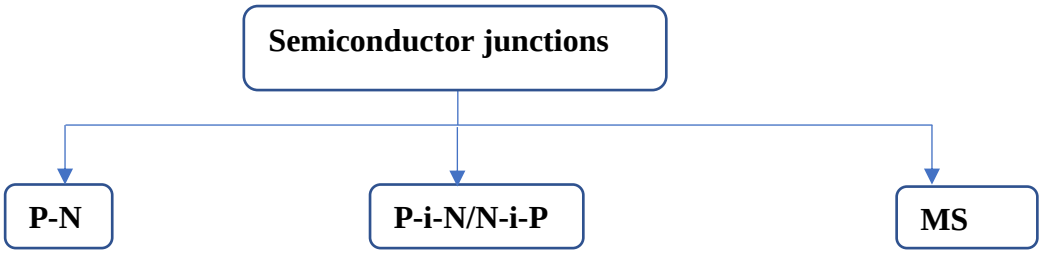

Figure 18 : Semi-conductors junctions

The p-n junction is fabricated from the same semiconductor material is an example of a p-n homojunction. A P-N/N-P junctions that are formed between two chemically different semiconductors are called heterojunction. The second category is called P-i-N/N-i-P, in which an i-layer is inserted between the p-type and n-type layers. Also, there is another junction between Semiconductors and metal is called an M.S. junction.

4.1 p-n homojunction

In isolated semiconductor Figure.19 the n-type is dominant by the majority of electrons and p-type by the majority of holes; when a p-type and n-type semiconductor are grouped, a very large difference in electron concentration between n- and p-type regions leads to a diffusion current of electron toward the p-type region and vis-versa across the" metallurgical junction" denotes the region between the n-and p-type region . as a result the region close to the metallurgical junction becomes

depleted of mobile charge carriers which help to create a space charge is called space-charge region or depleted region. The n-et p-types areas are also called the quasi-neutral regions.

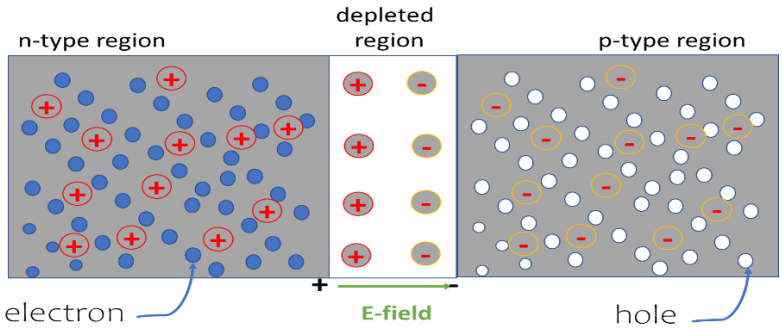

Figure.19: Formation of the space-charge region in p-n junction

An internal electric field is generated in the space charge region, which forces the charge carriers to move on the opposite side than the concentration gradient.

4.1.1 The p-n junction under equilibrium

The note of Fermi energy or the electrochemical potential is constant and independent of position and describes the average power of electrons on both sides. The vacuum level represented in which means the boundary of outside the atom. The electron affinity shows the potential that an electron present in the conduction band requires to be outside the atom.

When we produce p-n junction, the fermi level will be the some across the system, the conduction band E_c and E_v the valence band as well as the vacuum energy must be continuous. When the bands become bent, it means the presence of an electric field that will create an electrostatic potential in the depletion region

4.1.2 The p-n junction under applied voltage

The applying of an external voltage, V_a, to p-n junction leads to change the potential difference between the two regions. The electrostatic potential in the space charge region will become (V_{bi}-V_a) (the built-in the potential is negative in the p-type region). When we applied external bias, positive voltage +Va is called forward bias voltage to a p-n junction leads to decrease the potential difference across the p-n, the band diagram of the p-n junction, either the space-charge region becomes narrower. In the other option, when we applied a negative external voltage, which is called reverse-bias voltage concerning the potential region of p-type, the potential difference across the p-n junction will increase, and the depletion region becomes wider.

The forward-bias voltage creates a higher concentration of minority carriers at the boundaries of the depletion region; this phenomenon is called minority-carrier injection, which creates the diffusion of the minority of carrier to the bulk quasi-neutral region. This process causes a recombination current density, J_{rec}, which is compensated by the thermal generation current, J_{gen} .

At V_a=0, the situation inside the junction can be described as the balance between the recombination and generation current densities,

$$J = J_{rec} - J_{gen} = 0$$

It is assumed that when a moderate forward-bias voltage is applied to the junction, the recombination current density increases with the Boltzmann factor $e^{\frac{eVa}{KbT}}$:

$$J_{rec}\,(Va) = J_{rec}\,(Va = 0)\; e^{\frac{eVa}{K_bT}} \quad (27)$$

4.1.3 The p-n junction under illumination

The situation of illumination of a p-n junction leads to additional electrons and holes in the Semiconductor. The minority carrier of holes and electrons in p-type and n-type respectively increase, leading to flow the minority carriers across the depletion region into the quasi-neutral regions, the electrons from p-type into the n-type region and holes from the n-type region into the p-type region, this processes causes the so-called photogeneration current density, J_{ph}, adding to the thermal-generation current, J_{gen}. The last two types of generation are balanced by the recombination current, which will increase by decreasing the electrostatic potential barrier across the depletion region.

The illuminated p-n junction can be under open-circuit voltage, as discussed in non-equilibrium, the quasi-fermi level of electron E_{Fn} is higher than the holes E_{Fp} by the amount of qV_{oc}, (Voc is the open-circuit voltage).

The p-n junction can be under the short-circuited condition, which leads to the substantial variation of the quasi-Fermi level, but the electrostatic-potential not changed.

$$J_{Va} = J_{rec}(Va) - J_{gen}(Va) - J_{ph} = J_0\; e^{\frac{eVa}{K_bT}} - J_{ph}$$

4.2 P-i-n Junctions

In the p-i-n junction, undoped layer or intrinsic is sandwiched between the oppositely doped selective layers which is the case of PSCs, due to this contact, the band bending created at the interfaces towards the intrinsic region with a constant electric field is generated within the intrinsic layer as described in Figure 20.

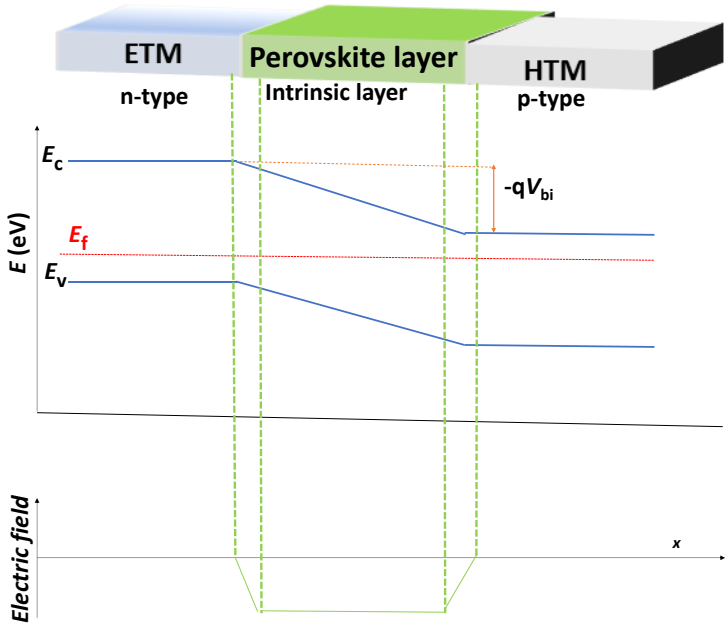

Figure 20 : Band diagram of a device p-i-n using perovskite solar cell.

5 The working principle of a solar cell

The working principle of a solar cell is based on the photovoltaic effect, i.e., the generation of a potential difference at the junction of two different materials in response to electromagnetic radiation. The photovoltaic effect is closely related to the photovoltaic effect, where electrons are emitted from a material that has absorbed light with a frequency above a material-dependent threshold frequency. In 1905, Albert Einstein discovered that this effect could be explained by assuming that the light consists of well-defined energy quanta, called photons[21]. The energy of such a photon is given by :

$$E = hv \quad (28)$$

Where :

Planck's constant

v :frequency

The photovoltaic process can be achieved through three basic steps: 1, 2 and 3

- **Step 1 : Generation of free charges**

All the photons come from solar radiation with a band gap equal or high than the absorber layer can excite an electron from an initial level to a high level, which means from the valence band to the conduction band leads to the creation of an electron-hole pair.

- **Step 2: Separation of the photo-generated charge carriers**

The electron will fall back to the initial energy level, for the last raisons the selective transport layers must be present in both sides of the light harvest , then the electrons can flow out through one membrane and holes can flow out through the other layer, in solar cells these membranes represented by n-type and p-type materials.

- **Step 3: Collection of photo-generated charges carriers**

The final step is done by the performing work in an external circuit made by the charges carriers that are extracted from the solar cells with the electrical contacts. The chemical energy of the electrons hole pairs is finally converted to electric energy. After the electrons have passed through the circuit, they will recombine again.

5.1 Main parameters in Solar cells

The performance parameters of a solar cell mainly related to the output characteristics of the cell (I-V) with short-circuit current, open-circuit voltage, fill factor, and power conversion efficiency, as shown in *Figure.18.*

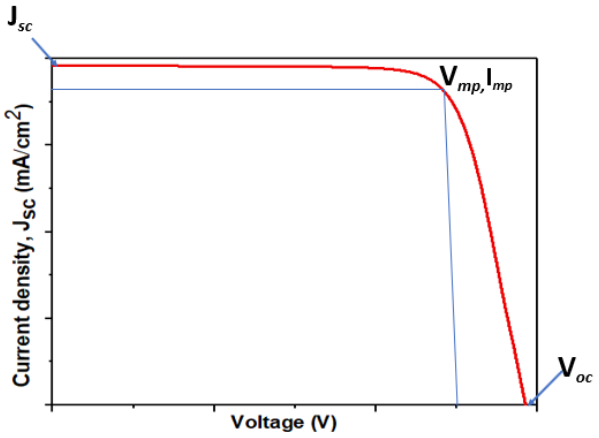

Figure 21: The Output characteristics of solar cell

- **Open circuit voltage**

The open-circuit voltage (Voc) is the maximum output voltage of solar cells. It can be obtained when the value of the output current is zero, which can be described through the equation :

$$Voc = \frac{K_b T}{q} ln\left[\frac{I}{I_0} + 1\right] \quad (29)$$

Where K_b is the Boltzmann constant, T is temperature, q is the elementary charge, I is the light-generated current density, I_0 is the saturation current density.

- **Short circuit-current**

A Standard Light source can illuminate a solar cell when the output is in a short circuit state, which means the voltage value is null. The current is the maximum output current called short-circuit current. It is given as :

$$I_{sc} = I - I_0(e^{\frac{qV}{K_b T}} - 1) \quad (30)$$

- **Fill Factor**

The fill factor (F.F.) is the maximum output power ratio to the open-circuit voltage and short circuit current. the value of F.F. depends on series resistance and voltage, which illustrated by the equation below :

$$FF = \frac{P_m}{V_{oc} I_{sc}} \quad (31)$$

Where P_m is the maximum output power. V_{OC} is the open-circuit voltage. I_{sc} is the short-circuit current.

- **Power conversion efficiency**

The power conversion efficiency is an essential parameter to compare the quality of the cell. It is defined as the ratio of the maximum output power to the incident light power, as shown in the below equation :

$$PCE = \frac{I_{sc} * FF * V_{oc}}{P_{in}} \quad (32)$$

Where Pin is the incident light power. It can be easily seen from this equation that the value of power conversion efficiency is determined by I_{sc}, FF,V_{oc} and P_{in}

6 Perovskite solar cells

6.1 General structure

The general formula ABX3 can explain the ionic structure with a specific spatial distribution of the components. A is a mono/divalent cation, B is a di/tetravalent cation, and X is mono/divalent anion. The first classification of such a crystal lattice arrangement was taken by Gustav Rose, who had found $CaTiO_3$ in the Ural mountains in 1839, and it has been named after the Russian mineralogist and nobleman, Lev Perovski . Over time, it has been discovered that there are hundreds of compositions that make a perovskite structure. It was first described by Goldschmidt [24].

The structure of a perovskite crystal, the constituting ions must fulfill requirements regarding their size and charge. These parameters can be described by the tolerance factor described in different works [25].

Related to Goldschmidt tolerance factor $t = (r_A + r_X)/\sqrt{2}(r_B + r_X)$, where r_A is the radius of the A cation, r_B is the radius of the B cation, and r_X is the radius of the anion. The structure of perovskite in the ranges of 0.8 to 1.0 [26,27] is the most stable.

Related to the structure illustrated in Figure 22, the A cation can be $CH_3NH_3^+$ (MA^+) or $NH_2CHNH_2^+$ (FA^+) , Cs^+ or Rb^+ . The inorganic cation B such as Pb^{+2}, $Sn^{+2,}$ or Ge^{+2}. The X anion can be I^-, Br^- or Cl^-.

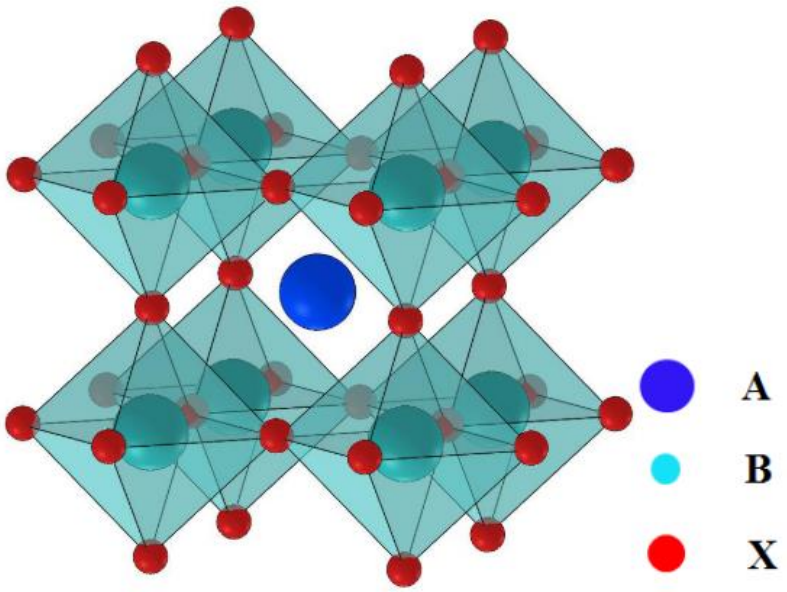

Figure 22: Typical unit cell of ABX3 structure of perovskite material

6.2 Work principal of Perovskite solar cell

In chapter 1, the type of different structure of PSCs was described. The working principle of those structures is illustrated in Figure *23*; the perovskite layer is sandwiched between the ETL and HTL in both configurations. The absorber layer is exposed to sunlight to generate free carriers charges (electrons et holes), then the electrons are separated in the ETL and holes at HTL. Finally, the electrons are collected at TCO and holes at back contact. The TCO and back contact are connected to generate a photocurrent in the out circuit.

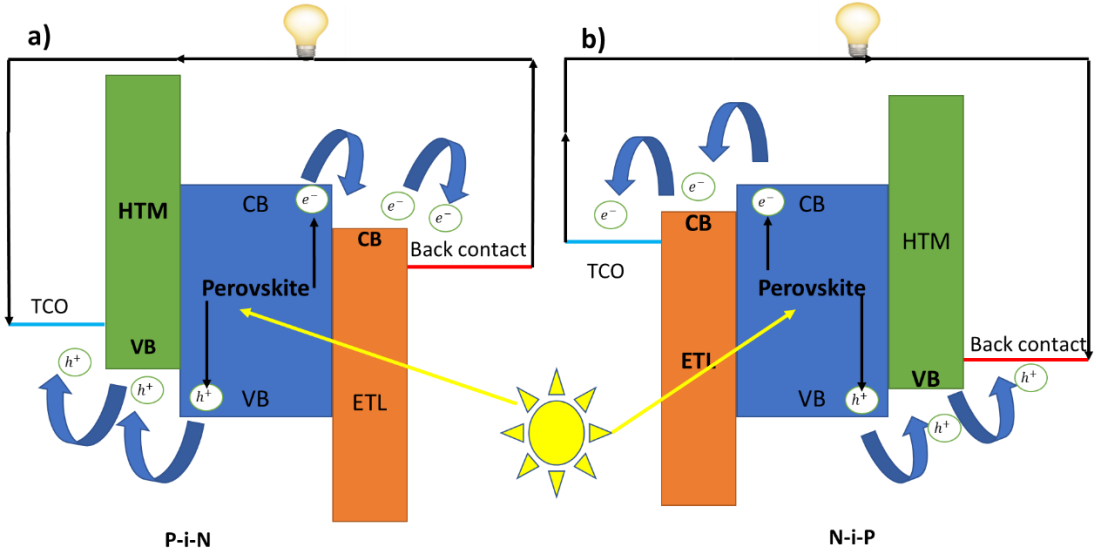

Figure 23: Schematic of the underlying principle work of Perovskite solar cell .a)P-i-N .b)N-i-P

6.3 Progress of perovskite materials as light harvesters

Table 2: the efficiencies of some inorganic-organic PSCs.

Perovskite materials	Band gap (eV)	Configuration	PCE (%)	Ref
$MAPbI_3$	1.52	ITO/PTAA/PVSK/C_{60}/BCP/Cu	20.7	[28]
$FAPbI_3$	1.47	FTO/bl-TiO2/mp-TiO2/PVSK/PTAA/Au	20.2	[29]
$(FAPbI_3)1-x(MAPbBr_3)_x$	NR	FTO/bl-TiO2/mp-TiO2/PVSK/PTAA/Au	18	[30]
$FA_{0.85}\,MA_{0.15}Pb(I_{0.85}Br_{0.15})_3$	1.55	ITO/PTAA/PVSK/C_{60}/BCP/Cu	20.6	[31]
$Rb_{0.05}(Cs_{0.05}(MA_{0.17}FA0_{.83})_{0.95}Pb(I_{0.83}Br0_{.17})_3$	1.63	FTO/bl-TiO2/mp-TiO2/PVSK/Spiro/Au	21.6	[12]

Halide perovskite materials were first used in 1893; since 2009 have taken huge attention after the first application as an active layer in solar cells [9]. Thereafter ,several perovskite materials have discovered with ABX3 formula ,using methylammonium (MA) , formamidinium (FA) ,cesium (Cs) and rubidium (Rb) at cation A sites , lead (Pb)/tin (Sn)/Germanium(Ge) at cation B sites , and halide (I,Br,Cl) at anion X site [12,32–36]. The wide perovskite material used is $MAPbI_3$ due to the band gap

of 1.55 eV, and high absorption coefficient, low-temperature annealing (100 °C), but it degrades in the presence of moisture and air [37]; another choice is using $FAPbI_3$, which shows better thermal stability than $MAPbI_3$ [38]. However, it is still not stable at room temperature (i.e metastable state) yields to fast converting to yellow phase, the Goldschmidt tolerance (t) should be between 0.8<t>1 to stabilize the black phase [18], the Goldschmidt tolerance for $MAPbI_3$, $FAPbI_3$ and $CsPbI_3$ is 0.9, 1 and 0.8 respectively, for these reasons some elements cannot fulfill the requirement of the ideal Goldschmidt tolerance such as K, Na, Ga. The tunability of perovskite materials can make different structure such as $MAPbI_{3-x}Br_x$ as illustrated in Figure.21 [39] , the incorporation of Br in I can change the wavelength from 786 nm to 544 nm for x=0 and x=3, respectively.

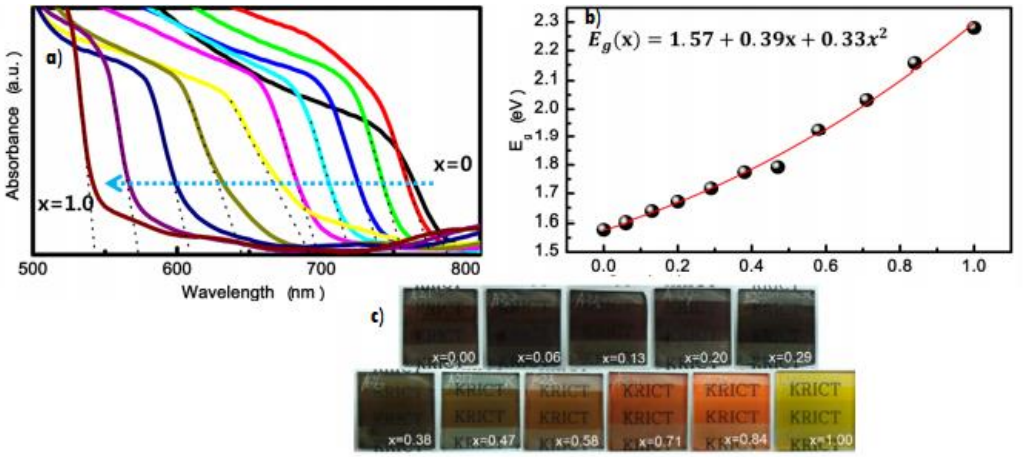

Figure 24: a) The absorption spectral of $MAPbI_{3-x}Br_x$ .b)the band gap of $MAPbI_{3-x}Br_x$. c) the color of $MAPbI_{3-x}Br_x$ [39]

Jeon et al. reported the performance of $(FAPbI_3)_{1-x}(MAPbBr_3)_x$ by varying x from 0 to 0.3[40] , the best amount is found with x=0.15, this structure also shows the better quality and more stability under outdoor conditions [41], but the efficiency still far from the Shockley Queisser limit which our study in chapter 5 will discuss it intensely.

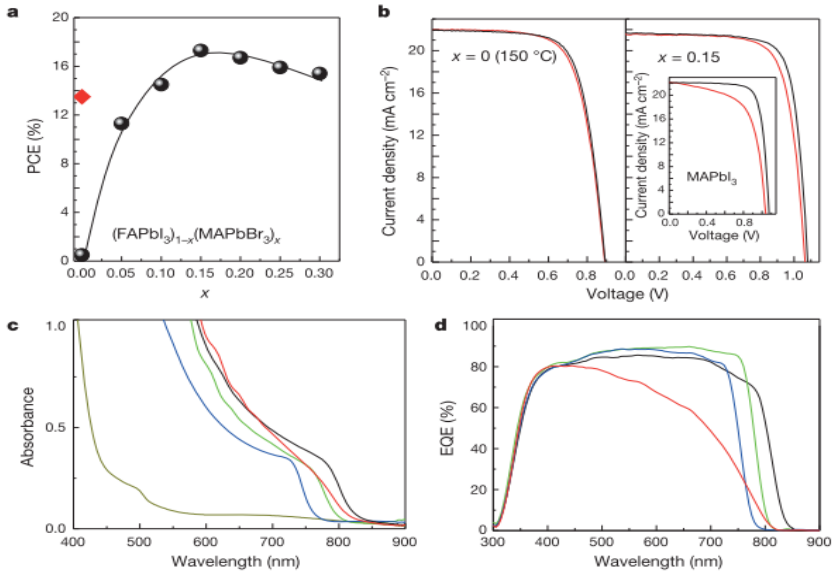

Figure 25: a) The efficiency vs. doping of $(FAPbI_3)_{1-x}(MAPbBr_3)_x$. b) The IV curve of $(FAPbI_3)_{1-x}(MAPbBr_3)_x$ compared to $MAPbI_3$. c) The UV-vs absorption spectra of $(FAPbI_3)_{1-x}(MAPbBr_3)_x$. The External Quantum Efficiency of $(FAPbI_3)_{1-x}(MAPbBr_3)_x$ [41].

6.4 Electron transport materials (ETLs) :

After the separation of free charges in the absorber layer, the turn comes on ETL to make the transfer of electrons to the anode; in this context, the ETL should be an n-type semiconductor with transparent in the visible light adding to excellent mobility and conductivity to create a better transfer of electrons.

6.4.1 Inorganic ETLs

- **Titanium dioxide TiO_2**

Titanium dioxide becomes the traditional ETL in PSCs, its C.B. approximately in the range of 4–4.1eV in case of anatase and rutile phase, with a band gap roughly to 3.2 eV [42] and 3eV [43] respectively. Its perfect band alignment with the perovskite material such as $MAPbI_3$ makes TiO_2 the must ETLs studied in PSCs, the highest performance achieved in PCSs made by mesoporous or compact TiO_2. However, it had many disadvantages, such as the quest for stability under U.V. illumination, high processing temperature, low mobility, and upper trap density. It opened the door for new investigations that can replace TiO_2 .

- **Zinc oxide ZnO_2**

ZnO can prepare by low processing temperature, has a high band gap, and considerable electron mobility due to those advantages [44]. Bi Dongqin et al. in 2013 reported for the first time the application of ZnO in PSCs as an alternative for TiO_2 [45]. Still, its efficiency is low around 5-8 %, due to defects and recombination with the perovskite material, the same approach with TiO_2 called again, by doping method it can reduce those disadvantages, nitrogen-doped ZnO (N: ZnO) demonstrated a PCE of 16.1 % with hysteresis free [46]. Still, the issue of chemical degradation at ZnO/Perovskite hinders its application for PSC[47].

- **Tin Oxide SnO_2**

Recently SnO_2 had got more attention in PCSs due to its proper mismatch alignments with the perovskite layer, which enhances the transport of free charges in solar cells. Also, the high mobility and conductivity compared with TiO_2 and ZnO lead to reduce the recombination loss. SnO_2 has a wide band gap (3.6-4 eV) and high transmittance in the visible region, which can facilitate crossing the high amount of light to the perovskite layer.< 200 C can be used to prepare SnO_2, which good point in the case of flexible or tandem solar cells[48][49]. The efficiency of SnO_2 in PCSs have started by 7.43 % by Ma et al. [50] and reached 23.3 % [51]

- **Zn_2SnO_4 (ZSO)**

ZSO is another competitive ETL for PSCs. For many reasons, such as wide optical band gap 3.8 eV, high mobility, proper alignment with the energy level of perovskite, and the most important chemical stability for polar solvents used in processing fabrication [52]. ZSO demonstrated excellent stability for PSCs without encapsulation, even its PCE, around 13 %, to boost its performance should more focus on the interfacial defect. A PCE reached 17.8 % when rGO used with nanofiber ZSO [53].

6.4.2 Organic ETLs

The organic ETLs have taken a massive interest in PSCs, to modify the surface of Inorganic ETL with the n-i-p structure or used directly as ETL in p-i-n structure, due to their optoelectronic proprieties, suitable energy level alignment, easy low-temperature solution-processed or vacuum-processed processing [54].

Among these family, fullerene and its derivatives (6,6]-phenl-C61-butic acid methyl ester (PCBM) or C60) are widely used depending on the structure of PSCs as mentioned previously.

Yoon et al. achieved a PCE of 19.1 % with hysteresis free using vacuum-processed for C60 ETL, and also they demonstrate excellent stability when used PEN substrate as a flexible substrate [55].

Perylene diimides (PDIs) have used as ETL for the n-i-p structure which can provide excellent thermal stability and high electron mobility, the first performance was only 7.93 % [56] but when the amino-substituted the PCE reached to 17.66 % and 14.32 % on glass/FTO and PET/ITO respectively, this improvement due to the amino-group which can reduce the work function of FTO and improve the morphology of the interface with the perovskite [57].

Organic ETLs have taken more attention for inverted planar PSCs structure p-i-n, which PCBM demonstrate a PCE around 20 % [58]; these achieving are going in parallel with solving the issues of band tail, low electron mobility, morphology, and stability of PCBM. The fullerene-based inverted planar PSC has low V_{oc}; Huang and co-workers used a solvent annealing to boost the *V*oc by 50mV, which makes better trap density [58]. The crosslinking silane layer can also be a good strategy by adjusted to fullerene layer yield to large V_{oc} [59].

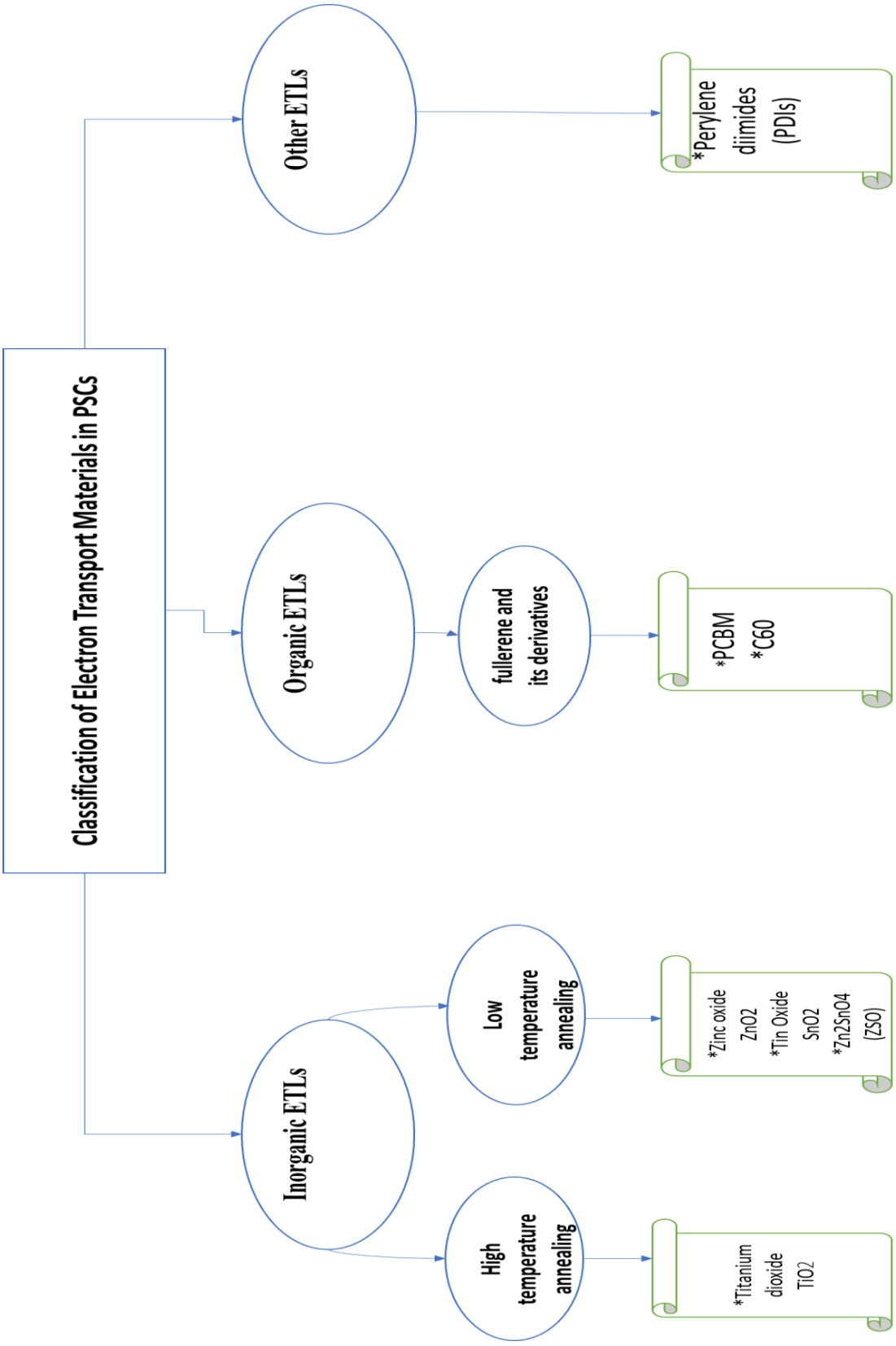

Figure 26: Schematic diverse Electron Transport layer is using in perovskite solar cells

6.5 Hole Transport Layer

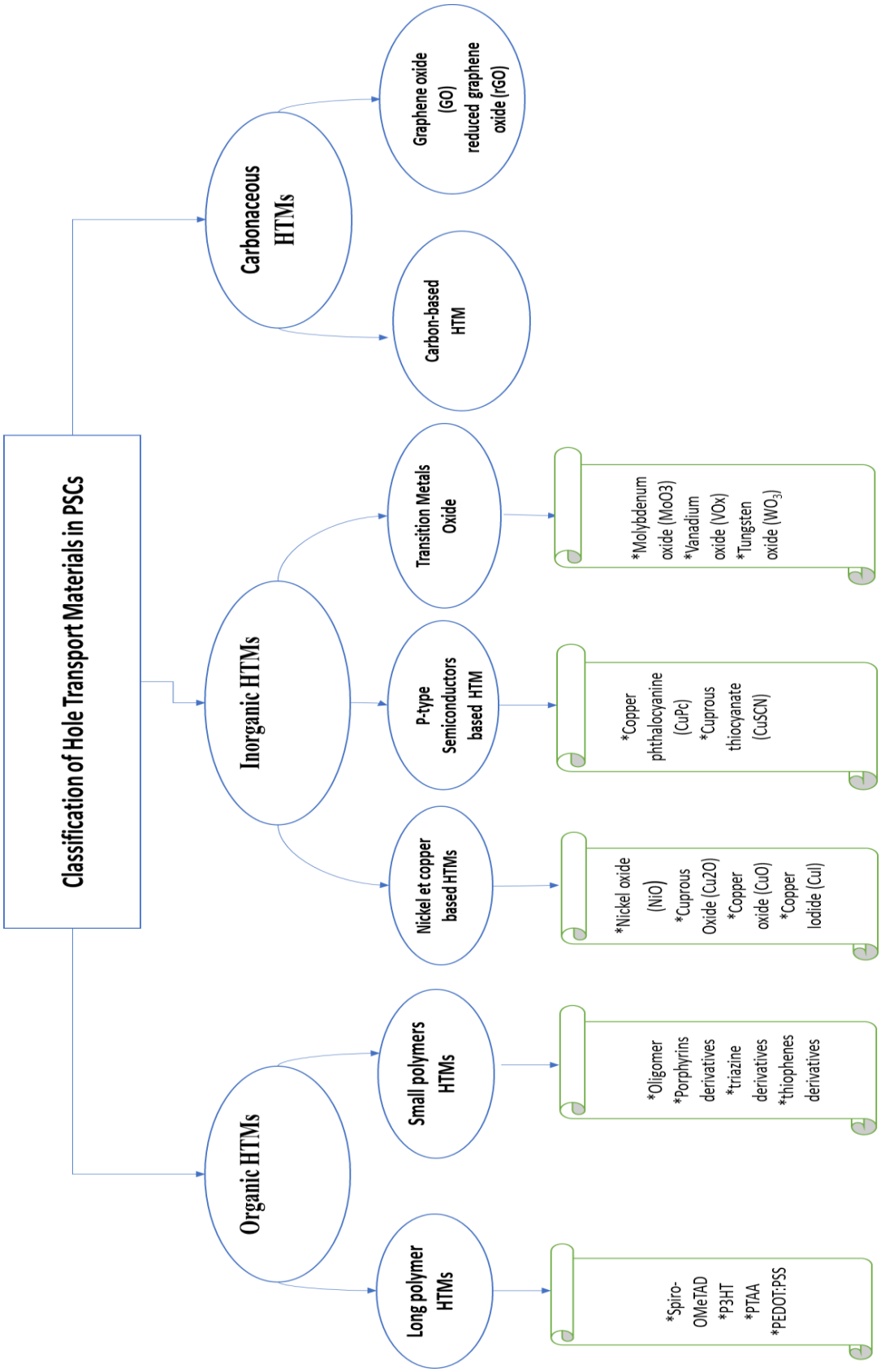

Figure 27: Schematic diverse hole Transport layers are using in perovskite solar cells.

6.5.1 Organic HTLs

6.5.1.1 Long polymer HTLs

- **Spiro-OMeTAD**

The Spiro-OMeTAD has been one of the successful HTLs in perovskite solar cells, with an efficiency exceeding 20 %; it was the common point when park et al. succeeded in eliminating the liquid electrolyte that used in solid-state de sensitized solar cells (s-DSSCs)[60].

Due to low mobility and conductivity in bulk Spiro-OMeTAD [61], dopants such as lithium bis trifluoromethylsulphonyl) imid (Li-TFSI) and 4-tert-butylpyridine (TBP) added to improve its proprieties owing to these efforts, the Spiro-OMeTAD still suffer from low conductivity and mobility, with high degradation after adding the previous dopants. Also, it is expensive, which harmed the commercialization of PSCs.

To balance the cost and stability with high performance, the polymer HTLs are also employing to replace the small molecules HTLs.

- **P3HT**

This competitive material used for the first time with organic solar cells,7 % was the start record in PSC [62], various efforts are made to enhance the morphology, the mobility and thickness resulted in a PCE of 15 .3 % [63,64], but this results need more investigation in term of experimental and theoretical calculations.

- **PTAA**

Owing to its higher hole mobility (10-2_10-3 cm2V-1s-1), PTTA is starting as successful HTL in PSCs, 12 % was the first PCE reported[65,66] based on divers optimization, the record of PEC attainted 20.2 % and more advantage can offer this inorganic material such as high molecular weight and couldn't pantry in the perovskite layer compared with Spiro.

- **PEDOT: PSS**

PEDOT: PSS one of the successful polymer HTLs in PSCs regarding its work function compared to MAPbI3 and transparency, it can allow arranging planar or inverted structure and also this HTLs can adapt with flexible PSCs for low-temperature treatment[67], modified the PEDOT: PSS can enhance its proprieties as Luo et al. demonstrated a PCE of 17 % by introducing graphene oxide (G.O.) [68], controlling the level energy and surface morphology of other layers can push the efficiency of PEDOT: PSS more than the previous value.

- **Small polymers HTLs**

From the above conditions, various small molecule HTLs had been tried as an alternative for Spiro-OMeTAD to push the efficiency and stability, such as oligomer HTLs[69], porphyrins derivatives, triazine derivatives, thiophenes derivatives, and pyrenes derivatives[70–72].

6.5.2 Inorganic HTLs

Even the inorganic HTLs can attend more than 15 % as PCE in PCSs but still suffer from the low hole mobility, the degradation under the humidity after adding the dopant to bulk state and are costly. For these reasons, many inorganic HTLs are investigated.

- **Nickel oxide (NiO)**

The challenge of NiO as inorganic HTL is started by Irwin et al. [73] when they made it as P-type instead of PEDOT: PSS demonstrated a proper matching with the valence band of perovskite and good conductivity that's open the door for more investigation. Among great effort by controlling the method of deposition of the film, tunneling the proprieties of the perovskite layer, and stacked another layer with NiO, to minimize the mechanism loss between the layers impressed the efficiency to 13% with Voc=1.04 V [74], Seok et al. reported the highest PCE 17 % and Voc =1.06 V near to 1.11 V that found by Spiro-OMeTAD[75].

- **Cuprous Oxide (Cu2O) & Copper oxide CuO & Copper Iodide**

Copper and its derivatives tried to be alternative to inorganic HTLs in PSCs due to its wide band gap, high conductivity, and simple synthesizing methods.

Cuprous, copper, and cupric oxides (Cu_2O , CuO, and CuI) have a bandgap of 2.1-2.6,1.3-2 and 2.9-3.1 eV, respectively, and high mobility more than (100 $cm^2V^{-1}s^{-1}$) [76–78].Cu2O, CuO_x, and CuI are used as HTL in PCSs and demonstrated a great PCE of 17 % [79], 17.43 % [80], and 13.35 [81]%, respectively. To be close to the performance of inorganic HTLs should be call effective synthesizing methods and more optimization in the case of material proprieties.

- **P-type Semiconductors HTL (Copper phthalocyanine CuPc & Cuprous thiocyanate CuSCN)**

Due to its low cost and moderate mobility, Kuma et al. applied CuPc as HTL in PSCs and achieved 5 % [82]. Its efficiency attends 16.1 % and high stability with printable PSCs, which the Carbone (C) as an electrode is used [83].

CuSCN is cost-effective, adding to its stability and high optical transparency [84]. The PCE of PSCs increased from 12.4 % to 17.01 % with pristine absorber layer and CuSCN [84–86] that's confirmed CuSCN can be a promising HTL candidate for PSCs.

6.5.3 Transition Metals Oxide

Transition Metals Oxide had been used in organic solar cells in the first stage, due to degradation of organic HTL in ambient condition, many researchers are focusing on transition metal, such as dopant for several reasons, their high work function, and conductivity, transparency[87].

- **Molybdenum oxide (MoO3)**

The high work function, non-toxicity, and smooth surface as advantages of MoO_3 , for those proprieties Kim et al., applied MoO_3 in PSCs , resulting in high voltage 1.12 V and 13.7% then its efficiency increased by 14.78 by Hou et al. when used MoO3:PEDOT: PSS as HTL in inverted planar and also it has been shown a significant improvement in the stability[87–90].

- **Vanadium oxide (VOx)**

VOx has been used in PSCs as pristine or interfacial layer due to its low cost, low-temperature processing which good point for large scale, its efficiency started by 14.14 % in inverted PSCs with negligible hysteresis was reported by Haochneg et al. [91], then a PCE 17.5 % and 1.05 V were showed

by Haitao et al. [92] which V2Ox sandwiched between Perovskite and PEDOT: PSS, also a PCE around 15 % reached by Wang, Dian, et al. with bilayer V2O5 :PEDOT: PSS as HTLs[93]

- **Tungsten oxide (WO_3)**

WO_x is also a promising low-temperature inorganic HML, Zhiwei et al. succeeded to report a PCE of 7.68 % by a solvothermal method in inverted PSCs [94],WO_x showed high hole mobility and highly transparent in the visible region [95], a PCE of 9.8 % also reported by Zong-Liang et al. when UV-ozone used to treat its surface for better coverage of perovskite material[96].

- **The carbonaceous hole-transporting materials (Carbon/graphene oxide/reduced graphene oxide)**

The carbon started in PSC as an electrode (back contact) to replace the expensive electrode gold (Au), but in 2014 Yang et al. have demonstrated that the carbon can be an electrode and HTL. The graphene oxide (G.O.), reduced graphene oxide (RGO), and carbon nanotubes (CNTs) can offer many advantages such as low cost, best alignment matching with the perovskite. Also, better mechanical performance can produce less interfacial resistance. Furthermore, carbon-based material can be prepared easily by spin coating, the doctor blade method, ink-jet printing[97][98].

6.5.4 Carbon-based HTL

Zhou et al. have succeeded in fabricated low and straightforward cost configurations of PSC without HTL based on Carbon as HTL. It delivered efficiency of 8 % [99]; after these impressive results, many studies have focused on the preparation of the carbon as an electrode for avoiding the damage of perovskite film, such as Zhang et al. reported low temperature-processed carbon paste with superb efficiency of 8.31 %[100]. On the other hand, the optimization of the interface between the carbon and the perovskite yield to achieve an exceeding PCE of 11%[101] and efficiency of 13.58 % also reported by Wei et al. [102] using thermoplastic carbon film.

6.5.5 Graphene and doped graphene oxide-based HTL

The graphene oxide (G.O.) and reduced graphene oxide (rGO) are two-dimensional materials arranged with carbon atom monolayer, those materials have demonstrated high conductivity, mobility and transfer charges make them as a right choice for PSCs to replace the organic HTLs [103].

Firstly as we discussed in organic HTLs, the G.O. has introduced as a buffer layer with PEDOT: PSS[68] with a PCE of 13.1 %, the best line of G.O. in PSCs is a dual function layer. rGO have tried for the first time by Yeo et al. yield to 10.8 % as a PCE and excellent stability [104] due to high conductivity, better alignment, and growth on the surface with the perovskite layer.

7 Fabrication Methodologies of perovskite solar cells

The quality of the perovskite layer has a strong effect on the performance of the cell. Controlling the crystallinity, morphology, phase purity, and uniformity of the absorber layer are essential tips to make a high performance of PSCs.

7.1 Deposition of the perovskite layer

There are two methods to make perovskite film; the first one is based on one step, in case of $MAPbI_3$, the PbI2 is coated firstly then MAI infiltrated in PbI_2 following by drying remained solvent and chemical at specific temperature and time to get perovskite phase. This method has a big issue that

produces a bench of a pinhole in the perovskite layer. To solve this problem a second method is applied to make perovskite layer is called two-step solution method based on solvent engineering as shown in Figure *28*, which (MAI, FAI or CsI,) and (PbI_2, SnI_2 or GeI_2) are dissolved in polar aprotic solvents such as N, N-dimethylformamide (DMF), dimethylsulfoxide (DMSO) to make the precursor solution. The perovskite film can be prepared by the spin-coating of the precursor solution on the substrate. During the spinning, the antisolvent is dropped in the center position of the rotating substrate following by postdeposition annealing on a hotplate to produce perovskite film. Several parameters can affect the quality of the film, such as precursor composition, processing temperatures and times, environment conditions (oxygen and humidity levels), substrate material, and deposition parameters [105,106][107].

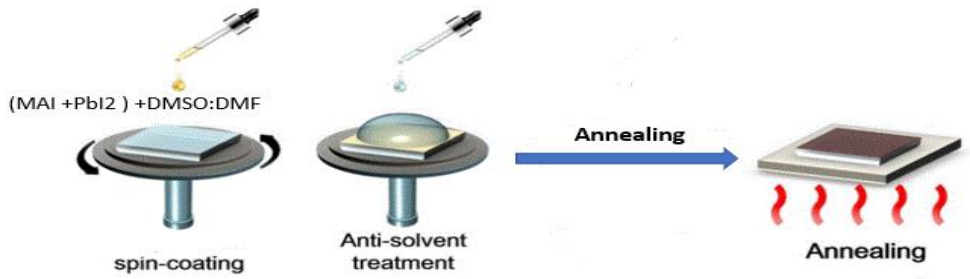

Figure 28: Preparation of $MAPbI_3$ using anti-solvent engineering method

The antisolvent method is sensitive because it is done by hands and needs a long time to master it for producing high quality of perovskite film.

7.2 Fabrication processes of Perovskite solar cells.

The processes of fabrication PSCs will start by the cleaned the ITO or FTO substrates with detergent, deionized water, acetone, and isopropyl alcohol in an ultrasonic bath for 15 min, respectively.

- For N-i-P planar PSCs :
- The cleaned substrates will be treated by oxygen plasma for a specific time.
- The HTL will spin-coated on the cleaned substrates.
- The substrate will anneal with specific temperature and time
- The substrate will transfer to the glove-box, and the perovskite precursor solution will spin-coated at specific rpm and time using antisolvent.
- The substrate will anneal again with specific temperature and time.
- The HTL will spin-coated on the perovskite film.
- The back contact of the cell will be sequentially evaporated by thermal evaporation under vacuum.
- The same processes for P-i-N just instead of stating by ETL will use the HTL first, then Perovskite film, ETL, and finally, the back contact.

For P-i-N, the same process is repeating just instead of starting by ETL; the HTL will be the first layer as shown in Figure *29*.

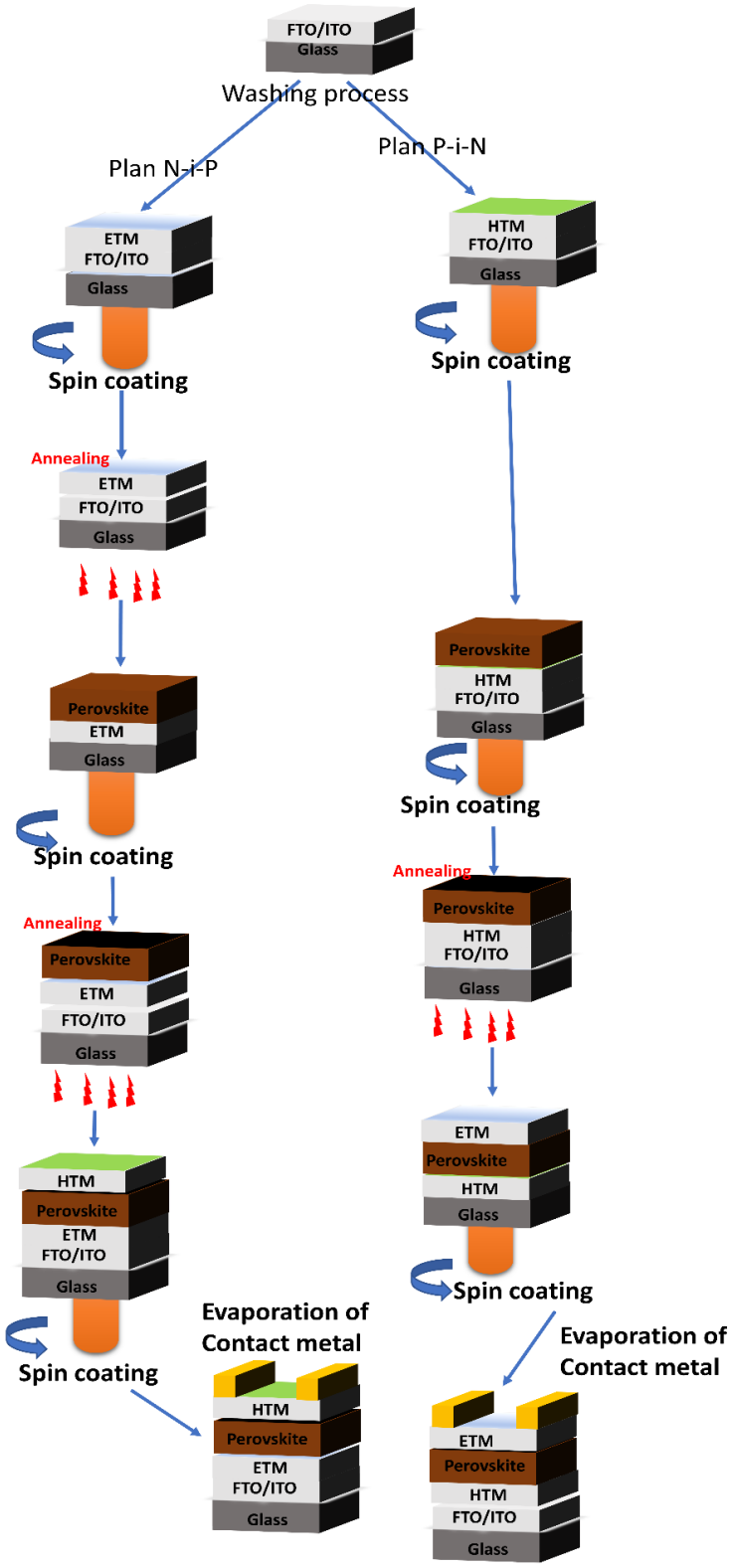

Figure 29: Schematic procedures of PSCs for and N-i-P and P-i-N

Chapter 3: Research Methods and Materials

This chapter is dedicated to mentioning the research methodology used in this work. In particular, in the first part, the numerical simulation was described by showing the method working of SCAPS software. Secondly, the experimental investigation that adopted in this work will describe.

1 Numerical window simulation

There are different commercially available software and educational software for numerical analysis of solar cell that solves these basic semiconductor equations. The list of software that is available free for educational purpose is listed below

- SCAPS-1D (Solar cell capacitance simulator)
- AMPS-1D (Analysis of Microelectronic and photonics Structures)
- AFORS-HET (Automat For Simulation of Heterostructures)
- PC1D
- ASA (Amorphous Semiconductor Analysis)

It very hard to choose between all those tools, we decided to continue with SCAPS-1D to perform our works because SCAPS is extensive literature available and a lot of experts in the PSCs have used it [16].

1.1 SCAPS-1D

SCAPS is a one-dimensional solar cell simulation program developed at the Department of Electronics and Information Systems (ELIS) of the University of Gent, Belgium from Marc Burgelman, Alex Niemegeers, Stefaan Degrave, Johan Verschraegen.

The most recent version 3.3.07, includes :

✓ All physical parameters required for solar cell ε_r is dielectric constant, E_g is bandgap, χ is electron affinity, N_c is effective conduction band density, N_v is effective valence band density, μ_n is electron mobility, and μ_p is hole mobility, N_D is donor concentration, while $N_{.A.}$ is acceptor concentration, N_t is the defect density, Capture cross-section fo electrons, and holes.

✓ Recombination profiles in solar cell (SRH, Auger) .

✓ Defect density in the bulk of Semiconductor and at the interface.

✓ Defects with charge type

✓ The work function of the back and front electrodes

✓ Illumination of working structure with different spectra available in the literature (AM0, AM1.5D, AM1.5G, monochromatic, white)

✓ Different kind of lighting from the back or front of the cell.

✓ Performing simulation under batch setting with controlled iteration.

✓ Run simulation using Script

✓ Saving materials and structures.

✓ Calculate : (Energy band diagram, I-V cure, C-V cure, Quantum efficiency, Built-in voltage , recombination profile with temperature).

✓ Highly recommended interface.

1.2 Tips of simulations

1.2.1 Literature preparation

Before start running simulation, considerable research should be done to find all parameters that show in Figure *30.*

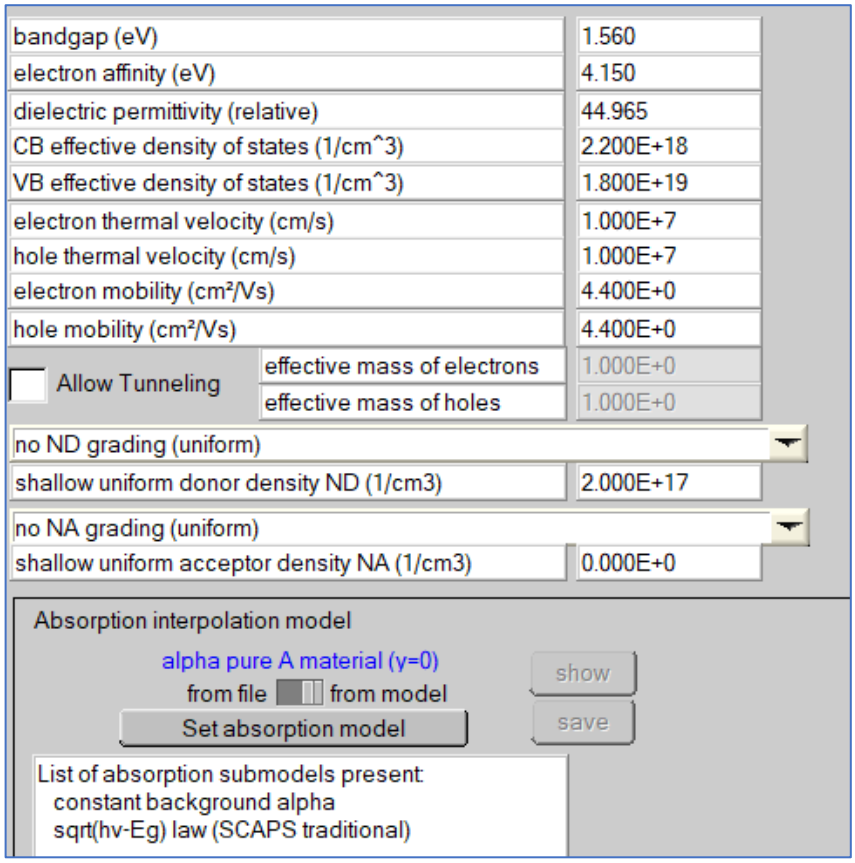

Figure 30: SCAPS Window of electrical parameters

Those parameters are mandatory for each layer, i.e., for ETL, HTL, and perovskite layer.

In our case, we found some parameters from the previous studies, and also we used some settings from our experimental studies.

1.2.2 Absorption coefficient

In the new version of SCAPS >3.3.07, there are two methods to fit the parameter of the absorption coefficient; the first one is given by the sub-model below :

$$\alpha(hv) = (+)\ \alpha_{bg} \quad back\ ground \qquad constant\ \alpha \quad (33)$$

$$(+)\ \alpha_c\ u(hv - E_g) \qquad E_g - step\ \ \alpha_c\ if\ hv > E_g, 0\ if\ hv < Eg \quad (34)$$

$$(+)\ \left(\alpha_0 + \beta_0 \frac{E_g}{hv}\right)\sqrt{\frac{hv}{E_g} - 1} \qquad E_g - sqrt \qquad and\ 0\ if\ \alpha_c\ if\ hv < E_g \quad (35)$$

$$(+)\ \left(\alpha_0 + \beta_1 \frac{E_{g1}}{h\nu}\right)\left(\sqrt{\frac{h\nu}{E_g} - 1}\right)^{n1} \quad power1 \quad and\ 0\ if\ \alpha_c\ if\ h\nu < E_{g1} \quad (36)$$

$$(+)\ \left(\alpha_0 + \beta_2 \frac{E_{g2}}{h\nu}\right)\left(\sqrt{\frac{h\nu}{E_2} - 1}\right)^{n2} \quad power2 \quad and\ 0\ if\ \alpha_c\ if\ h\nu < E_{g2} \quad (37)$$

$$(+)\ \ exp\left(-\frac{E_g - h\nu}{E_0}\right) \quad sub - bandgap \quad (38)$$

The singe (+) means here that the sub-model can be added or canceled by the user to the total $\alpha(h\nu)$ in the SCAPS user interface [108].

Where A et B are the absorption constants, h is Planck's constant,v is the light speed.

The second option is to export the file of absorption from the experimental fabrication of each layer.

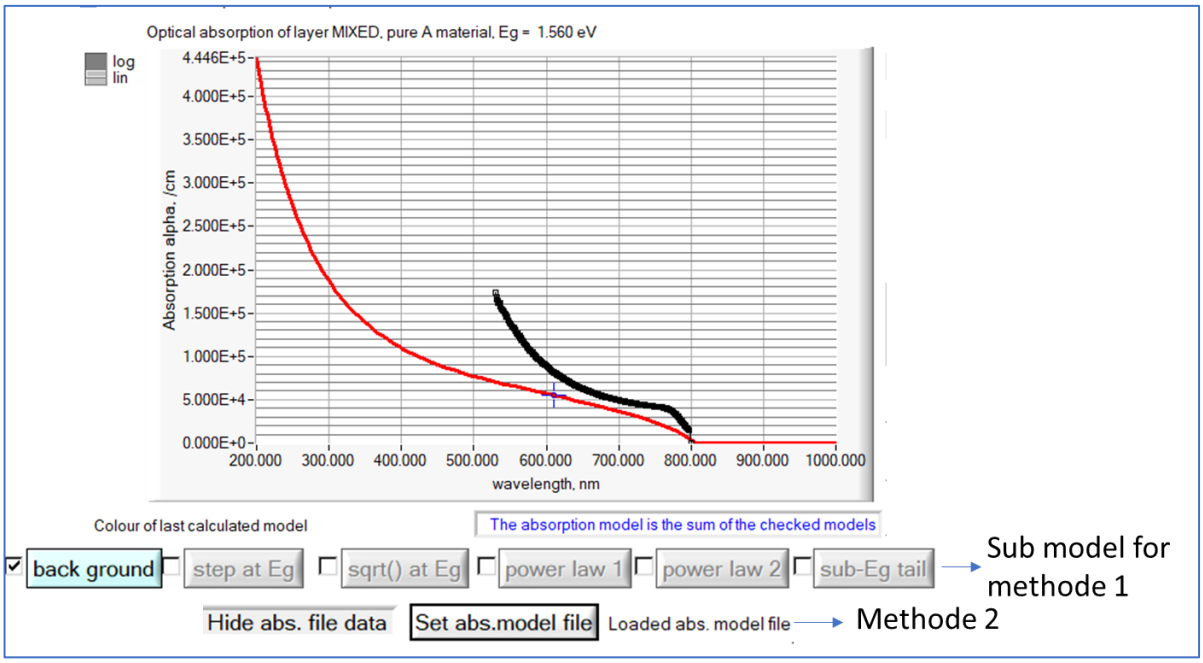

Figure 31: User interface for absorption in SCAPS

1.2.3 Recombination model

There are three recombination models used in SCAPS,

- band-to-band recombination
- The Shockley-Red-Hall (SRH) recombination
- Auger recombination

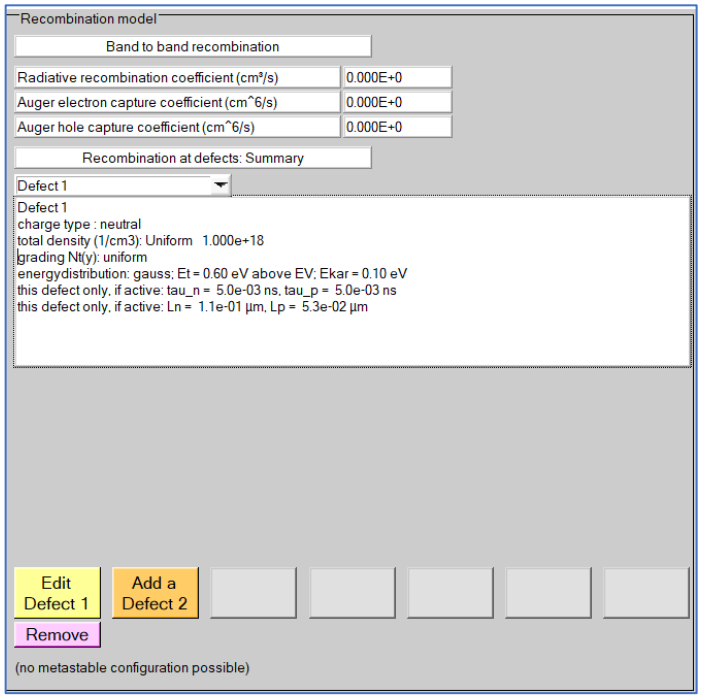

Figure 32: Recombination model in SCAPS

All those tips should be done for each layer. Our methods also are suggested to use two interfaces in case of perovskite layer by adding two-layer with 10 nm, which can make the performance of the study of the cell more accurate to the experimental environment.

1.2.4 Back and front contact

In case of front and back contact, the work function is an essential input to complete making the solar cell,

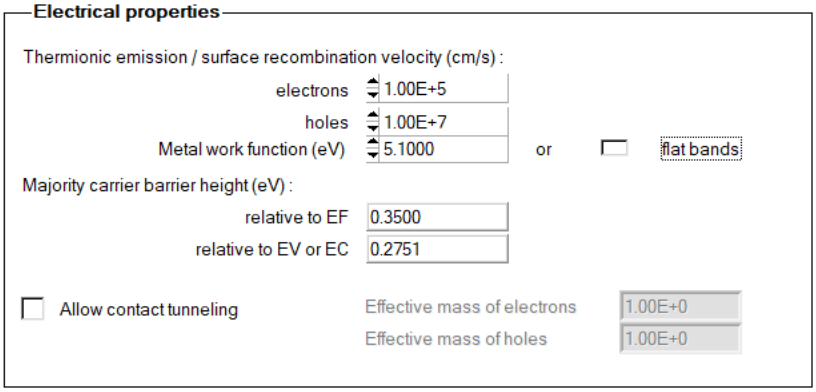

Figure 33:Input parameters of back contact in SCAPS.

After completing all these steps, then our PSCs, Figure *34,* is ready to deliver its performance with all other results.

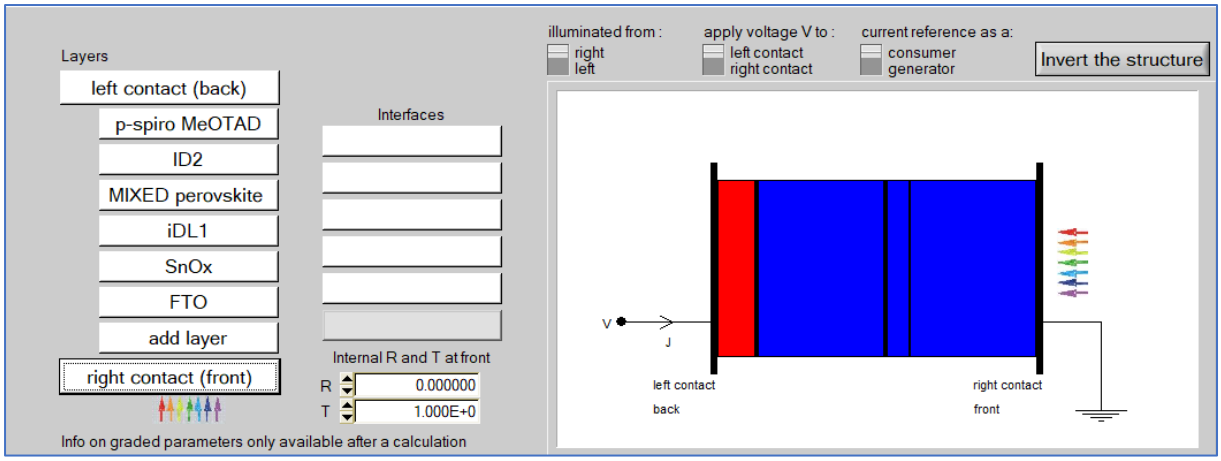

Figure 34: Final structure of PSCs in SCAPS

Then we should come back to the main interface to simulate the working point desired, as illustrated in the following fig.

Figure 35: Main parameters to simulate SCAPS

1.2.5 Results

We can analyze all the results that we need to perform our PSCs. All the results also had a data list that can take it from software by selecting them first then press CTL+C to move them out of SCAPS, which can plot them again with different tools.

1.2.6 Algorithm of SCAPS

The leading theory of SCAPS-1D is to solve Poisson's equation and continuity equations. Every round of calculation begins from the start point, by using the initial assumption, which is expressed by using quasi-Fermi levels, to obtain the equilibrium state, which means no illumination and voltage are applied. When the work point is set in a dark condition, the equilibrium condition is referred to the calculations . When it is placed under a light condition, the short circuit situation will be calculated, and this new value will be used as the initial value of the next step.

The convergence of the Gummel type iteration scheme with the Newton-Raphson algorithm is used in SCAPS for numerical calculations. After a calculation point is set, SCAPS will follow the Newton-Raphson algorithm to undertake iteration calculation until obtaining the optimization value

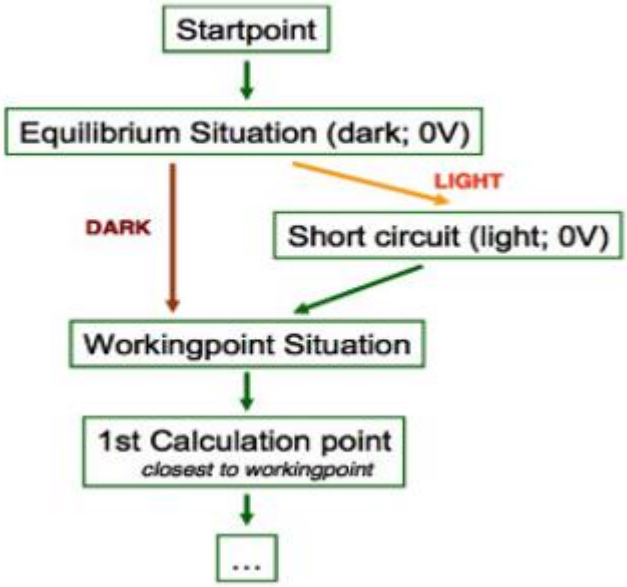

Figure 36: Working strategy of SCAPS.

.

2 Experimental investigation

2.1 Deposition Method

The solvent engineering method was applied for the preparation of perovskite film inside the glove-box with proper condition of O_2 and H_2O and temperature.

Some instruments which are mandatory for making all the process of fabrication are placed inside glove-box, such as spin-coater and the hot-plate.

The sping coating method also was applied to prepare ETL or HTL inside or outside the glove box depends on the desired goal of the fabrication.

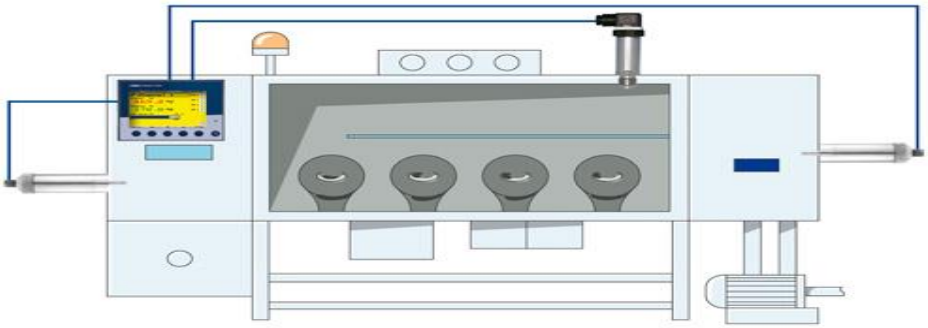

Figure 37: depict scheme of the operation principle of glove-Box

Figure 38: depict scheme of glove-Box

Figure 39: Depict scheme of spin-coater

2.2 Characterization Techniques

2.2.1 Structures studies X-Ray Diffraction

The orientation crystal of materials was analyzed by XRD (Shimadzu 6000) using Cu-K_α target and radiation of wavelength 1.5406, the patterns of XRD were recorded at a scanning rate of 5 (deg/min) , applied voltage and current of the target are 40 (kV) and 30 (mA) , respectively. The structure of materials was investigated with peak positions (2θ-values).

2.3 Morphological studies

2.3.1 Scanning Electron Microscope

The shapes of the perovskite crystals materials are studied by the image of Scanning Electron Microscope (SEM), using 100kx as magnification and 500kx, high voltage 10kv, and SEM in secondary electron mode.

2.3.2 Optical properties studies

The absorption and transmittance of the film-coated is measured at room temperature using U.V./Vis/I.R. spectrophotometer (PerkinElmer Instrument)

2.4 Photovoltaic parameters of PSCs

The testing of the I-V curve of the cell was done by using a photovoltaic measurement system, which is composed of Oriel Solar simulator (Vera Sol LED), Keithley model 2400 digital source meter, and a computer for storing data. The solar simulator is equipped with a 450 W xenon lamp. The output power is managed to match AM1.5 global sunlight (100mW cm^{-2}). For photovoltaic testing system there are three standards that define solar simulator performance (International Electrotechnical Commission (IEC) 609004-9 Edition 2 (2007) (Photovoltaic Devices)), (Japanese Industrial Standard (JIS) C 8912-1998 (Solar Simulators for Crystalline Solar cells and Modules)) and American Society for Testing and Materials (ASTM) International E 927-05 (2005) (Specification for Solar Simulation for Terrestrial P.V.)[109]

Chapter 4: Performance analysis of $MAPbI_3$ based perovskite solar cells employing diverse charge selective contacts: Simulation study

ABSTRACT

The rapid development in organo-metal halide perovskite solar cells (PSCs) has led to the report of power conversion efficiency of 25%. However, their large-scale deployment and possible commercialization endeavor are currently limited due to the presence of high-temperature processed electron transport material (ETL) such as TiO_2 and the expensive hole transport material (HTL) in the state-of-the-art devices. By employing Solar Cell Capacitance Simulator (SCAPS)-1D, we attempted to propose low-cost charge selective materials as ETL and HTL, which can deliver high photovoltaic performance. For this, the evaluation of TiO_2, ZnO, and SnO_2 as ETLs was validated. Besides this, the role of the thickness of ETLs was also investigated in perovskite solar cells using $CH_3NH_3PbI_3$ perovskite as light harvester and Spiro-OMeTAD as HTL. Our simulation results showed that 90nm of SnO_2 layer outperforms as ETL for device fabrication. The impact of ETL thickness on the fill factor was also studied as a function of dopant donor concentration (N_D). Furthermore, in our pursuit to avoid the usage of Spiro-OMeTAD, different organic and inorganic HTLs (P3HT, $CuSbS_2$, Cu_2O, CuSCN) have been investigated, and more importantly, the HTL thickness was optimized for high-performance solar cells. We have found that by using the configuration of FTO/SnO_2(90 nm)/$MAPbI_3$/CuSCN (100 nm)/Au can yield a PCE of 26.74% and V_{oc} of 1180mV and FTO/SnO_2 (90 nm)/$MAPbI_3$/Spiro-OMeTAD (100 nm)/Au., The role of metal cathode work function was also studied to replace the expensive gold (Au) electrode.

Keywords: perovskite; solar cells; selective charge contacts; hole-transporting materials; Electron transporting materials.

1 Introduction

Organic-inorganic halide perovskites have received significant attention due to their extraordinary and tunable electro-optical properties, leading to improve performance in solar cells and light-emitting devices. These materials are well known for over a decade; however, Miyasaka et al. in 2009, mentioned its first usage in solar cells[9], which was built on D. Mitzi's work.

These materials can be represented by a general formula ABX_3, where A is an organic methylammonium ($CH_3NH_3^+$) ion [110] or formamidinium ($NH{=}CHNH_3^+$) ion [111–113]B is inorganic cation Pb^{2+}, Sn^{2+}, and X can be a halogen ion, I^-, Br^-, or Cl^-.

The remarkable performance of three-dimensional ABX_3 perovskites in solar cells was due to their panchromatic light absorption throughout the visible and near-infrared spectrum, the low exciton binding energy (~2 meV), direct band gap, [114] long diffusion length, high charge carrier mobility, which makes them ideal photovoltaic materials with controlling the quality of perovskite film by different methods can decrease the defect density to improve the photovoltaic parameters [115,116] . Owing to these unique characteristics, a certified power conversion efficiency (PCE) of 25.2 % was reported [5]. The PSCs work on the same photovoltaic operation principle, like solid-state dye-sensitized solar cells. Among the best efficiencies in PSCs showed until now are based on TiO_2 as ETL. However, TiO_2 needs to be annealed at high temperature (500 ^oC) to acquire the crystalline rutile phase [117–119], which inhibits the application of PSCs in flexible devices. Moreover, TiO_2 has low electron mobility [120] and is UV un-stable [121]. To avoid these drawbacks, Liu et al. used a low-temperature solution-processed based ZnO as ETL, and they measured a PCE of 15.7 % in planar PSCs [122]. These results showed new directions to replace TiO_2 by other metal oxides as ETL for high-efficiency PSCs. In 2015, Ke et al. demonstrated a PCE of 16.02 %, when low temperature solution-processed SnO_2 layer was used as an ETL in a normal planar structured PSCs with less hysteresis [123]. In another report, SnO_2 has been used as an efficient ETL in planar PSCs synthesized using low temperature ALD method, yielding a PCE of 18% along with no hysteresis [124]. The recent results using SnO_2 as an ETL in PSCs showed a high performance similarly as of TiO_2 and ZnO in planar architecture, with V_{oc} of 1090 mV and PCE of 20.3% [125] and also SnO_2 have got more attention due to its electronic structure [126]. However, these promising PSCs still suffer from the use of small organic molecule-based Spiro-OMeTAD as HTL. To work as an efficient HTL, this Spiro-OMeTAD needs dopant and additives such as hygroscopic LiTFSI salt and t-BP, which makes the perovskite solar cells unstable [41]. Besides, degradation of perovskite in the presence of doped Spiro-OMeTAD, the other reasons include 33.9% of the total device cost occurs due to the HTL synthesizing steps along with expensive gold (Au) working as a cathode in devices. [127]. To replace Spiro-OMeTAD, several other organic small molecules, polymers, inorganic p-type semiconductors, and organometallic complexes have been employed as HTL in PSCs and exhibited significant PV performance; however, in terms of atmospheric stability, few of them were found to be encouraging [128–132]. Recently, Cu-Based ternary chalcogenide semiconductors described by a general formula CuaBXb(B=Sn, Sb, Bi and X=Se, Te, S) are showing more attention as new HTLs in thin-film solar cells [133], such as CuSbS2 is from the family of abundant and cheap sulfates in nature [134] also another material, Cu2O demonstrated that could be a promising HTLs in PSCs to enhance its efficiency and the most important its low cost and it can help to create an environmentally friendly solar cell [135], CuI and CuSCN [136,137]. These inorganic HTLs have high conductivity and high carrier mobility compares to organic HTLs and can be used without doping but are still need more investigation with the best selective layer for efficient PSCs.

To address these challenges which have hindered the commercialization of PSCs, in the present work, we have used a simulation program named (Solar cell capacitance simulator) SCAPS for the screening of the HTLs, which can be tested experimentally in optimized condition. The main goal of this study is to propose efficient PSCs, using low-temperature processed ETL (SnO_2) with other alternative efficient HTLs.

Herein, firstly, ETL will be optimized. For the second step through a comparative study of three devices using TiO_2, ZnO, and SnO_2 as ETLs, $MAPbI_3$ as a light harvester and Spiro-OMeTAD as HTL with the gold (Au) and FTO as back and front contact respectively is performed. To the best of our knowledge in the case of simulation of perovskite solar cells, we investigated the first time the impact of the thickness of ETL on fill factor as a function of donor concentration (N_D). Through the screening of ETL from the first step, the second step will be focused on finding the efficient HTL using the configuration: FTO/SnO_2/$CH_3NH_3PbI_3$/HTL/Au and different HTL such as Spiro-OMeTAD poly(3-hexylthiophene-2,5-diyl) (P3HT), Copper antimony sulfide ($CuSbS_2$), Cuprous oxide (Cu_2O) and Copper thiocyanate (CuSCN) will be evaluated. The effect of different back contact on the device performance was also studied using SnO_2 as an ETL and CuSCN as HTL.

2 Device Simulation

The 1-dimensional Solar cell capacitance simulator (SCAPS) version. 3.3.07 was used as a simulation platform (ELIS, University of Gent, Belgium). It is based on three coupled differential equations, namely, Poisson's (39) and continuity equations for holes (40) and electrons (41) as follows:

$$\frac{d}{dx}\left(\varepsilon(x)\frac{d\Psi}{dx}\right) = q[\,p(x) - n(x) + N_D^+(x) - N_A^-(x) + p_t(x) - n_t(x)\,] \quad (39)$$

$$\frac{1}{j}\frac{dJ_p}{dx} + R_p(x) - G(x) = 0 \quad (40)$$

$$-\frac{1}{j}\frac{dJ_n}{dx} + R_n(x) - G(x) = 0 \quad (41)$$

Here, ε is the permittivity, q is the charge of electron, Ψ is the electrostatic potential and n is electron concentration, p is free hole concentration, n_t is trapped electron, p_t is trapped hole, N_D^+ is the ionized donor-like doping and N_A^- is the ionized acceptor-like doping concentrations, $R_n(x)$, $R_p(x)$ are electrons and holes recombination rate, G(x) is the generation rate, J_n and J_p are the electron and hole current densities respectively.

The planar structure used in this simulation, where the n-type transparent semiconducting metal oxide was modelled by investigating ETL such as TiO_2, ZnO and SnO_2, $CH_3NH_3PbI_3$ used as a light harvester, and Spiro-OMeTAD as HTL as illustrated in Figure *40*-a . The second part of this simulation was modeled by the SnO_2 as ETL with $CH_3NH_3PbI_3$ as an absorber layer, using P3HT, $CuSbS_2$, Cu_2O, CuSCN, and Spiro-OMeTAD as HTLs as shown in Figure *40*-b. Moreover, the gold (Au) is used as the back contact and fluorine doped tin oxide (FTO) as the front contact.

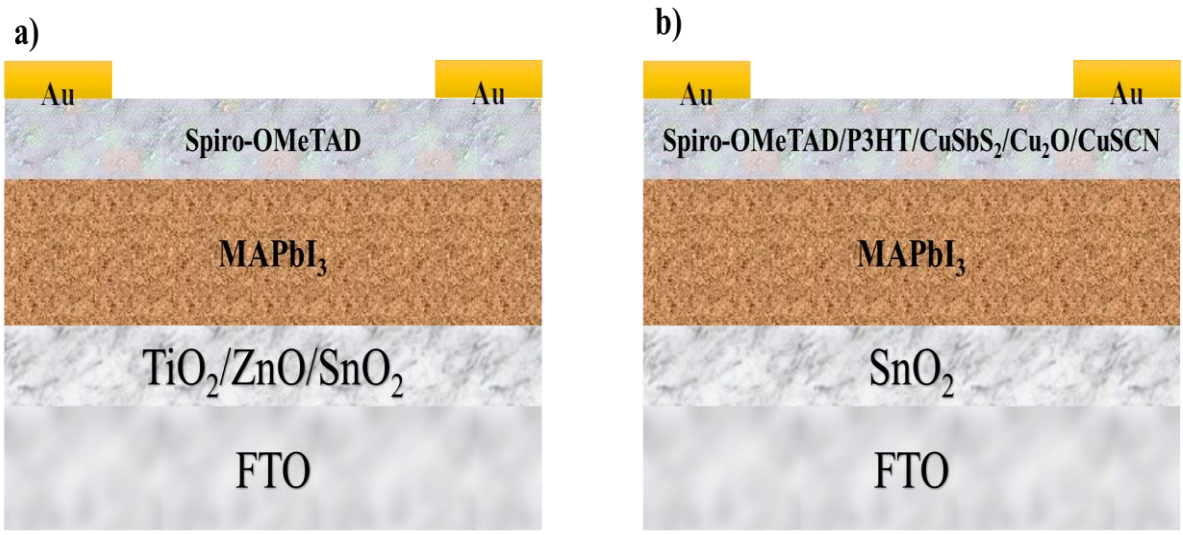

Figure 40:a-b) device structure of simulated perovskite solar cell

The input parameters used in SCAPS-1D for the simulation that are extracted from theories and literature are summarized in Table 3.[138,139,148–150,140–147].

In the device simulation, ETL/$MAPbI_3$, and $MAPbI_3$/HTL interface defect layer (IDL) is also introduced. The work function of HTL layers is calculated with respect to the valence band energy level [139], and input parameters are given in Table 2. Simulated current density-voltage (J-V) curve under illumination was obtained using standard AM 1.5G solar spectrum.

Where $\mathcal{E}_r$ is dielectric constant, E_g is bandgap, χ is electron affinity, N_c is effective conduction band density, N_v is effective valence band density, μ_n is electron mobility, and μ_p is hole mobility, N_D is donor concentration while N_A is acceptor concentration,

Table 3:Simulation parameters of the perovskite solar cell

Parameter	**$MAPbI_3$**	**n-TiO_2**	**n-SnO_2**	**n-ZnO**	**Spiro-OMeTAD**	**P3HT**	**$CuSbS_2$**	**Cu_2O**	**CuSCN**
thickness (nm)	450	Wide-ranging	Wide-ranging	Wide-ranging	Wide-ranging	Wide-ranging	Wide-ranging	Wide-ranging	Wide-ranging
E_g (eV)	1.5	3.2	3.6	3.3	2.9	1.7	1.58	2.17	3.6
χ(ev)	3.93	4	4	4	2.2	3.5	4.2	3.2	1.7
Ɛr	30	100	9	9	3	3	14.6	7.1	10
N_c (1/cm^3)	2.5×10^{20}	1×10^{21}	2.2×10^{18}	3.7×10^{18}	2.5×10^{20}	2×10^{21}	2×10^{18}	2.5×10^{18}	2.2×10^{19}
N_v (1/cm^3)	2.5×10^{20}	2×10^{20}	1.8×10^{19}	1.8×10^{19}	2.5×10^{20}	2×10^{21}	1×10^{19}	1.8×10^{19}	1.8×10^{18}
μ_n(cm^2/Vs)	50	0.006	100	100	0.0021	0.0018	49	200	100
μ_p(cm^2/Vs)	50	0.006	0.256	25	0.0026	0.0186	49	8600	25

N_A (1/cm^3)	--	-	-	-	1×10^{18}	1×10^{18}	1×10^{18}	1×10^{18}	1×10^{18}
N_D (1/cm^3)	--	5.06×10^{19}	1×10^{17}	1×10^{18}	-	-	-	_	-
Work function (eV)		---	---	---	-5	-5.1	-5.15	-5.27	-5.2

Table 4:Parameters of interfaces layer.

Interface	Defect type	Capture cross section electrons /holes (cm^2)	Energetic distribution	Reference for defect energy level E_t	Total density (integrated over all energies) (1/cm^2)	Total density (integrated over all energies) (1/cm^2)
ETL/$MAPbI_3$	Acceptor	1×10^{-17} 1×10^{-18}	Single	Above the VB maximum	0.32	1×10^{9}
$MAPbI_3$/HTL	Acceptor	1×10^{-18} 1×10^{-19}	Single	Above the VB maximum	0.07	1×10^{9} - 1×10^{12}

3 Results and discussion

3.1 Performance of PSCs based on Spiro-OMeTAD as HTL using different ETL

The role of ETL is to facilitate diffusion of the electrons from the photoexcited perovskite layer ($MAPbI_3$) into the FTO glass and thus to the external circuit. Materials have most used in the standard devices suffer from high-temperature processing, which has a deleterious effect on PSCs fabrication cost. To address such challenges, two categories of ETLs were compared in this work, one based on high processing temperature such as TiO_2, while the other was based on ZnO and SnO_2, which can be processed at low temperature. The photovoltaic parameters obtained from our simulation presented in Table 5.

Table 5:Performance of PSCs with 90 nm thick ETL layers.

Device Architect	J_{sc} (mA·cm^{-2})	V_{oc} (mV)	FF (%)	PCE (%)
FTO/ZnO/$MAPbI_3$/Spiro-OMeTAD/Au	25.10	1120	81.86	23.21
FTO/TiO_2/$MAPbI_3$/Spiro-OMeTAD/Au	24.98	1120	81.68	23.04
FTO/SnO_2/$MAPbI_3$/Spiro-OMeTAD/Au	25.59	1130	81.54	23.55

ETL thicknesses were kept the same in all three different types of solar cells investigated. From Table 5, it can be observed that for the same width of all the ETLs, the efficiency of PSC based on SnO_2 as ETL was higher than of ZnO and TiO_2. It can be deducted from Table 5 and J-V curve in Figure *41*, that the device based on SnO_2 as ETL showed higher current density than other ETLs employed here, due to increasing light absorption by the perovskite, which also reflects in the EQE increment in the 300-450 nm spectral region. SnO_2 has a wider band gap (3.6 eV) and higher transmittance in between 300-400 nm compared to that of ZnO(3.3eV) and TiO_2 (3.2eV)[123,151–155] These results suggest that low temperature processed SnO_2 as ETL in PSCs can be an effective candidate for efficient device fabrication. Our results are in accordance with the other reported experimental studies and numerical simulations[156–159].

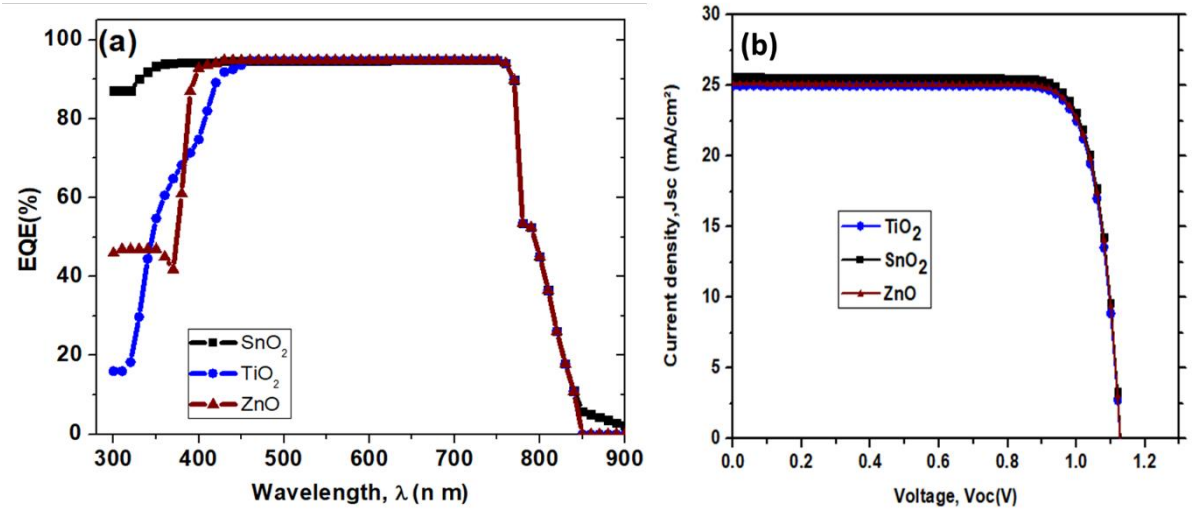

Figure 41: a) Simulated EQE curves and b) J-V curves of perovskite solar cells with 90 nm thick ZnO, TiO2, and SnO2 ETL layer.

3.2 Effect of ETLs Thickness on photovoltaic parameters

Figure 42 shows the variation of PV parameters open-circuit voltage (V_{oc}), short circuit current density (J_{sc}), fill factor (*FF*), and PCE as a function of ETLs layer thickness. All the devices were simulated using $MAPbI_3$ (450 nm) as light harvester and Spiro-OMeTAD (400 nm) as an HTL layer. The thickness of the ETL layer used here was varied from 90 nm to 200 nm. It can be noted that the increase of thickness leads to a decrease in V_{oc}, *Jsc*, and consequently PCE in the case of TiO_2 and ZnO, while in the case of SnO_2, these values did not change significantly. It is noticeable that the increase of ETL thickness harms V_{oc} and J_{sc} due to partial absorption of incident light by the thick ETL layer and change in series resistance. On the other hand, the decreased amount of light transmitted to the active layer with thicker ETLs leads to increase the fill factor up to a certain thickness (~150 nm), which might be due to less number of photon absorption by the active layer and thus decrease the rate of charge generation and collection and consequently short circuit current (J_{sc}), and series resistance will be reduced [156,160].

A simple empirical expression for the effect of the series resistance on fill factor [161]

$$FF_0 = FF_s(1 - rs) \quad (42)$$

FF_0 is the ideal FF in the absence of series resistance, r_s is the normalized series resistance, which equals $R_s * I_{sc}/V_{oc}$.

Using the above formula, the FF increased up to 150 nm thickness as a result of decrease series resistance due to the low charge generation rate.

We should mention here that we used high donor dopant concentration (N_D) for ETLs and, as mentioned in few works [160,162], the high value of donor dopant concentration (N_D) for ETLs leads to increase the conductivity of ETLs and reduces the resistivity. A similar observation was seen in organic solar cells that FF increases with high N_D and vice versa [163]. Here we investigated the effect of ETLs such as SnO_2, ZnO, TiO_2 thickness on the fill factor as a function of N_D. For a deep understanding of our results, the variation of N_D adapted to that used in the simulation for each layer. We figured out that with low N_D, the fill factor becomes very sensitive to thicker thickness with low

N_D if we increased the width of ETLs; the fill factor drops inversely to high N_D, as shown in Figure *43. b-c-d*, due to improvement in the conductivity of ETLs, as mentioned above.

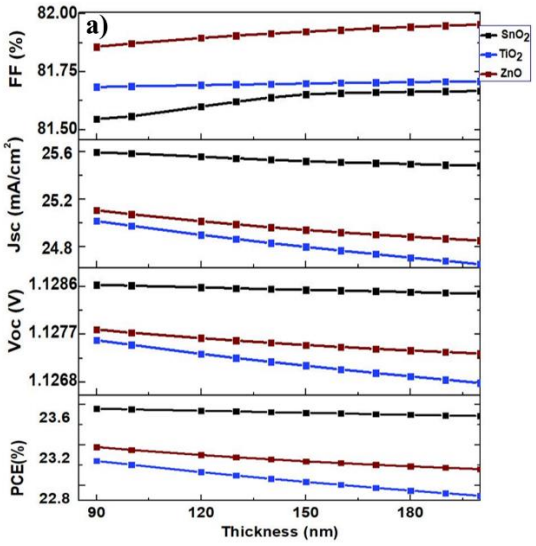

Figure 42: Effect of different ETL thickness on photovoltaic parameters.

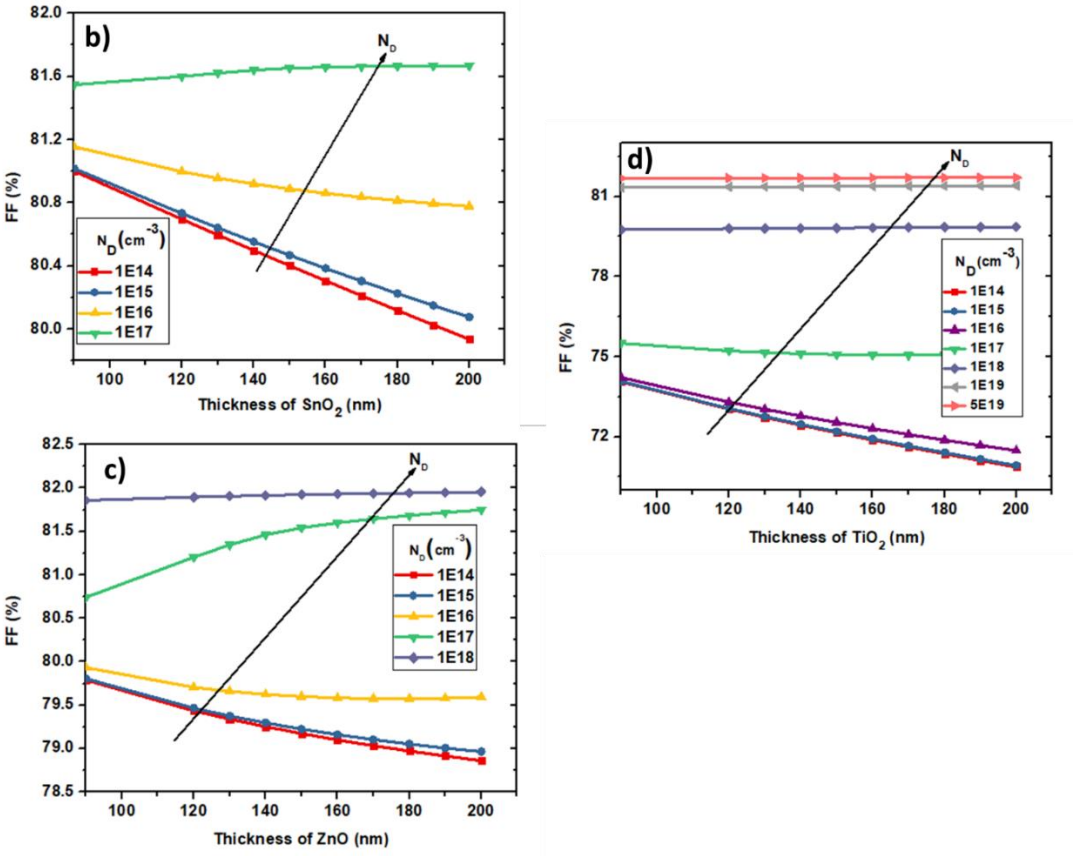

Figure 43: The effect of ETLs thickness b) SnO_2, c) ZnO, and d)TiO_2 on the fill factor as a function of dopant donor concentration(N_D).

4 Solar cell performance with SnO_2 ETL and using different HTLs

4.1 Photovoltaic parameters

Figure *44* shows the energy level diagrams of planar perovskite solar cells using SnO_2 as ETL and different inorganic and organic HTL, which affect the valence band offset (e.i the difference between the valence band of the absorber layer and those of HTL. The energy level alignment plays a vital role in the excellent performance of the solar cells. The photogenerated electrons in the perovskite are injected to the SnO_2 conduction band and hole to the HTL, and lastly, these extracted electrons and holes are collected to their respective front (FTO) and back contact(Au metal) respectively. To extract the electron at SnO_2/$MAPbI_3$ interface, the electron affinity (E.A.) of SnO_2 should be higher than the perovskite and to remove the holes at HTL/ $MAPbI_3$ interface, the ionization energy(I.E.) of HTL should be lower than perovskite. The energy level mismatching at ETL/perovskite and perovskite/HTL influence the PV properties, more importantly, open-circuit voltage(V_{oc}) and short circuit current(J_{sc}).

Figure *45*-b illustrates the simulated *J-V* curves of PSCs based on $MAPbI_3$ as perovskite (thickness 450 nm), SnO_2 as ETL (thickness is 90 nm) with P3HT, $CuSbS_2$, Cu_2O, CuSCN, and Spiro-OMeTAD as HTLs. It is noticeable that the devices fabricated with CuSCN as HTL outperformed with a V_{oc} of 1190 mV, J_{sc} of 25.60 mA/cm^{2,} and FF of 87.85% and an overall PCE of 26.74% can be achieved. This was followed by Cu_2O, which showed high performance after CuSCN with PCE of 25.97%, J_{sc} of 25.61 mA/cm^2, V_{oc} of 1150 mV, and FF of 88.39%. Cu_2O, P3HT also gave promising results achieving PCE of 20.8% with V_{oc} of 1140mV, J_{sc} of 25.55 mA/cm^{2,} and FF of 77.88%. The relatively low PV performance was found when $CuSbS_2$ was used as HTL, and it gave a PCE of 19.88%, V_{oc} 960mV, J_{sc} of 25.59 mA/cm^2 , and FF of 77.88%. The values of the energy levels of all layers used in the simulation with SnO_2 as ETL are illustrated in Figure *44*-a.

Among all the HTLs simulated here, the highest photovoltaic performance was found with CuSCN, followed by Cu_2O as HTLs in PSCs using SnO_2 as ETL. These two good performings HTLs have deeper valence band energy level concerning $MAPbI_3$ perovskite absorber compared with other HTLs, which allowed to maximize the V_{oc}, and sizeable optical band gap (Eg=3.6eV) of CuSCN guarantees good electron blocking properties of this HTL to prevent photogenerated electrons transfer from perovskite to itself. Further, it´s optical transparency in the UV-visible region allow to increase the absorption in the absorbing layer and thus enhanced the short circuit current [128,129,164]

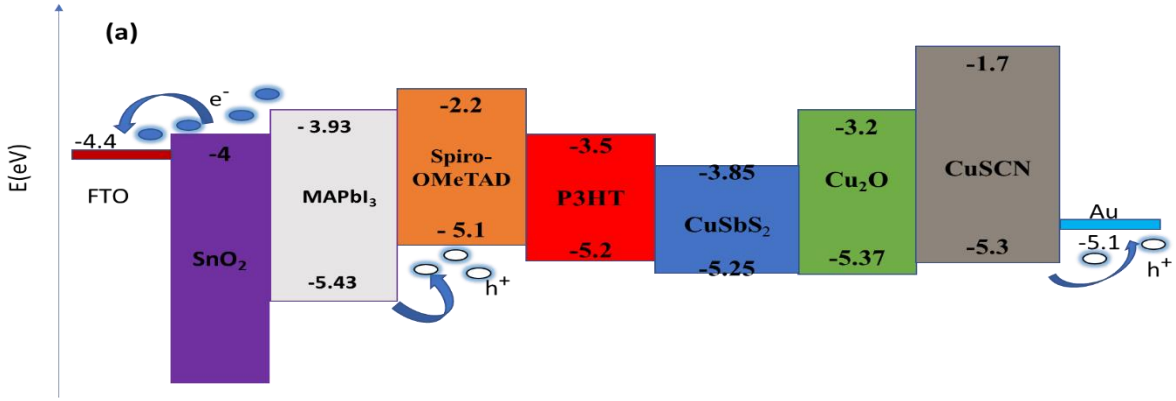

Figure 44: a)Corresponding band energy diagrams of planar perovskite solar cells using SnO2 as ETL and different HTL

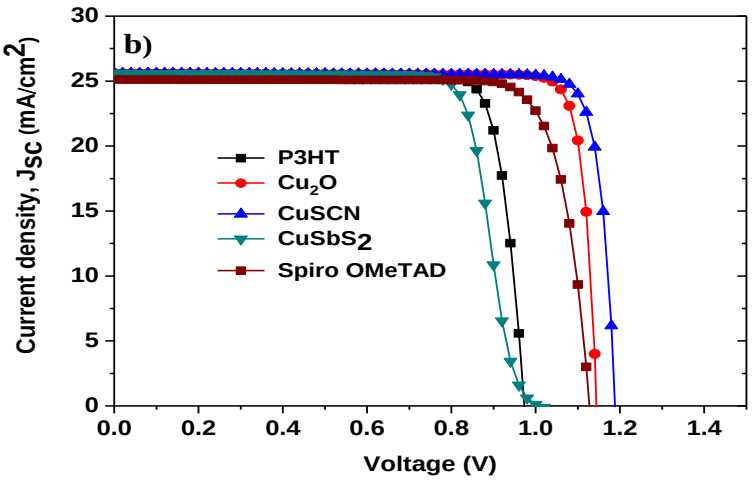

Figure 45: b) Simulated J-V curves of perovskite solar cells using SnO2 as ETL and P3HT, CuSbS2, Cu2O, CuSCN, and Spiro-OMeTAD as different HTL.

4.2 Effect of HTLs thickness on photovoltaic parameters

Figure 46 depicts the influence of HTLs thickness in the range of 20-200 nm on photovoltaic parameters with various HTLs, Spiro-OMeTAD, P3HT, $CuSbS_2$, Cu_2O, and CuSCN with SnO_2 and $MAPbI_3$ as ETL and absorber layer respectively. These results suggest that PV parameters depend on the type and thickness of HTL. The optimization of HTL thickness is mandatory to improve the PV performance, and the HTL layer act as a capping layer and prevents direct contact between the perovskite and gold metal.

It can be observed from *Figure 46* a-e, if the thickness exceeds 100 nm, the PCE decreases (in case of Spiro-OMeTAD and P3HT) or showed minor changes in the case of $CuSbS_2$, Cu_2O, and CuSCN. For the same thickness, V_{oc} increased in the case of Spiro-OMeTAD, Cu_2O, and CuSCN and showed low V_{oc} with the rest of HTLs ($CuSbS_2$, P3HT). The *FF* increases dramatically (Spiro-OMeTAD, P3HT, and $CuSbS_2$) or with negligible value; finally, J_{sc} showed a tiny increment (in case of Cu_2O) or a decrease in other HTLs. We can address here in case of the P3HT and Spiro-OMeTAD that has low carrier mobility, so it may be that the increase of the thickness while affecting the movement of free charges to stay for a longer time in the layer and hence they can recombine with oppositely charged Particles through the interface with the absorber layer, inversely with Cu-based HTL which had high mobility.

The P3HT and Spiro-OMeTAD have low conductivity and low charge carrier mobilities compared to the inorganic HTLs. Thus increased thickness in the case of organic HTLs will increase the resistance of the layer, and consequently, it will decrease the fill factor (FF) and device performance. While in the case of inorganic HTLS, due to their high mobility and high conductivity, they don't affect by the thickness.

Taiho Park et co-works [165] showed in their experimental work fascinating finding, for optimization of HTL, they addressed that a thicker HTL with high mobility may provide the high performance and reproducible devices.

Table 6 shows that all the devices performed excellently when the thickness was 100 nm, contrary to literature value, where 400 nm was simulated.

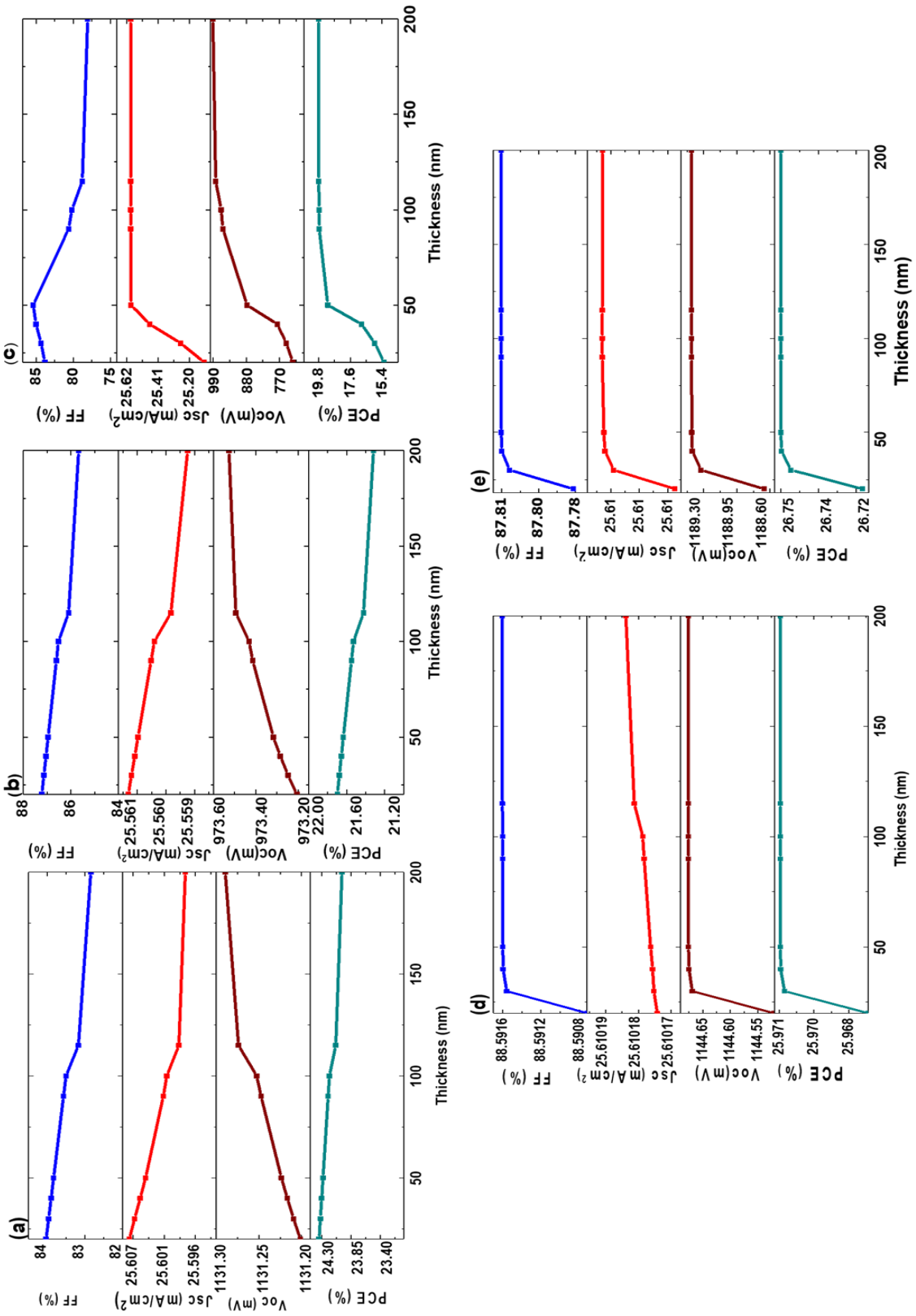

Figure 46: Effect of HTL thickness on photovoltaic parameters in the n-i-p configuration using SnO2 (90nm) as ETL in MAPbI3 based perovskite solar cells; a) Spiro-OMeTAD, b) P3HT, c) CuSbS2, d) Cu2O and e) CuSCN

Table 6: Performance of SnO_2~PSC with different HTL with optimum thickness.

Device Architect	HTL thickness (nm)	PCE (%)	V_{oc} (mV)	J_{sc} (mA/cm^2)	FF (%)
FTO/SnO_2/$MAPbI_3$/Spiro-OMeTAD/Au	100	24.18	1130	25.60	83.50
FTO/SnO_2/$MAPbI_3$/P3HT/Au	100	21.52	970	25.56	86.52
FTO/SnO_2/$MAPbI_3$/$CuSbS_2$/Au	100	19.70	960	25.59	80.18
FTO/SnO_2/$MAPbI_3$/Cu_2O/Au	100	25.97	1140	25.61	88.59
FTO/SnO_2/$MAPbI_3$/CuSCN/Au	100	26.74	1190	25.61	87.81

4.3 Impact of the work function of back contact on the PCE of SnO_2~PSCs with CuSCN as HTL

To further optimizing each stacking in PSCs, we have simulated the PSCs with different back contact in the device configuration of FTO/SnO_2/$MAPbI_3$/CuSCN/back contact (adaptable), to ratify whether another alternate back-contact (cathode) with similar performance as of Au can be used. Figure *47* showed the PCE of our simulated solar cell containing different back contacts such as Ag (4.74eV), Fe (4.81eV), C (5eV), Au (5.1), Ni (5.5eV), and Pt (5.70eV). The PCE of PSCs first increases with increasing the work function of metals up to a specific value of ~ 5.2-eV when the improvement become weak and then, it saturated totally at 5.4 eV that may be related to the work function of CuSCN (-5.2 eV) when we observed the start of saturation in the efficiency; due to the alignment with the WF of HTL and the valence band of the absorber layer. With high metal work function, the fermi level energy decreases due to band bending at the metal-semiconductor interface, leading the contact more ohmic[141]. From these values of metal work function, Figure *48* illustrated in for different back contacts, we can confirm that the carbon with work function at 5 eV can be used as a useful alternative for replacing the expensive Au electrode, and an efficiency of 25.55 %, can be achieved using the structure FTO/SnO_2/$MAPbI_3$/CuSCN/C for low-cost PSCs.

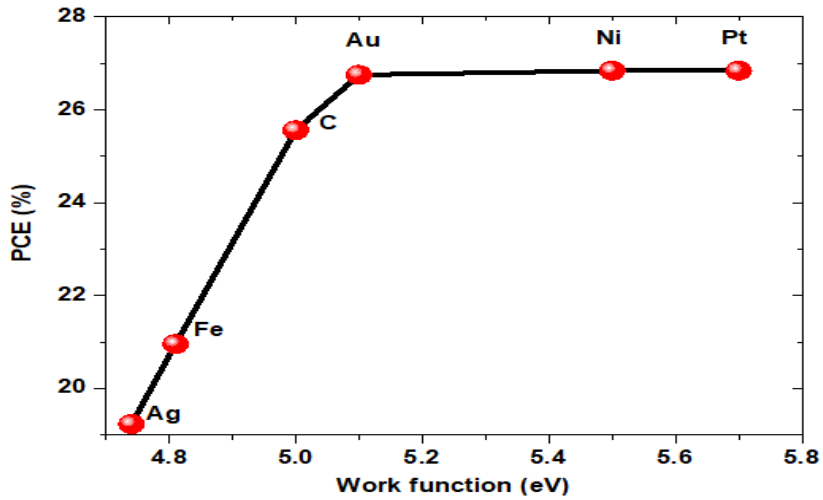

Figure 47:Effect of the work function of different back contact (metal contact) on the power conversion efficiency of planar perovskite solar cells, $MAPbI_3$ as perovskite absorber, SnO_2 as ETL and CuSCN as HTL.

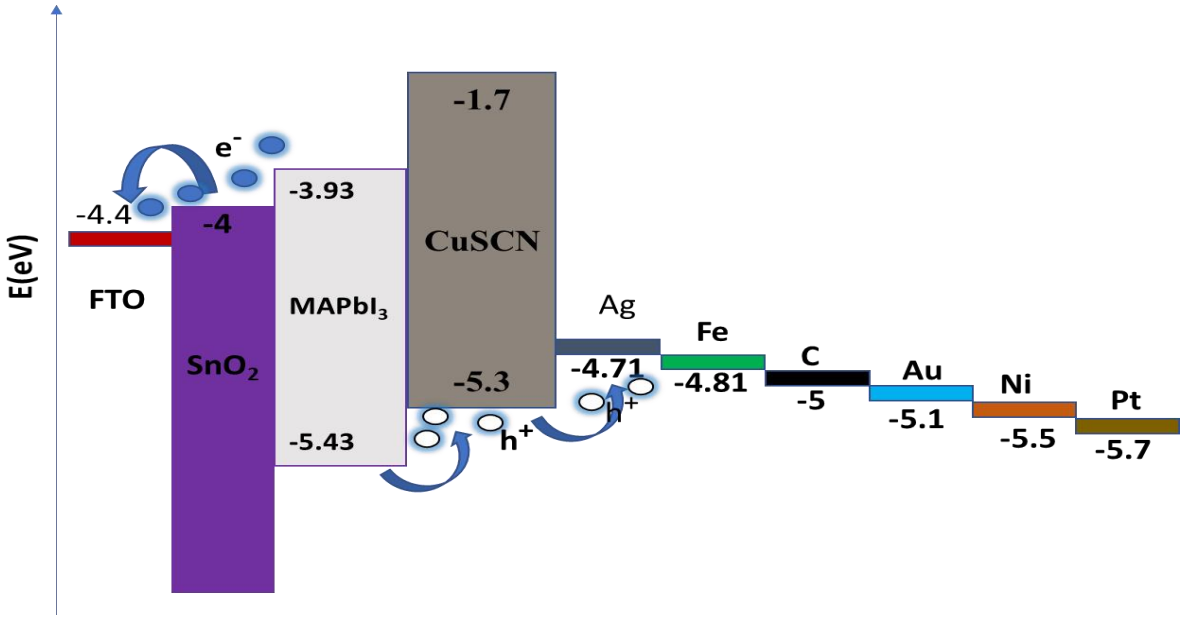

Figure 48:Energy levels for different back contacts with SnO_2 , $MAPbI_3$, and CuSCN.

5 CONCLUSION

To summarize, the performance of planar PSC with SnO_2 as ETL was studied, and a comparative study was made using other conventional ETLs and HTLs through a numeral simulation by SCAPS package for the first time. These results illustrated that the application of SnO_2 as an alternative ETL holds great promise in terms of PV performance as compared with TiO_2 and ZnO in the device architecture FTO/ETL/$MAPbI_3$/Spiro-OMeTAD/Au, and PCE of 23.21 %, 23.04 %, and 23.55% can be simulated using ZnO, TiO_2 and SnO_2 respectively. Additionally, the effect of various organic and inorganic HTLs such as P3HT, $CuSbS_2$, Cu_2O and CuSCN on the PV parameters was also studied, and it was found that the PCE improved from 23.55% to 26.74 % and V_{oc} from 1130 mV to 1180 mV, when Spiro-OMeTAD was substituted by CuSCN as HTL. In order to reduce the cost of fabricated PSCs, the effect of ETL and HTL thickness was simulated, which suggest that by employing low thickness in the range of 30 -100 nm of HTLs can produce similar or high performance compared with 400 nm reported in the literature. Further, using the carbon as back contact can allow achieving a PCE of 25.25 %, which is a model material to replace the expensive gold electrode (Au). Our results will pave the way for optimizing the PSCs' cost and performance.

Chapter 5: Energy level engineering of charge selective contact and halide perovskite by modulating band offset: Mechanistic insights

Abstract

Mixed cation and anion based perovskite solar cells $(FAPbI_3)_{0.85}(MAPbBr_3)_{0.15}$ gave enhanced stability under outdoor conditions. However, it yielded limited power conversion efficiency when SnO_2 and Spiro-OMeTAD were employed as electron and hole transport layers (ETL/HTL). The inevitable interfacial recombination of charge carriers at ETL/perovskite and perovskite/HTL interface diminished the efficiency in planar (n-i-p) perovskite solar cells. Employing a computational approach for uni-dimensional device simulator, the effect of band offset on charge recombination at both interfaces was investigated. We noted that it acquired cliff structure when the conduction band minimum of the ETL is lower than that of the perovskite, and thus maximizes interfacial recombination. However, if the conduction band minimum of ETL is higher than perovskite, i.e., spike structure is formed, which improve the performance of solar cell up to an optimum value of conduction band offset allowing to reach the performance of 25.21%, with an open-circuit voltage (V_{oc}) of 1231 mV, a current density J_{sc} of 24.57 mA/cm^2 and a fill factor of 83.28%. Additionally, we found that beyond the optimum offset value, a large spike structure could decrease the performance. With an optimized, energy level of Spiro-OMeTAD and the thickness of a mixed-perovskite layer performance of 26.56 % can be attained. Our results demonstrate a detailed understanding of the energy level tuning between the charge selective layers and perovskite and furthermore, how the improvement in PV performance can be achieved by adjusting the energy level offset.

Keywords: Device modeling, Electron Affinity, Conduction band offset, Valence band offset, Charge recombination, Perovskite solar cell.

1 Introduction

Over the past years, hybrid organic-inorganic lead halide perovskite was subject to intense investigation due to its astonishing opto-electrical properties, which led to the fabrication of efficient solar cells that are cost-effective and easy to process. One of the seminal scientific events of 2009 was the report of perovskite solar cells (PSCs) fabrication, which gave 3.8% power conversion efficiency (PCE) [9]. After a decade of highly intense efforts by researchers across the globe, PSCs have reached the certified PCE of 25.2% [166], while the theoretical approach for this has also been reported [167].

The rapid evolution in the field of PSCs was ensued due to the radical approach in materials compositions and device architect engineering. The first report employed it as a sensitizer in a solid-state dye-sensitized solar cell [168], followed by as an absorber in insulating alumina scaffold structure, and subsequently in a planar heterojunction PSC [169]. The planar heterojunction has attracted significant attention due to its ease of processing and the existing knowledge borrowed from organic photovoltaics. The PSCs based on *n-i-p* planar configuration consists of transparent conducting oxide (TCO) / electron transport layer (ETL) / perovskite / hole transport layer (HTL)/metal contact; where, ETL act as n-type, HTL as p-type and perovskite as intrinsic layer. In recent years, we have witnessed a surge of interest in utilizing SnO_2 as ETL for PSCs fabrication due to its numerous merits. Compared to conventional TiO_2, SnO_2 exhibits a wider band gap due to deeper conduction band, shows high transmittance over a wide spectral range with high electron mobility, which in turn can fasten electron transfer from perovskite to the ETL and minimize the charge accumulation at the ETL/perovskite interface. Moreover, SnO_2 is stable than TiO_2 under UV illumination and ideally suited with low-temperature fabrication process; all these properties make tin oxide as a favorable candidate as ETL for PSCs [117,128,131,170–173]. The best efficiency using SnO_2 as ETL was reported with different perovskites such as $MAPbI_3$, $(FAPbI_3)_{0.97}(MAPbBr_3)_{0.03,}$ and $(FAPbI_3)_{0.85}(MAPbBr_3)_{0.15}$ [154,174–177]. Among them, $(FAPbI_3)_{0.85}(MAPbBr_3)_{0.15}$ demonstrated higher stability under outdoor conditions as well as in the laboratory [18,19]. You's group reported 21.6% room-temperature processed SnO_2 and passivated $FAPbI_3$ [179], this improvement in PCE was made possible due to increased electron extraction as a result of optimized perovskite film fabrication process, to allow the carriers rational interface between the ETL/perovskite. The conduction band of SnO_2 depends on various factors, such as the method and fabrication condition, oxygen vacancies that directly affects the energy level alignment at ETL/perovskite. Among many factors that cause lower V_{oc} in PSCs, the interface recombination at ETL/PSK and PSK/HTL influence largely and affects device performance [180,181]. For planar PSCs, charge injection and recombination processes depend on the properties of ETL, HTL, energy level alignment for ETL/absorber and absorber/HTL interface, and defect density at both

interfaces. Thus, an optimized interface is vital to push the performance of PSCs, which can be achieved by adjusting the conduction band offset (CBO) and valence band offset (VBO). These band offsets are critical for charge transport, extraction, and interface recombination in PSCs. Interface engineering at ETL/perovskite and perovskite/HTL interface play an important role in influencing the carrier recombination and profoundly, the performance of PSCs [16,129,182,183]. Takachi et al. have reported the effect of tunneling the electron affinity of ETL to form spike and cliff structures which have a bearing on the performance of PSCs, in *n-i-p* configuration employing classical TiO_2 as ETL, $MAPbI_{3-x}Cl_x$ as absorber layer with an electron affinity of 3.9 eV, and Spiro-OMeTAD as HTL. The reported parameters were limited, and with the compositional engineering of perovskite, the energy level will change, and importantly the ETL used to suffer from, lower electron mobility which causes insufficient charge carrier separation at the interface and hysteresis [184], the UV instability of TiO_2 yields to rapid decrease in the performance [185]. Earlier, we have shown that $(FAPbI_3)_{0.85}(MAPbBr_3)_{0.15}$ as light harvester in PSCs showed improved stability under outdoor conditions [41], and theoretically we analyzed the performance of PSCs using SnO_2 as an alternative of TiO_2 [167]. To overcome intriguing stability and performance issue we undertook mechanistic study in a configuration of FTO/SnO_2/$(FAPbI_3)_{0.85}MAPbBr_3)_{0.15}$/Spiro-OMeTAD/Au which can elucidate the role of spike and spoke with an electron affinity of 4.15 eV for perovskite layer. Doping of SnO_2 can shift the level energy by adjusting the alignment between the layers, also it can enhance the performance of the device by reducing the recombination rate at ETL/perovskite interface.

To address such challenges, herein, by using solar cell capacitance simulator (SCAPS) software, we have elucidated the impact of energy level alignment between ETL/absorber interface using SnO_2/$(FAPbI_3)_{0.85}(MAPbBr_3)_{0.15}$, and absorber/HTL interface using $(FAPbI_3)_{0.85}(MAPbBr_3)_{0.15}$/Spiro-OMeTAD by varying the conduction band offset (CBO=$\Delta Ec= Ec,_{ETL}- Ec,_{absorber}$) and valence band offset (VBO = $\Delta E_{V} = E_{V,absorber} - E_{V,HTL}$) respectively via the electron affinity of selective layers. We noted that changing the electron affinity of SnO_2 and Spiro-OMeTAD leads to a favorable CBO and VBO, respectively, and decreases charge recombination at both interfaces and improves the external quantum efficiency (EQE) in the spectral range of 320 − 360 nm. These factors help to enhance the performance of our modeled PSCs with optimized CBO (+0.35eV) and VBO (-0.41 eV), which can yield a PCE of 26.50 % with a V_{oc} of 1.23 V, J_{SC} of 24.88 mA/cm^2 and FF around 86.53 %.

1. Experimental Section

The normal glass and ITO coated glass substrates were cleaned by a sequential sonication treatment in hellmanex solution, acetone, distilled water, and isopropanol and then treated with UV-

ozone for 1h. For optical measurements, $(FAPbI_3)_{0.85}(MAPbBr_3)_{0.15}$ was deposited from a precursor solution containing FAI (1 M), PbI_2 (1.2 M), MABr (0.2 M), and $PbBr_2$ (0.2 M) in anhydrous DMF:DMSO 4:1 (v:v). The perovskite solution was spin-coated in a two-step process at 1000 and 4000 rpm for 10 and 30 s, respectively. During the second step, 100 µL of chlorobenzene was used as an antisolvent and poured on the substrate 15 s prior to the end of the deposition process. The substrates were then annealed at 100 °C for 1 h in a glovebox, according to the previous report [186]. The hole transporting layer (HTL) was prepared by dissolving 72.3 mg of Spiro-OMeTAD in chlorobenzene and mixed with 28.8 µL of 4-tert-butylpyridine, 17.5 µL of bis(trifluoromethane) sulfonamide lithium salt (Li-TFSI) from the stock solution(520 mg mL^{-1} in acetonitrile). The solution was spin-coated on normal glass at 4000 rpm for 20 s. The electron transporting layer (ETL): SnO_2 nanoparticles (2.67 %) solution was spin-coated on normal glass substrates in ambient air at 5000 r.p.m. for 30 s, and was subject to annealing at 150 ^oC for 30 min.

Device Preparation: The concentration and deposition conditions of the absorber and charge selective layers were the same as mentioned above. SnO_2 as ETL was deposited on the ITO substrate using SnO_2 nanoparticles (2.67 %) followed by thermal annealing at 150 ℃ for 30 min in air. Subsequently, perovskite deposited in a one-step deposition method [186]. Followed by the hole transporting layer Spiro-OMeTAD was deposited on top of perovskite at a spin rate of 4000 rpm for 20 s. Finally, a ~ 70 nm gold electrode was thermally evaporated on top of the HTL.

Absorption Measurements: The absorption spectra was required to make inputs for SCAPS simulation, and the thickness of different layers was determined from cross-sectional SEM image as illustrated in Figure *50.* For the device simulation, the absorption coefficient (α) of $(FAPbI_3)_{0.85}MAPbBr_3)_{0.15}$ (absorber layer) Spiro-OMeTAD (HTL) and SnO_2 (ETL) film was determined by measuring the absorbance spectra and b) and the thickness (L), using the equation $\alpha = A\ ln_{10}/L$[187]. The absorbance was measured using Cary 60 UV-vis spectrophotometer. The width of the film was determined by cross-section SEM as shown in Figure 50.

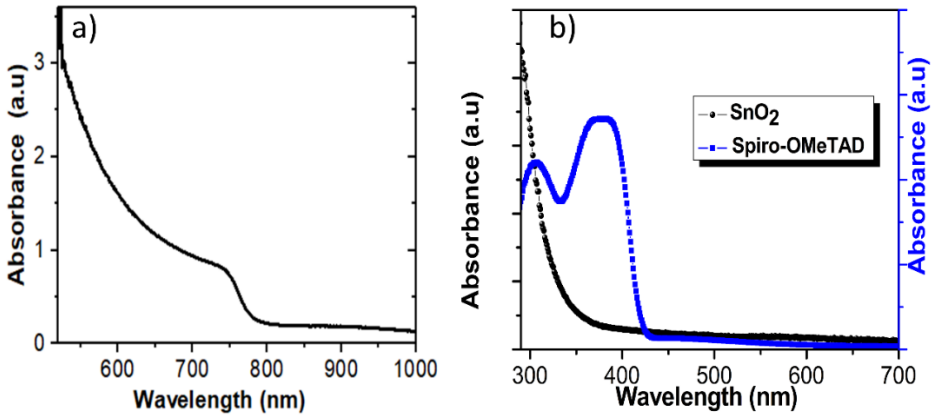

Figure 49: (a) UV-Vis absorption spectra of mixed perovskite $(FAPbI_3)_{0.85}(MAPbBr_3)_{0.15}$ and (b) Spiro-OMeTAD and SnO_2

2. Device simulation parameters

The simulations were performed using SCAPS 3.3.07 software [188], which is based on the Poisson equation (39), and the continuity equations for electrons (40) and holes (41), as reported in our previous work [167].

$$\frac{d}{dx}\left(\varepsilon(x)\frac{d\Psi}{dx}\right) = q[\,p(x) - n(x) + N_D^+(x) - N_A^-(x) + p_t(x) - n_t(x)\,] \quad (39)$$

$$\frac{1}{j}\frac{\mathrm{d}J_p}{\mathrm{d}x} + R_p(x) - G(x) = 0 \quad (40)$$

$$-\frac{1}{j}\frac{\mathrm{d}J_n}{\mathrm{d}x} + R_n(x) - G(x) = 0 \quad (41)$$

The device architecture of the planar *n-i-p* type PSCs proposed in the present simulation study consists of FTO/SnO_2/interface layer 1 (IL1) /$(FAPbI_3)_{0.85}MAPbBr_3)_{0.15}$ /interface layer2 (IL2)/ Spiro-OMeTAD /Au as illustrated in Figure *50*-b. The gold (Au) was back contact (cathode) and fluorine doped tin oxide (FTO) as the front contact (anode). The thickness of the FTO, ETL, absorber, and HTL were calculated from the cross-sectional SEM image of fabricated device showing an experimentally achieved efficiency of 11.5 % with a V_{oc} of 0.97 V, J_{sc} of 19.27 mA/cm^2 and fill factor (FF) of 61.41%.

Table *7* summarizes the input parameters for the FTO, SnO_2, mixed perovskite, Spiro-OMeTAD, IL1 and IL2. In the table, NA and N_D denote acceptor and donor densities, ε_r is relative permittivity, χ is electron affinity, E_g is the band gap energy, μ_n and μ_p are mobilities of electron and hole, and N_t is defect density, which is the most critical parameter to calculate the efficiency of the PSCs. For mixed perovskite, $N_t = 3\times10^{11}$ cm^{-3} was taken from the literature. [178]. The defect type in bulk perovskite is considered to be neutral, and capture cross-section of electron and hole is 2×10^{-14} cm^2. The electron and hole thermal velocity was 10^7cm/s. The simulations were carried out at AM 1.5G illumination.

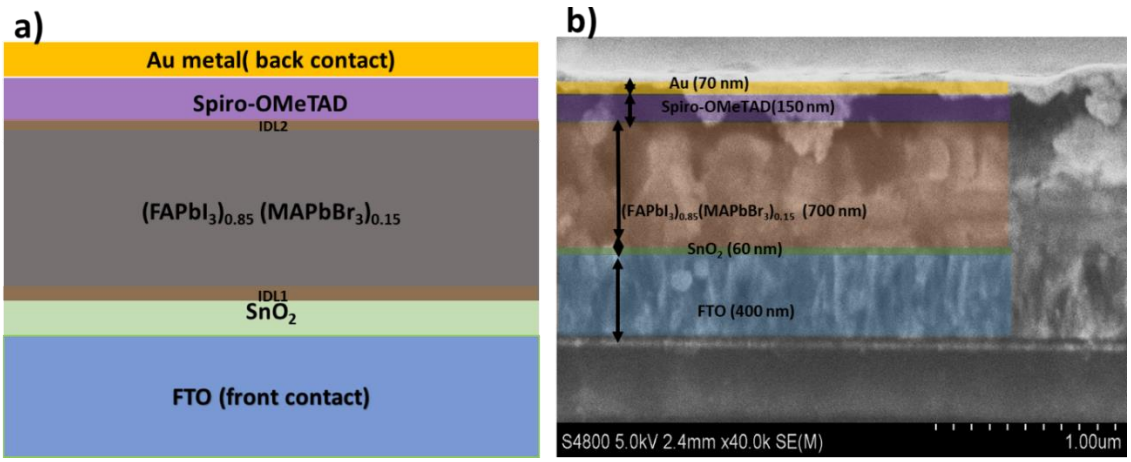

Figure 50:a) Device architecture of planar type perovskite solar cell used in the present study and b) cross-sectional SEM image.

Table 7: Parameters Used in the SCAPS Simulation of Perovskite solar cell.

Parameter	FTO	SnO_2	IL1	Mixed PSK	IL2	Spiro-OMeTAD
thickness (nm)	400	90	10	700	10	150
Band gap, E_g (eV)	3.5	3.6[189]	1.56	1.56[124,190]	1.56	3.04[191]
Electron affinity (χ)	4	Wide-ranging	4.15	4.15[124,190]	4.15	2.11[191]
Ɛr	30	100	46.9	46.9 [192]	46.9	3[191]
***Nc* (1/cm^3)**	2.2×10^{18}	2.2×10^{18}	2.2×10^{18}	2.2×10^{18}	2.2×10^{18}	2.2×10^{18}
***Nv* (1/cm^3)**	1.8×10^{19}	1.8×10^{19}	1.8×10^{19}	1.8×10^{19}	2.5×10^{19}	1.8×10^{19}
μ_n(cm^2/Vs)	20	240[193]	5.31	5.31[192]	5.31	0.001[194]
μ_p	10	240	10.19	10.19[192]	10.19	0.001
N_A (1/cm^3)	--	-	-	-	-	1×10^{18}
N_D (1/cm^3)	2×10^{19}	1×10^{17}	1×10^{13}	1×10^{13}	1×10^{13}	-
N_t(1/cm^3)	1×10^{15}	1×10^{15}	1×10^{15}	3×10^{11}[178]	1×10^{15}	1×10^{15}

2 Results and discussion

2.1 Formation of Cliff-CBO (-eV) and Spike-CBO (+eV) structures at ETL/perovskite layer

One of the hot debate in the community of PSCs, is the energy level between the perovskite layer and the selective layers; the topic is still far to make it clear. To figure out this issue, the efforts should focus on building a canal between the theoretical and experimental studies.

Here, through the theoretical device modeling, by adjusting the electron affinity (χ) of SnO_2 as ETL, we can notice the formation of two structure related to the conduction band offset (CBO) of $SnO_2/(FAPbI_3)_{0.85}MAPbBr_3)_{0.15}$ layer, when the electron affinity of ETL (χ_{ETL}) is larger or smaller than absorber layer($\chi_{absorber}$) as illustrated in Figure *51*, the energy Cliff with CBO (-) and the energy spike

− CBO (+) formed respectively. In other words, if the conduction band of ETL is lower than that of the absorber, the energy Cliff CBO (−) is formed with no potential barrier for electrons at the ETL/absorber interface. If CB of ETL is higher than that of the mixed perovskite absorber, the energy Spike-CBO (+) is formed at the ETL/absorber interface, acting as a barrier for electrons as shown in Figure 52.

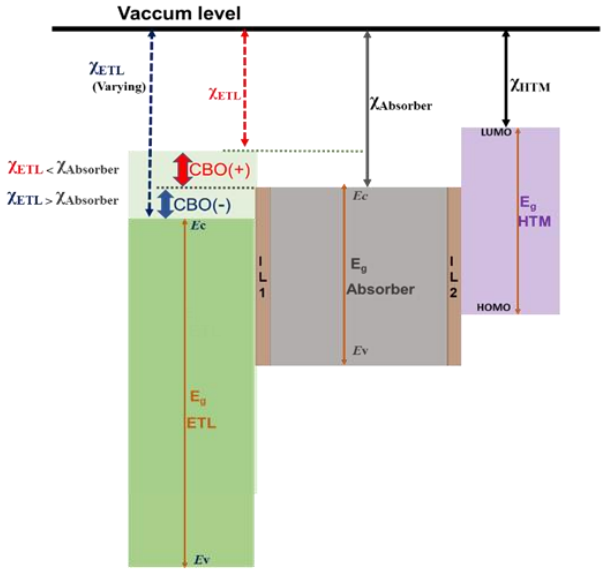

Figure 51: Band alignment scheme of SnO_2 ETL/IL1/mixed perovskite absorber showing negative and positive conduction band offset (CBO) by varying the electron affinity of SnO_2 with respect to mixed (FAPbI3)0.85(MAPbBr3)0.15. The negative and positive signs of the CBO were defined by the barrier height of the photo-generated electrons.

The cliff formation can improve the accumulation near to SnO_2/perovskite, which in turn enhances the recombination in this area by back-transfer to the interface of $SnO_2/(FAPbI_3)_{0.85}MAPbBr_3)_{0.15}$ heterojunction. On the other hand, the formation of spike structure act as band bending to reduce the recombination at $SnO_2/(FAPbI_3)_{0.85}MAPbBr_3)_{0.15}$. A similar trend has also been reported in perovskite solar cells and other types of thin-film solar cells [181,195–197].

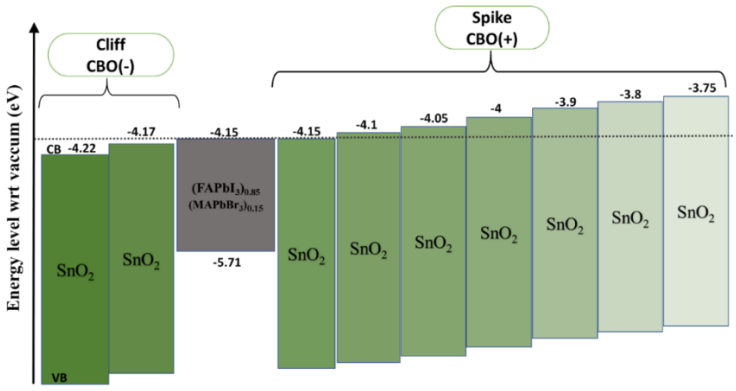

Figure 52: Theoretically calculated energy levels diagram (relative to the vacuum level) of SnO2 films by varying the electron affinity of SnO_2 with respect to mixed $(FAPbI3)_{0.85}(MAPbBr3)_{0.15}$.

2.2 Influence of the conduction band offset of ETL/perovskite interface on PV performance

Figure 53-a represents *J-V* characteristics as a function of conduction band offset ranging from -0.07 to +0.4 eV by controlling the electron affinity of SnO_2, and Figure 53-b shows the influence of the CBO on V_{oc}, J_{sc} and *FF* and PCE. With the increase in the CBO value, the cliff structure transforms into the spike structure (Figure 53 -d) . The J_{sc}, V_{oc}, FF, and PCE of PSCs first increase with increasing CBO until +0.35eV and then becomes constant. The solar cell with CBO_{spike}= +0.35eV showed the best performance, with an astonishing PCE of 25.61%, a V_{oc} of 1231 mV, a J_{sc} of 24.57 mA/cm^2 and a *FF* of 83.28 %.

To understand the enhancement in the performance by differentiating with cliff and spike structure, we first analyzed the external quantum efficiency (EQE) using the same variations of CBO as used for the *J-V* characteristics and illustrated in Figure 53-d, We can notice that increasing CBO lead to an increase in the EQE value in the spectral range of 300 − 360 nm, and when the CBO is higher than +0.35, the EQE becomes saturated in this region, this has a positive impact on the performance of the solar cell.

The decrease in the V_{oc} for the lower value of CBO can be assigned to the cliff structure formation, which is build up at ETL/mixed-perovskite, and leads to high recombination between the holes and electrons due to small potential difference at this area Figure 50-a. On the contrary, the formation of spike structure leads to build a barrier at ETL/mixed-perovskite to facilitate the separation of charge carriers Figure.50-b.

The effect of CBO on V_{oc} can be illustrated according to equation (4) [198,199].

$$Voc = \frac{E_A}{q} - \frac{nkT}{q} ln \frac{Joo}{Jsc} \qquad (43)$$

$$E_A = Eg - \Delta Ec \qquad (44)$$

V_{OC} is open-circuit voltage; E_A is the activation energy, n is diode ideality factor, K is Boltzmann constant , T is temperature, J_{00} is current pre factor and J_{sc} is short circuit current density. For T = 0 K, ($Voc = \frac{E_A}{q}$), as illustrated in Figure 53-a and Figure 54-a, the formation of “cliff-type” band alignment will break the barrier for the transfer of electrons, leading to decrease $E_{A,}$ and this directly affects the value of V_{oc}.

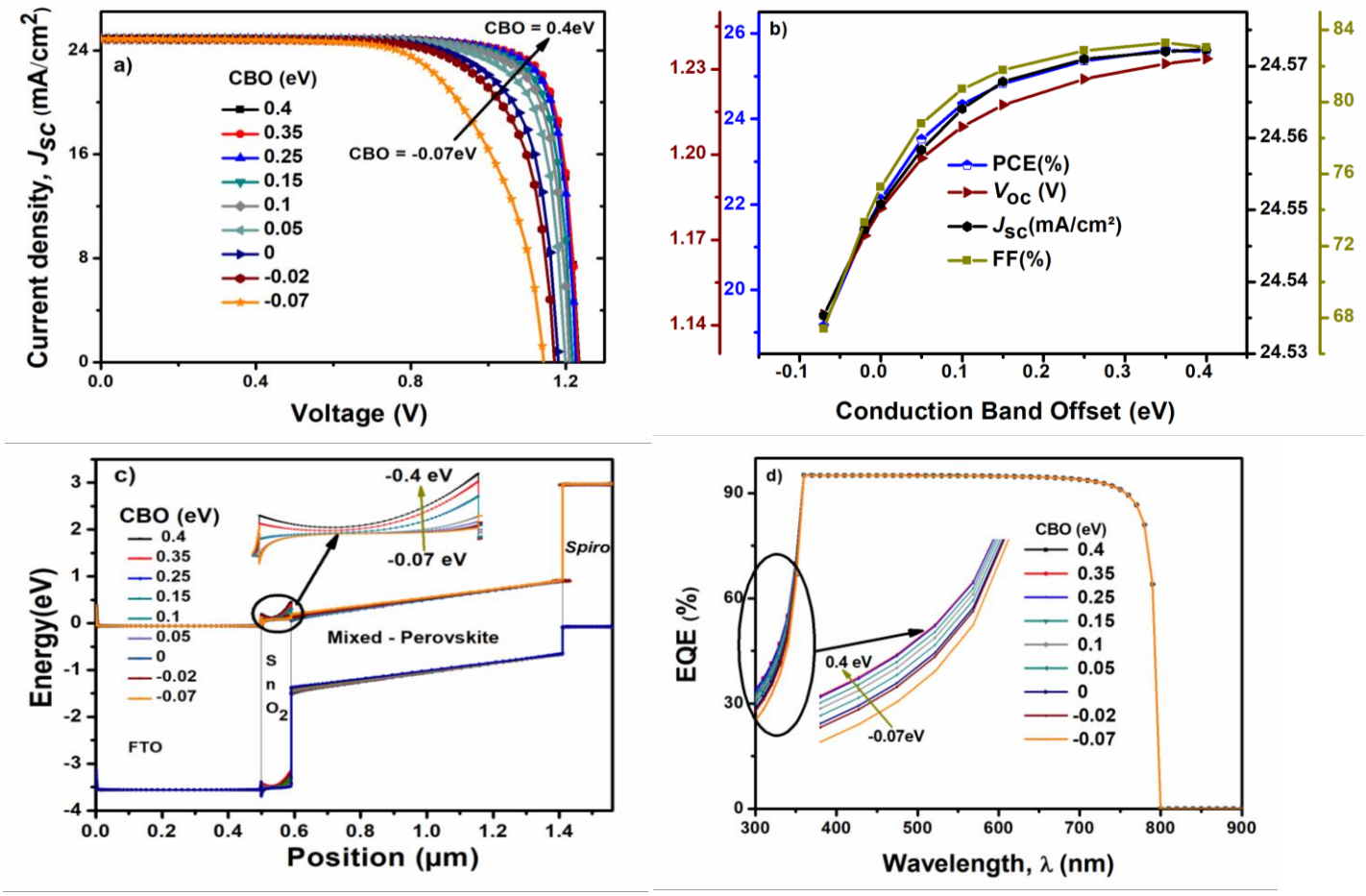

Figure 53: a) J–V curves of perovskite solar cell as a function of CBOs, b) Influence of the CBO on PCE, V_{oc}, J_{sc} and FF, c) Energy band diagram of planar perovskite solar cells with the variation of conduction band offset showing the formation of the cliff and spike structure and d) effect of conduction band offset on External Quantum efficiency.

We can analyze the advantage of spike structure when is formed at the ETL/absorber layer interface as shown in Figure *53,* and Figure *54* which can act as a barrier for photo-generated electron flow toward to edge of ETL/absorber endows to enhance the photo-generation of free charges carriers as well the suppressing the recombination rate at the interface which is helpful to increase the photovoltaic parameters of the solar cell, means that spike structure makes the extraction and transport of charges carriers efficient. To continue this improvement in the performance of solar cell using the spike structure at ETL/absorber, we highly recommended the optimizing of CBO value for do not becomes larger compared to the energy alignment of the absorber layer, to avoid that the spike structure will not work as a barrier to stop the migration of electron to the back contact which would lead to increase the rate of recombination at interface.

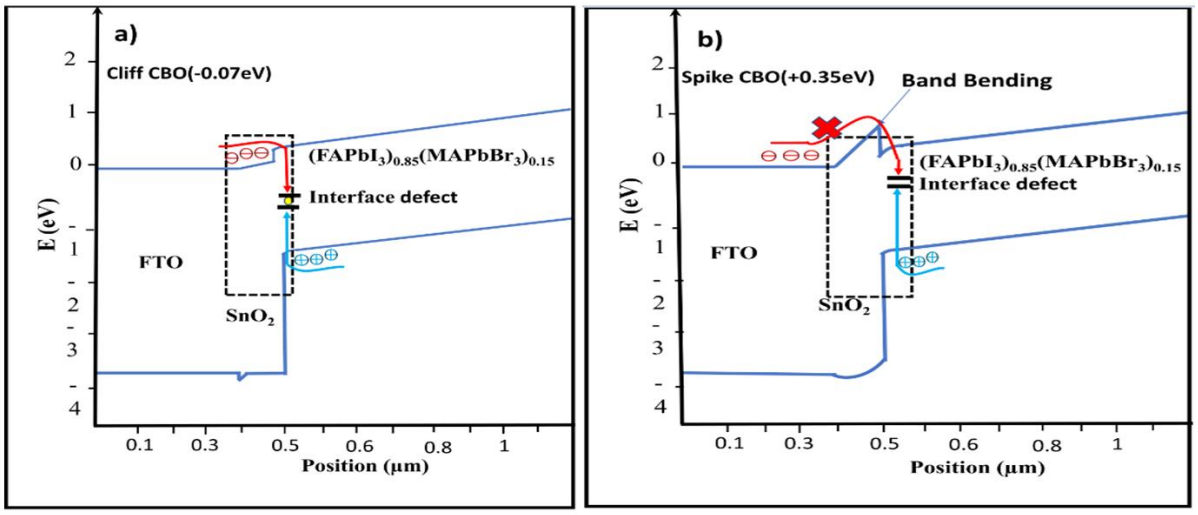

Figure 54: Energy band diagram of PSCs using the FTO/SnO_2/mixed PSK/Spiro-OMeTAD structure when the conduction band minimum of SnO_2 is a) below {cliff structure} and b) above {spike structure} that of CBM of mixed perovskite.

2.3 Influence of CBO of ETL /Perovskite on charge recombination

The recombination at the interfaces is multiple steps, where first the majority carrier extracted to the ELL, then recombination with the minority carrier generated in the perovskite layer, which means that should increase the lifetime of free charges by minimizing the capture of the hole by the electron.

The spike structure would act as a barrier to block the flow of injected electrons from the ETL to the absorber layer. The perovskite solar cells are facing many challenges; one of them is the recombination loss across the interfaces, especially at the ETL/absorber, which can lower the voltage as reported previously [16]. The issue of recombination at the interfaces come from the defect state and due to misalignment of the energy between the perovskite and the ETL [15]. To figure out the improvement in the performance of PSCs related to the CBO, we investigated the effect of CBO on the recombination rate at ETL/absorber.

Figure 55 depicts the total recombination rate of FTO/SnO_2/$(FAPbI_3)_{0.85}MAPbBr_3)_{0.15}$/Spiro-OMeTAD/Au with the variation of CBO. It can be noted that decreasing the CBO of ETL /perovskite helps to reduce the interface recombination between SnO_2 and mixed perovskite. This provides the solution to enhance the performance of solar cells with an optimum value of CBO of +0.35 eV. After achieving this optimum value of CBO, the interface recombination saturated. The formation of the cliff structure between ETL / perovskite facilitates the accumulation of electrons and holes, which contributes to the highest recombination rate. When the spike structure starts to form, the recombination rate decreases until an optimum spike is formed. Therefore, after reaching to the CBO value of +0.35 eV, the spike structure becomes a barrier that prevents the back transfer of electrons to the perovskite.

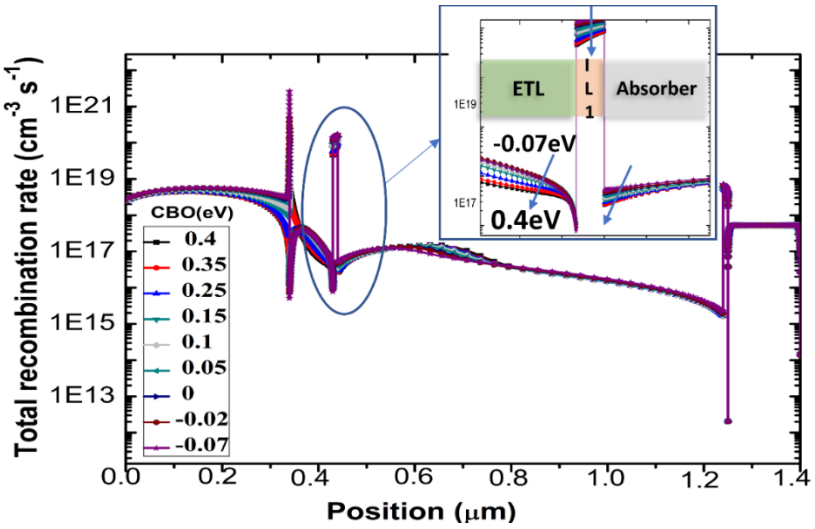

Figure 55: The depth distribution curve showing total recombination rates of the perovskite solar cells with different CBO at 0V bias.

The design of an optimum CBO can reduces the recombination rate and enhances the extraction of free charges at ETL/perovskite by forming an optimum spike structure at the interface leads to build a stronger band bending that prevents to flow of injected electrons to the interface which lowers the recombination rate between the majority and minority carriers.

Having shown the importance of the interfacial recombination at ETL/perovskite, we can suggest some methods that can lead to shifting the conduction band of SnO_2 related to the energy level of $(FAPbI_3)_{0.85}(MAPbBr_3)_{0.15}$ which can reduce the recombination at the interface. Modified SnO_2 with different methods speculate to be an excellent strategy to achieve the desired spike structure, taking into account the energy level of the perovskite layer. Applying some elements doping that have been involved with great potential such as Mg, Li, Y, Zn elements, and so on, but the amount doping of those elements should be optimized to make efficient conduction band according to the perovskite layer used. Also, using the graphene quantum dot (GQDs) treatment for SnO_2 could be the right way to enhance the extraction of the electrons and reduce the recombination as reported with $MAPbI_3$ as absorber layer [200]. Also, we can recommend the use of cesium carbonate Cs_2CO_3 to modified SnO_2 as found in organic solar cells, by changing the amount doping of Cs_2CO_3 [201] we can reach to the optimize conduction band of SnO_2 (-3.9 eV) as pointed above in our results.

2.4 Influence of the valence band offset of perovskite/HTL interface on PV performance

Suitable energy level alignment between perovskite and the hole transport layer is also a crucial key to improve the performance of PSCs. We have observed that the valence band maximum (VBM) of $(FAPbI_3)_{0.85}MAPbBr_3)_{0.15}$ is much lower (-5.71 eV) compared to highest occupied molecular orbital (HOMO) of Spiro-OMeTAD (-5.15 eV), that leads to an increase valence band offset (VBO = − 0.56eV), i.e. the difference between the valence band of the absorber layer and those of HTL is significantly high. As reported previously, $\Delta Ev < 0$ is a prerequisite to deliver high photovoltaic

parameters [183]. Here, we investigated the effect of VBO, by changing the electron affinity (χ) of Spiro-OMeTAD to make deeper (HOMO) level of HTL related to mixed perovskite to see which value of VBO can maximize the efficiency and the electron affinity of absorber and ETL were kept fixed as shown in Figure 8. Figure 9 a-b shows the influence of valence band offset variation on photovoltaic parameters of PSCs using the optimized conduction band offset (0.35 eV) for ETL/mixed-perovskite as discussed in the previous section. When the VBO is increased more than −0.56 eV (pristine Spiro-OMeTAD), V_{oc} decreases while J_{sc} remains unchanged; thus, FF and PCE significantly improved until VBO reaches a value of −0.41 eV, after this optimum value of VBO, we observed reduction in PCE and FF. It has been reported that decreased the VBO is preferable to reduce the charge recombination at interface, but high VBO results in low FF [16], we speculate this behavior does not originate from the beginning. There is an optimum value that can activate these processes due to the absorber energy level. In our case, we elucidated the optimum amount of VBO, equal to −0.41eV using in the same time the optimized value of CBO, according to our previous study [167] that deep lowest unoccupied molecule level (LUMO) of HTL respect to absorber layer allows to push the performance of PSCs. Here we have achieved this by using a similar HTL, but through optimized electron affinity, theoretically, that can deliver the peak performance of 26.50 %.

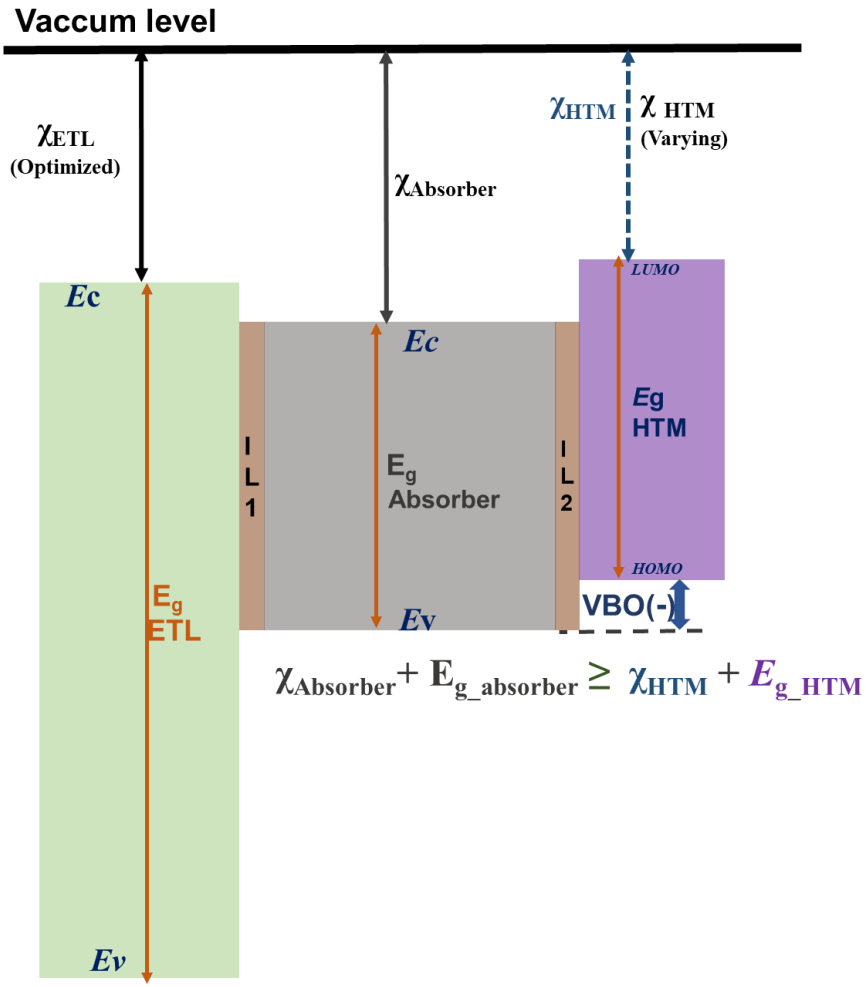

Figure 56: Band alignments of absorber/IL2/HTL layers with negative VBO when the electron affinity of the absorber is higher than the HTL. Here IL1 and IL2 are inserted to take into account the carrier recombination at the interface.

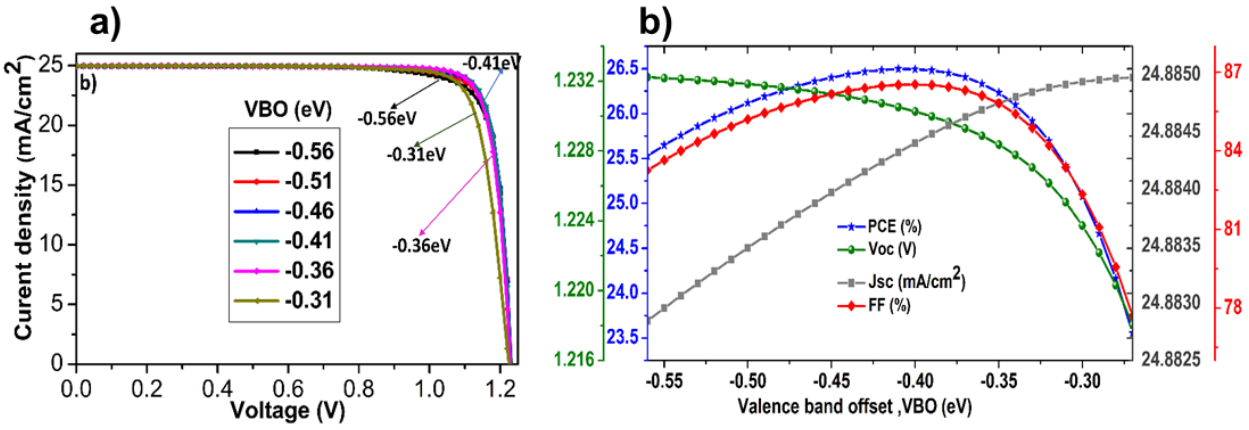

Figure 57 :(a) J–V curves of PSCs as a function of VBOs and (b) the effect of the electron affinity of HTL on the performance of PSCs.

2.5 Thickness optimization of the mixed perovskite absorber layer

In the case of a single cation perovskite layer such as $MAPbI_3$, many theoretical and simulation studies demonstrated that 500 nm could be the optimum thickness of the perovskite layer. In the case of a mixed cation-anion perovskite layer, controlling the optimum thickness has a significant effect on device performance. Thus, we investigated the impact of perovskite thickness in a range of 300 to 1400 nm on PV performance using optimized CBO and VBO at ETL /PSK and PSK/HTL interface, respectively. As illustrated in Figure *58*-a, with increasing the perovskite thickness, the FF drops monotonically related to the increased series resistance. V_{oc} mostly remain unchanged for up to 500 nm, beyond this V_{oc} dropped because with the thicker absorber layer the recombination dominates, the voltage can be presented by the equation (5) where n is diode ideality factor, I_o is dark saturation current, I_L is light -generated current, and $\frac{nKT}{q}$ is thermal voltage :

$$v_{OC} = \frac{nKT}{q} \ln\left(\frac{I_L}{Io} + 1\right) \qquad (45)$$

In case of the thick absorber layer, the carriers recombination rate become higher, leads to increase I_o more than I_L. Due to this reason, V_{oc} decreases with increasing the absorber thickness. On the other hand, thick layer absorbs more light, and thus charge carrier concentration increases, which results in a high value of J_{sc}. Subsequently, the PCE increases and reaches a maximum of 26.56 % at 641nm thickness; beyond this, it saturates and starts decreasing. With the high thickness of the absorber layer, the transfer of charge carriers becomes longer, leading to a higher rate of recombination. It can be deducted from Figure *58*-b; if the thickness of the perovskite layer increases, the external quantum efficiency (EQE) dramatically improved in the range of 641 -700 nm; after that, it increases slowly which can explain the improvement of J_{sc} even for higher thickness.

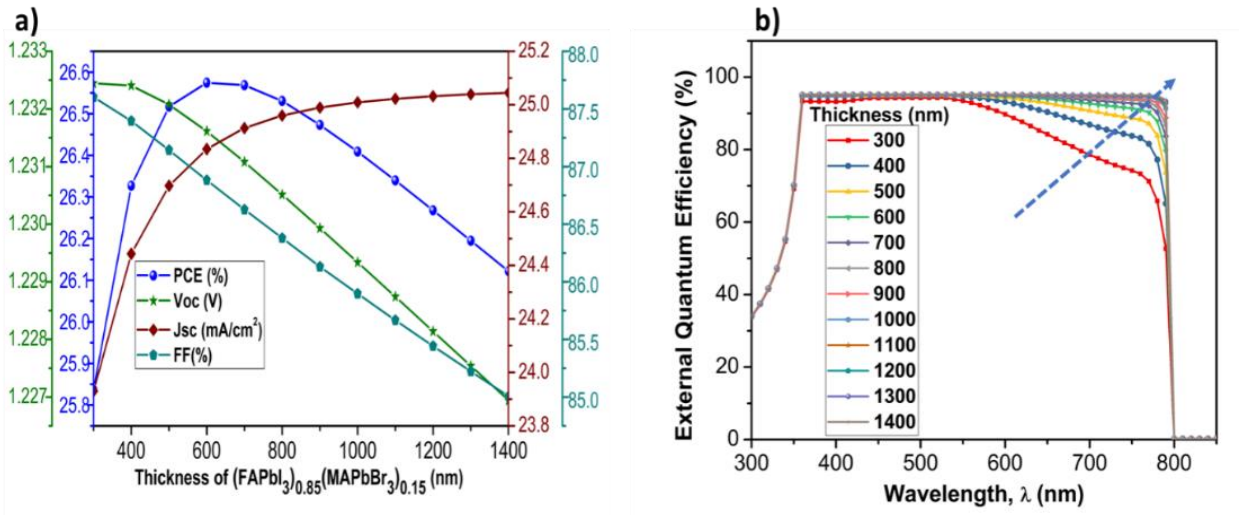

Figure 58 :(a) Influence of mixed perovskite absorber thickness on PV parameters for FTO/SnO_2/mixed perovskite/Spiro-OMeTAD/Au device and (b) external quantum efficiency of PSCs as a function of absorber layer thickness

5. Conclusion

Energy level engineering is paramount to reduce the interfacial recombination in PSCs. We investigated the influence of the conduction band offset (CBO) in planar PSCs by tuning the electron affinity of SnO_2 as a selective charge layer in a mixed perovskite environment through numerical analysis using SCAPS. This was established on the absorption coefficient, which was derived from the experimental data set. We found that the performance of the solar cell is affected by conduction band offset at SnO_2/$(FAPbI_3)_{0.85}(MAPbBr_3)_{0.15}$, and noted the formation of "spike-type'' band alignment, that is favorable as compared to "Cliff-type''. This, in turn, decreases the recombination rate at the SnO_2/$(FAPbI_3)_{0.85}(MAPbB_3)_{0.15}$ interface with an optimized value of CBO elucidated to be 0.35eV, which will lead to a competitive PCE of 25.61%. The modified valance band of Spiro-OMeTAD was found to attend 5.3 eV, while the optimum thickness of the mixed perovskite layer at 641nm yielded a power conversion efficiency of 26.56%. Our mechanistic insights demonstrate that band-alignment engineering at ETL/perovskite and perovskite /HTL is a vital strategy to push the performance of PSCs to their full thermodynamic potential, which can be effectively achieved by designing new charge selective layers or tweaking its intrinsic (Physico-chemical) properties.

Chapter 6: Unraveling of theoretical window for high-performance inorganic perovskite solar cells

ABSTRACT

Perovskite solar cells (PSCs) have celebrated a decade of intense investigation as a promising photovoltaic technology, measuring a power conversion efficiency of >25.2% with the use of lead-based light harvester. Recently, Inorganic cesium cation based mixed halide perovskite (CsMI3-xBrx, M=Pb, or Sn) as an absorber in PSCs gave promising results; notably, CsPbI2Br demonstrated improved thermal stability and carriers transport properties. However, the performance is far-off from the theoretical limit due to intriguing issues such as high defect density (Nt), energetic level mismatch. Such a barrier can be overcome through device modeling and the unraveling of the kinetics. Here we have employed a computational approach to design and investigate efficient inorganic $CsPbI_2Br$ based solar cells by elucidating the role of defect density in the perovskite on the performance by applying different types of hole transport layers via optimizing their valence band offset and barrier height at back contact. By optimizing such parameters for $CsPbI_2Br$, the efficiency of 17.71, 17.44, and 17.54 % using CuSCN, PTAA, and Spiro-OMeTAD as HTMs respectively can be reached. Furthermore, lead-free CsSnI3-xBrx (0<x>3) based PSCs were simulated, and the effect of band gap variation as a result of Br content was studied on the performance. The influence of defect density of the absorber layer ($CsSnIBr_2$) and at of interfaces was studied, and with optimized defect density, CsSnIBr2 based PSCs gave an efficiency of 20.32 % with Voc of 1.35 V when SnO_2 was used as the electron transport layer and Spiro-OMeTAD as an HTM. Our simplistic approach suggests a way for experimental design protocol to achieve high-performance inorganic Pb and Sn-based PSCs.

.

1 Introduction

Solar energy is one of the most promising sources of energy to counter the adverse effect of climate change on our planet. Among the photovoltaics, emerging technologies have the potential to reach the masses, particularly perovskite solar cells (PSCs). The hybrid organic, inorganic lead (Pb) based perovskite as a light absorber ($APbI_3$) is the most investigated in PSCs due to their excellent electro-optical properties [41,113,118,128,129] and gave record performance. [202],[203]However, hybrid organic-inorganic lead halide perovskite suffers from challenges such as thermal instability at high temperature, originating due to the volatile nature of organic cations (FA or MA). [25,30] Replacement of the organic cations by inorganic cations such as Cs found to be an effective route to overcome such bottleneck.[204,205] However, the $CsPbI_3$ is stable only in the cubic perovskite (α-phase) at high temperature, which can be easily converted to orthorhombic non-perovskite (δ) phase.[206]In this context, $CsPbI_{3-x}Br_x$ evolved as a promising material for the diverse architect of PSCs in term of phase stability, with the fraction of 1 for Bromide (Br), Snaith et al. showed that $CsPbI_2Br$ is stable in the cubic phase at room temperature with a rational band gap of 1.82 - 1.92 eV [207], partial substitution of I to Br into $CsPbI_3$ stabilizes the cubic phase, this led to intense investigation and performance of $CsPbI_2Br$ based PSCs up to 16.07 % was reported. [208]Such results were obtained by reducing the defect density in the active layer, growth control of $CsPbI_2Br$ through optimized annealing temperature[209], using effective anti-solvent approach [210] or minimizing the energy level gap at the charge selective layers[211], similar to hybrid lead halide PSCs.[167]However, the performance remains lower from the theoretical limit of 22.1 % and 1.65 V for PCE and $V_{oc,}$ respectively, when 500 nm thick $CsPbI_2Br$ was used.[212]To achieve the theoretical efficiency limit, the strategy should be focused on reducing the defect density of the active layer, and it should be less than the current value of 3.64 E15 cm^{-3}. [213]The energy alignment at the charge selective layers needs further optimization using p-type conducting polymers or inorganic semiconductors to minimized energy loss ($E_{loss} = E_g - eV_{oc}$), E_g is the band gap and e is the elementary charge). Arguably, the efficient $CsPbI_2Br$ based PSCs should focus on reducing E_{loss} as much as possible by improving V_{oc} and $J_{sc,}$ this target can be achieved through energy alignment and high-quality $CsPbI_2Br$ crystal deposition. The most efficient $CsPbI_2Br$ based PSCs yielded PCE of 16.79 % with an V_{oc} of 1.32 V, i.e., E_{loss} = 0.59 eV [214], these results will pave way to design efficient $CsPbI_2Br$ based PSCs.

The toxicity of the lead (Pb) metal is a barrier to the commercial success of inorganic PSCs. (Sn) is seen as possible metal to replace the problematic Pb [215]. Compared to Pb-perovskite, Sn-based perovskites showed high optical absorption coefficients [216,217], narrow optical band gaps, and high charge carrier mobilities. [218] In accordance with the perovskite structure, $ABX_{3,}$ the A cation can be (MA, FA, and Cs). In the case of MA cation, an efficiency of 6.4% was achieved by using $MASnI_3$ as light harvester having a band gap of 1.3 eV. [175] Further, using FA cation, slightly larger than MA, Koh et al. .prepared $FASnI_3$ with the incorporation of 20 % SnF_2 addition, a PCE of 2.10% was achieved with a band gap of 1.41eV. [219] However, the instability of organic-inorganic halide perovskite has become troublesome for commercial applications, due to the behavior of organic cations under outdoor conditions. [220] To resolve this stability issue, Cs as A cation was opted for all inorganic Sn-

based perovskites with X = I, Br, which has similar electro-optical properties to $FASnI_3$ and $MASnI_3$. The first report using Sn-based all-inorganic PSCs was reported in 2012, where $CsSnI_3$ acted as hole transporter yielded a PCE of 0.9 %. [221]However, the instability of Sn in the +2 oxidation state, which can be easily converted to the +4 state in the presence of moisture and oxygen [222] was a limiting factor. To resolve the oxidation instability of Sn, $SnCl_2$, and SnF_2 as reducing agents was exploited to minimize the extent of *p*-type self-doping of the perovskite and to reduce the hole carrier density and thus enhanced the performance.[223,224] Besides, mixed anion containing $CsSnI_{3-x}Br_x$ as light harvester has been exploited, where its band gap can be tuned from 1.27 eV to 1.74eV by changing the percentage of Br from x = 0 – 1. [225]

Although these Inorganic Sn-based PSCs shows lower performance compared to their Pb based counterparts, their low band gap exhibit a great potential to exploit them in perovskite-perovskite tandem solar cells. Further, investigation of the macroscopic device model of inorganic Sn-based PSCs is still obscure, and a lot of issues need to be resolved to improve the Sn-based PV technology, such as prevention of bulk and interface recombination due to tin vacancies, rational designing of selective charge contacts to efficiently extract carriers from perovskite. The issue of high hole carrier density as a result fo self p-doping can be controlled by SnF_2 addition, which will allow reducing the defect density from the pristine value of 1.1E19 cm^{-3} to 5.7E17 cm^{-3} for $CsSnI_3$. This can be retarded furthermore by substitution of I to Br. Taking such factors into account, we performed a theoretical investigation for $CsPbI_2Br$ and $CsSnI_{3-x}Br_x$ based PSCs. Firstly, we focus on $CsPbI_2Br$ PSCs by studying the effect of interface engineering at HTL and perovskite interface employing different HTLs such as organic (Spiro-OMeTAD), inorganic (CuSCN) and polymeric (PTAA). Also, the effect of the defect density of the $CsPbI_2Br$ absorber layer on the performance of cells was studied. The HTL is a channel to transfer the holes from the active layer to back contact of cell, which should be optimized to make a better alignment. For such reasons, we have investigated the effect of the valence band (E_V) of HTLs (Spiro-OMeTAD & PTAA) on the performance of $CsPbI_2Br$ solar cells. During this process, we discovered that modulating the E_V (by varying the electron affinity) of HTL, leads to an arc shape at HTL/back contact which changes its curvature with the variation of E_v and that has a strong influence on the performance of PSCs. All these optimizations yield to an efficiency of 17.73, 17.45, and 17.44% using CuSCN, PTAA, and Spiro-OMeTAD as HTLs, respectively.

Most of the PSCs studies are focused on optimizing the valence and conduction band offset, which is critical for transport and extraction of charges as the height of the energy barrier regulates the contact resistance. However, reports showing the effect of energy band alignment between HTM and back contact are scarce. Earlier, we reported that a valence band offset should be optimized to boost the performance of PSCs. Thus, to address the mismatch alignment at perovskite/ HTM/back contact, in the first part, we have elucidated the impact of valence band maximum (VBM) of HTMs (Spiro-OMeTAD, CuSCN & PTAA) on the performance of CsPbI2Br solar cells and also on the contact between HTM-Back contact. During this process, we discovered that modulating the EV (by varying the electron affinity) of HTM leads to an arc shape forms at HTM/back contact, which changes its curvature with the variation of Ev and that has a strong influence on the performance of PSCs. Such optimizations

yield to an efficiency of 17.73, 17.45, and 17.44% using CuSCN, PTAA, and Spiro-OMeTAD as HTMs, respectively.

Secondly, we simulated lead-free Sn-based inorganic PSCs, where the effect of I anion substitution by Br in CsSnI3 absorber was investigated to clarify its impact on the conduction band offset (CBO), i.e., the difference between the conduction band minimum (CBM) energy levels of the ETL and those of the perovskite layer, ΔEc= Ec_ETL – Ec_absorber.

To our understanding, there are no theoretical or experimental studies emphasized on lead-free inorganic PSCs. The ‘’self-doping‘’ in Sn-based inorganic PSCs allows lowering the trap density, and its impact on solar cell performance was studied. We studied the influence of defect density variation in the absorber layer and its interfaces to elucidate the optimum values that can boost the efficiency and computed 20.35 % PCE with a Voc of 1.35 V.

1. Theory and Computational details

The simulations were performed using SCAPS 3.3.07 software[167], based on the Poisson equation(39), and the continuity equations for electrons(40) and holes (41)

$$\frac{d}{dx}\left(\varepsilon(x)\frac{d\Psi}{dx}\right) = q[\,p(x) - n(x) + N_D^+(x) - N_A^-(x) + p_t(x) - n_t(x)\,] \quad (39)$$

$$\frac{1}{j}\frac{\mathrm{d}J_p}{\mathrm{d}x} + R_p(x) - G(x) = 0 \quad (40)$$

$$-\frac{1}{j}\frac{\mathrm{d}J_n}{\mathrm{d}x} + R_n(x) - G(x) = 0 \quad (41)$$

Here, ε denotes the permittivity, q, the charge of the electron, Ψ, the electrostatic potential, n, the free electrons, p, free holes, n_t and p_t are trapped electrons and holes, N_D^+ and N_A^- are the ionized donor and acceptor-like doping concentrations respectively, Rn and Rp are electrons and holes recombination rate, G is the generation rate, Jn and Jp are, the electron and hole current densities respectively.

The symbols presented in table 1 and 3 are , N_A and N_D denote acceptor and donor densities, ε_r is relative permittivity, χ is electron affinity, E_g is the band gap energy, μ_n and μ_p are mobility of electron and hole, and N_t is defect density.

Computational studies were performed on a planar PSCs with an architecture of FTO/SnO_2/interface layer 1(IL1) / inorganic perovskite absorber /interface layer2(IL2)/HTL/Au. The defect type in bulk perovskite is considered neutral with a cross-section of electron and hole is 2×10^{-14} cm^2. The electron and hole thermal velocity was 10^7cm/s. Gold (Au) was used as the back while fluorine doped tin oxide (FTO) as the front contact, and AM 1.5G solar illumination of 100 mW/cm^2 was used for simulative studies.

Most of the studies in PSCs are focusing on designing optimal conduction band offset and forgotten that efficient extraction of holes outside the device needs to balance the energy alignment from the perovskite layer to the back contact. To address this challenge in the mismatch alignment at HTL-Perovskite-Back contact, we have

elucidated the impact of valence band energy of two HTLs on the performance of inorganic PSCs based on $CsPbI_2Br$.In our previous study, we demonstrated that a valence band offset should be optimized to boost the performance of PSCs [226]. For those reasons; the first part of this study will clarify the impact of VB of HTL on the performance of cells and also on the contact between HTL-Back contact.

The following lines will describe the fundamental of interfaces at Metal-Semiconductor [19]; ϕ is the work function, sp, and m refer to p-type semiconductor and metal, respectively. E_F is the fermi-energy, and χ is the electron affinity. If the metal and semiconductor brought together, two types of contact could be found depending on the difference of work functions: ohmic junction and Schottky junction, as illustrated in the figure.59 a-b. The interface type is a result of the work function levels to balance the

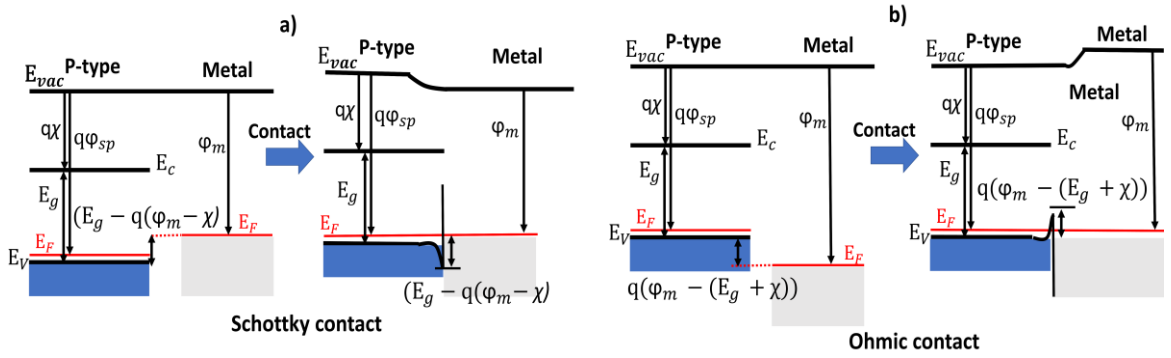

Figure 59 : The energy band diagrams for semiconductor-metal interfaces. a) Schottky contact . b) Ohmic contact.

chemical potential. In the case of p-type semiconductor which our study will focus on it, if the work function of HTL, which is the p-type semiconductor is higher than that of the metal, as shown in Figure 59 -a, a barrier of holes create is called, Schottky contact. Otherwise, if the work function of HTL is lower than that of the metal, an ohmic contact will form, which is mentioned in Figure 59-b. To analyze the effect of these two contacts on the performance of PSCs, we will vary the valence band of Spiro-OMeTAD and PTAA as HTLs, which can create the desired interfaces at HTL-metal. The optimum level of the valence band for each HTL will optimize according to the point when the performance of $CsPbI_2Br$ PSCs is maximized. The barrier height between a p-type semiconductor and metal is defined using two formula $(\boldsymbol{\phi_{B-p}} = (\boldsymbol{E_g} - \boldsymbol{q}(\boldsymbol{\phi_m} - \boldsymbol{\chi})$ $\boldsymbol{or}$ $\boldsymbol{\phi_{B-p}} = (q(\varphi_m - \chi) - E_g)$ depending the type of contact. The valence band offset (VBO) is the difference between the valence band energy of the perovskite layer and those of HTL VBO= $E_{V\text{-}PSK}$-$E_{V\text{-}HTL}$. In the second part of this study, we analyzed the conduction band offset (CBO), which is the difference between the conduction band energy of ETL and those of perovskite layer CBO= $E_{C\text{-}ETL}$-$E_{C\text{-}PSK}$.[226]

An online package also is used to calculate the Shockley Queisser limit for the single-cell according to the band gap of the absorber layer.[227]

2 Results and discussion

2-1 $CsPbI_2Br$ PSCs

2-1-1 Performance of $CsPbI_2Br$ PSCs using different HTLs

The photon absorption leads to the creation of an electron-hole pair in a PSC; the electrons travel to the front side through electron selective layers, while selective hole layers conduct the holes to the backside. To make this process efficient, the energy levels of the interface layers should be in the equilibrium conditions to maximize charge transfer. For efficient transfer of holes, rational HTL with a suitable energy level match with $CsPbI_2Br$ (absorber layer), and the metallic cathode (Au) as the back contact is a prerequisite.

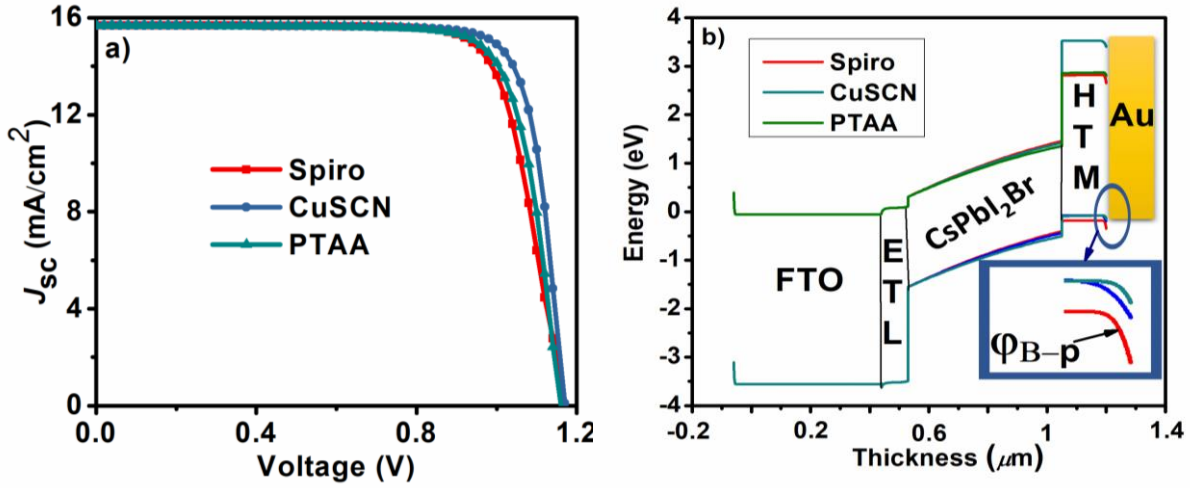

Figure 60 :J-V curves of PSCs based on different HTMs using parameters shown in Table 1 b) : Corresponding energy band diagrams of the inorganic $CsPbI_2Br$ based PSCs using different types of HTM showing energy barrier at HTM and back

We investigated the effect of tuning of the valence band by studying a series of HTLs, Spiro-OMeTAD, PTAA ,and CuSCN in a structure of FTO/SnO_2/IL1/$CsPbI_2Br$/IL_2/HTLs/Au and the preliminary results are shown in table 10.

Table 8: Parameters Used in the SCAPS Simulation of Pb based inorganic PSCs.

Parameter	IL1	$CsPbI_2Br$	IL2	PTAA	CuSCN[167]
Thickness (nm)	10	500	10	150	150
E_g (eV)	1.86 [228]	1.86 [228]	1.86 [228]	2.95 [229]	3.6
χ	3.8 [228]	3.8 [228]	3.8 [228]	2.3 [229]	1.7
ε_r	8.6	8.6	8.6	3.5 [230]	10
N_c (1/cm^3)	2.2E18	2.2E18	2.2E18	2.2E18	2.5E18
N_v (1/cm^3)	1.8E19	1.8E19	1.8E19	1.8E19	1.8E19
μ_n(cm^2/Vs)	200 [231]	200 [231]	200 [231]	1E-4 [193]	100
μ_p (cm^2/Vs)	200	200	200	1E-4	25
N_A (1/cm^3)	--	--	--	-	1E18
N_D (1/cm^3)	1E15	1E15	1E15	1E18	-
N_t(1/cm^3)	3.64E16	3.64E15[213]	3.64E16	1E15	1E15

Figure 60 presents the *J-V* characteristics of inorganic lead-based PSCs with different HTLs using the parameters in Table 8 and for spiro-OMeTAD from Table 2. It can be deducted that the employed HTLs represent similar J_{sc} of around 15.67 mA/cm^{2,} which does not influence the Quantum efficiency (QE) of PSCs. At the same time, the fill factor (FF) significantly varies by changing the HTL and reaches 76.66, 79.01, and 81.94 % for Spiro, PTAA, and CuSCN, respectively, suggesting favorable interfacial contact at $CsPbI_2Br$/HTL. To compare and confirm our first model of simulated PSCs, we summarized in Table 9; some reported PSCs based on $CsPbI_2Br$ with the same configuration that we used. Regarding our results, It can be noted that the valence band maximum (E_v) value of -5.30 eV for the CuSCN can deliver the highest PCE of 14.90 % in contrast to PTAA (-5.25 eV) with an efficiency of 14.28%. In comparison, Spiro-OMeTAD (-5.45 eV) gave a slightly lower PCE of 14.09%. The value of the defect density of $CsPbI_2Br$ is equal to 3.64E15 cm^{-3} which is the finest value[213] and the work function of back contact is -5.1 eV (Au), added to the high mobility of the free charges in inorganic HTLs compared with the organic or polymer HTLs, this difference in the performance between those HTLs, may be related to two parameters, the first one; the effect of VBO and the second one the barrier height (ϕ_{B-p}) as presented in table 10.

We can conclude here that the efficient cells need to have a balanced value between the VBO and ϕ_{B-p} to facilitate the extraction of the holes from the perovskite layer and also to make an efficient transfer of the holes from the HTL to the outside of cells.

Table 9: A Summary of performance parameters of reported CsPbI2Br based on Spiro-OMeTAD and PTAA as HTL.

HTLs	**PCE (%)**	**Voc (V)**	**Jsc (mA /cm2)**	**FF (%)**
Spiro[228]	13.10	1.21	14.60	74.1
PTTA[232]	14.36	1.16	15.56	79.06

Table 10 : Performance of FTO/SnO_2/IDL1/$CsPbI_2Br$/IDL2/HTLs/Au using different HTLs

PSCs configuration	**PCE (%)**	**Voc (V)**	**Jsc (mA /cm2)**	**FF (%)**	**VBO (eV)**	ϕ_{B-p}
Spiro	14.09	1.17	15.67	76.66	-0.21	-0.35
PTAA	14.28	1.15	15.67	79.01	-0.41	-0.15
CuSCN	14.90	1.16	15.68	81.94	-0.36	-0.2

*PSk:$CsPbI_2Br$

As shown in Figure 60, the corresponding energy band diagrams of simulated PSCs with diverse HTLs. We can analyze clearly from the zoom box the formation of an "arc-

shaped" at HTL/back contact with different curvature depending on the valence band energy used for each HTL, and that may act as a barrier to slow down the movement of holes toward the back contact which increase the recombination rate that lowered the voltage. Also, we can notice, as explained in Figure-60-b, that the Shockley contact is dominated for all three HTLs with different levels as presented with ''arc-shaped''.

2.1.1.1 Effect of defect density (N_T) of $CsPbI_2Br$ on the performance of PSCs

The performance of the diverse structures simulated here is in accordance with the recent experimental studies but is still far from the theoretical values. Arguably, the optimization of the selective layers will be rational if the active layer is of high quality (low defect density). The defect density influences the performance of the cell; we will elucidate the effect of this parameter on the performance of PSCs with different HTLs. N_t is based on the Shockley-Read-Hall recombination (R_{srh}) [22,233]

$$R_{srh} = \frac{n_p - {n_i}^2}{\tau_p(p+p_i)+\tau_n(n+n_i)} \quad (42)$$

$$L = \sqrt{D\tau} \quad (43) \qquad \tau_{n,p} = \frac{1}{\sigma_{n,p}\vartheta_{th}N_t} \quad (44) \qquad D = \frac{\mu T K_B}{q} \quad (45)$$

ϑ_{th} is thermal velocity, N_t is defect density, n and p are the concentration of electron and hole.

K_B and μ represent Boltzmann constant and mobility, q and T represent the magnitude of charge and temperature in Kelvin.

It can be noted that R_{srh} is directly proportional to the defect density of the absorber layer. Also, we can consider the formula of carrier diffusion length (L) to analyze the effect of N_t on the performance of the device according to the SRH effect and diffusion length relation. Here L is the diffusion length τ the charge carrier lifetime and D is the diffusion coefficient. The equations (4,5 and 6) highlight the direct relation between the defect density and lifetime of free charges in bulk perovskite, which can control the performance of devices.

Figure 61 shows the change in the efficiency and the voltage as a function of defect density in $CsPbI_2Br$ with different HTLs. It is known that the defect density of the absorber layer directly affects the performance of PSCs, which is a limiting factor in achieving the Schockley-Queisser limit.[234,235]

It can be deducted from Figure 61-a, that with decreasing the N_t of absorber layer up to a specific value of N_t=1E13 cm^{-3}, the increase in PCE can be observed for all the three HTLs studied. The lower defect density resulted in the increased liftime as a result of increased diffusion length (a measure of absorber quality), which reduces the rate of recombination in the absorber layer. In comparison to the extracted PCE value for the high defect density of absorber (3.64E15 cm^{-3}) and the optimized defect density (N_t=1E13 cm^{-3}) By comparing the extracted PCE value(table 10).

For the high defect density of absorber (3.64E15 cm^{-3}) and the optimized defect density (N_t=1E13 cm^{-3}) leads to an increment in PCE to 16.16, 17.44, and 17.71 % for Spiro-OMeTAD, PTAA and CuSCN respectively Figure 61-a.

Table 11: *Parameters Used in the SCAPS Simulation of lead-free inorganic PSCs.*

Parameter	**FTO**	**SnO_2**	**IL1**	**$CsSnI_{3-x}Br_x$**	**IL2**	**Spiro-OMeTAD**
Thickness (nm)	400	90	10	350	10	150
E_g (eV)	3.5	3.6 [189]	Wide range	Wide range	Wide range	3 [37,38]
χ	4	4	4.47	4.47 [238]	4.47	2.45[237]
Ɛr	30	100	48	48 [239]	48	3[237]
***Nc* (1/cm^3)**	2.2E18	2.2E18	2.2E18	2.2E18	2.2E18	2.2E18
***Nv* (1/cm^3)**	1.8E19	1.8E19	1.8E19	1.8E19	2.5E19	1.8E19
μ_n(cm^2/Vs)	20	240 [193]	6	6 [224]	6	2E-3[237]
μ_p (cm^2/Vs)	10	240	6	6	6	2E-3
N_A (1/cm^3)	--	-	1E13	1E13	1E13	1E18
N_D (1/cm^3)	2E19	1E17	-	-	-	-
N_t(1/cm^3)	1E15	1E15	Wide range	Wide range	Wide range	1E15

A similar trend was observed in the case of the voltage, where V_{oc} increases with decreasing N_t until reaching the optimized value of 1E13 cm^{-3}, as illustrated in Figure 61-b. However, the improvement in the voltage is higher when we use CuSCN and PTAA as HTLs, 1.43, and 1.42 V, respectively, compared to Spiro-OMeTAD, 1.28 V, as mentioned in

Table 10, in the case of Spiro-OMeTAD, the VBO is less, but the barrier height is large on the contrary to other HTLs. We can, that even if the defect density of perovskite layer is low (high quality of fabrication) with less VBO will not help the voltage to cross the theoretical value (case of spiro-OMeTAD), but if the barrier height is less with large VBO, the performance can be near to the Shockley limit as showed with CuSCN and PTAA.

To confirm these conclusions, we will change the valence band energy level of Spiro-OMeTAD and PTAA by varying their electron affinity, to be closer to the VBO and ϕ_{B-p} values of CuSCN, which it is experimentally achievable.

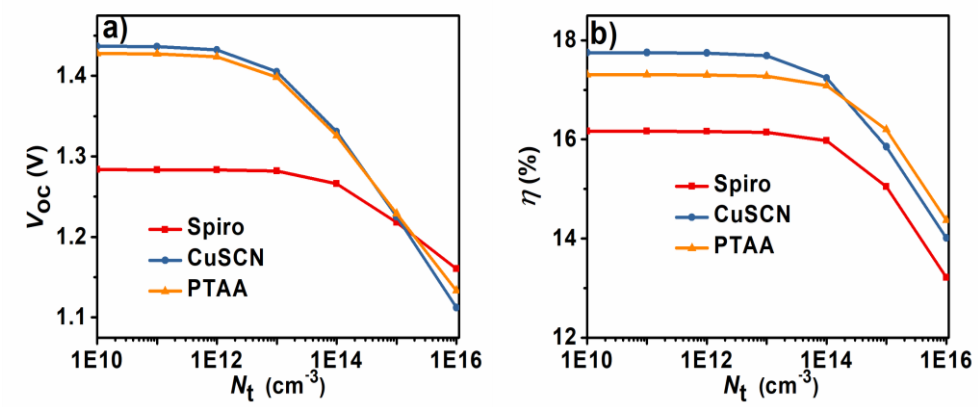

Figure 61 : the effect of defect density in absober layer with divese HTMs on ,a)Votgae , b) effeciency .

2.1.1.2 The influence of HTL's valence band on the performance of PSCs

Figure 62 represents the influence of the valence band of Spiro and PTAA on the performance of PSCs and their corresponding energy band diagrams. The valence band of HTL ($E_{v,}$ HTL) was varied through the simulation by tuning the electron affinity (χ) when the valence band maximum (VBM) of HTL decreases concerning the absorber valence band maximum(-5.66eV), the PCE and the V_{oc} increases when the value of VBM reaches closer to the work function of back contact (-5.1 eV), the PCE and the V_{oc} saturates, but when electron affinity value is higher than -2.25 eV and -2.3 eV for Spiro and PTAA Figure 62a-c respectively, the performance dropped suggesting the optimized value of E_v when gold is used as back contact.

Table 12: Performance of inorganic PSCs using different HTLs, related to the VBO and φ_{B-p}

HTMs	E_v (eV)	VBO (E_v_HTM-E_v_absorber) (eV)	φ_{Bp}(eV)	PCE (%)
Spiro-OMeTAD	-4.7	-0.96	-0.4	9.82
	-5	-0.66	-0.1	14.28
	-5.1	-0.56	0	15.79
	-5.25	**-0.41**	**-0.15**	**17.57**
	-5.4	-0.26	-0.3	16.29
	-5.55	-0.11	-0.45	14.28
PTAA	-4.55	-1.11	-0.55	7.95
	-4.85	-0.81	-0.25	12.03
	-5.15	-0.51	-0.05	16.52
	-5.25	**-0.41**	**-0.15**	**17.44**
	-5.3	-0.36	-0.2	17.36
	-5.4	-0.26	-0.3	16.25

Related to the engineering of the interface in optoelectronic devices, we can explain these results with two manners when the valence band of HTLs varied affect

directly and at the same time the VBO and the barrier height (ϕ_{B-p}) at HTL-Back contact. Which means, an optimize value of VBO and ϕ_B should be found for each HTL related to the valence band of HTLs.

To further elucidate this, we analyzed the band diagram of devices with a different value of E_v for each HTL (Figure 62 b-d). If we focus on the area between the HTL and the back contact with the change of the E_v of HTLs, the performance increase with increasing the VBO until an optimum value which found to be -0.41, means 2.25 and 2.3 eV as electron affinity for Spiro and PTAA respectively and, beyond these optimized values of VBO, the performance drops due to the Schottky barrier for hole which increases with increasing the E_v of HTL as illustrated in the zoom box in Figure 62 b-d and Table 12 . If the Schottky barrier is high, it will hinder the transfer of the holes to the back contact, which leads to decrease the performance of $CsPbI_2Br$ based PSCs. According to the variation of the efficiency as summarized in Table 12, the Schottky contact is preferable with -0.15 eV as the barrier height.

Table 13 illustrates the performance of $CsPbI_2Br$ PSCs with the optimized parameters, N_t for absorber layer, VBO and (ϕ_{B-p})

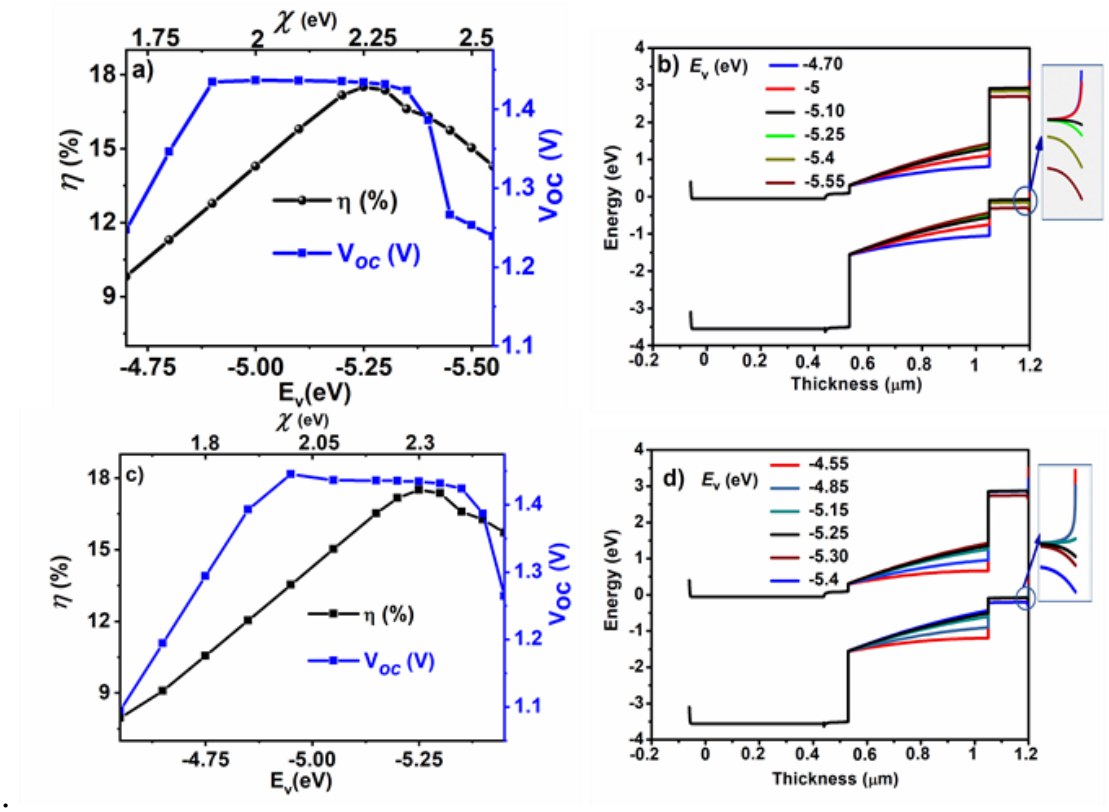

Figure 62 : a) Influence of valence band of Spiro-OMeTAD on the performance of CsPbI2Br PSCs, b) corresponding energy band diagram, c) influence of valence band of PTAA on the performance of $CsPbI_2Br$ PSCs and d) corresponding energy band diagram.

Table 13 : The performance of the optimized FTO/SnO_2/IDL1/$CsPbI_2Br$/IDL2/HTLs/Au based on different HTLs, compared to the Shockley-Queisser-limit

HTLs	PCE (%)	Voc (V)	Jsc (mA /cm^2)	FF (%)
CuSCN	17.71	1.43	15.90	78.90
PTAA	17.44	1.43	15.69	77.76
Spiro	17.57	1.43	15.69	78.31
Shockley-Queisser-limit[240]	25.86	1.56	17.99	91.69

2.2 Lead free $CsSnI_{3-x}Br_x$ PSCs

2.2.1 Effect of bromide substitution on the performance of $CsSnI_{3-x}Br_x$

It is reported that the addition of SnF_2 (20 mol%) allows decreasing the defect density in $CsSnI_3$ from 1.1E19 cm^{-3} to 5E17 cm^{-3}, by influencing the morphology of $CsSnI_3$.[167] Similarly, in present work, we have focussed on the $CsSnI_3$ where Iodine was partially replaced by bromide anion; as a result, of the band gap variation. Further, the effect of band gap variation was studied on the performance of the $CsSnI_{3-x}Br_x$ based solar cells. Figure 63-b shows the simulated trend of PCE and V_{oc} as a function of the band gap for the planar device structure FTO/SnO_2/$CsSnI_{3-x}Br_x$/spiro-OMeTAD/Au and using the parameter given in table 11.

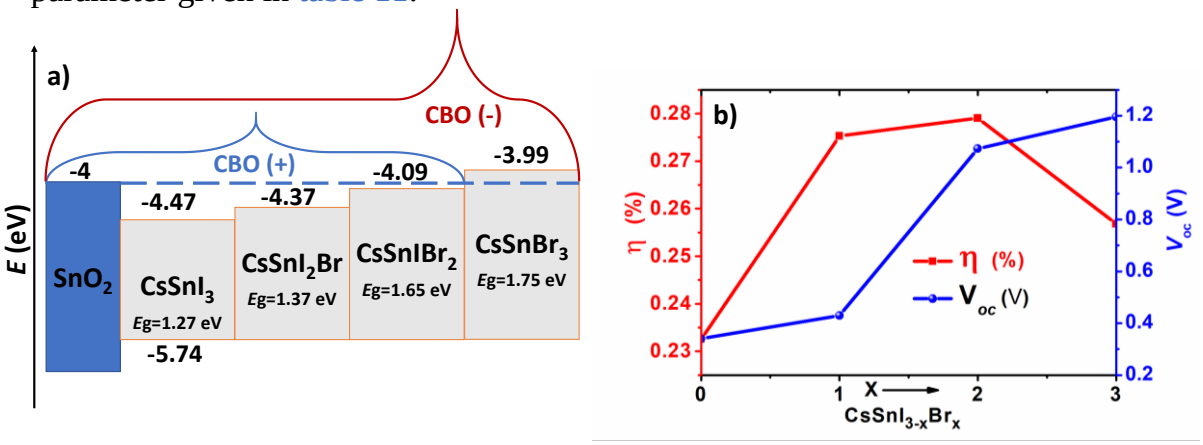

Figure 63 : a) Energy levels diagram (relative to the vacuum level) of CsSnI3-xBrx films by varying its electron affinity with respect to SnO2 as ETL .b) The influence of CsSnI3-x Brx band gap on the PCE and Voc of PSCs

Corresponding to Br/(I + Br ratio, (x) ranges from 0–3, the band gap was varied from 1.27 −1.75 eV. A similar trend was noted in $CH_3NH_3PbI_3$ and $CsSnI_3$,[225,241] on the experimental hand, which validate our investigation. Figure 63-b shown that the open-circuit voltage (V_{oc}) escalates with the increase in band gap due to increased Br fraction, while PCE starts to get drop beyond x=2. The improvement of V_{oc} is a consequence of the band gap increment due to high Br content; however, on the other hand, it reduces the absorption in the visible region due to a wide band gap. To emphasize here, we have employed SnO_2 as ETL, as the selective layer plays a crucial role in reducing the recombination rate, particularly the mismatch in energy level alignments at ETL/perovskite interface may increase the recombination. This could be explained by the conduction band offset (CBO), i.e., the difference between the conduction band minimum of ETL and those of perovskite layer ($\pm\Delta \boldsymbol{Ec}$),[16] the (+) sign represents the spike structure, and the (-) sign is the cliff structure as reported in our last study.[226] In the past studies, the spike structure is shown to be beneficial for improving the performance of PSCs, which can build a potential barrier at ETL/perovskite to reduce the recombination rate[182]. From our theoretical and experimental observation, with the increase in the band gap of perovskites, only *Ec* is assumed to shift upwards; therefore, the CBO becomes smaller with an optimum value of +0.09 eV (spike structure) for $CsSnIBr_2$ which gave the best performance as shown in Figure 63-a. Thus, the PCE decreases dramatically after x=2, and the following equation can describe the Voc.[198,199]

$$V_{oc} = \frac{E_A}{q} - \frac{nkT}{q} ln \frac{J_{00}}{J_{sc}} \quad (46)$$

$$E_A = E_g - \Delta E_C \quad (47)$$

V_{OC} is open-circuit voltage; E_A is the activation energy, n is diode idealist factor, K is Boltzmann constant, T is temperature, J_{00} is current prefactor, and J_{sc} is short circuit current density. For T =0 K, V_{oc}= E_A/q. The CBM of bulk $CsSnI_3$ compared to the CBM of ETL is much deeper, thus a large energy barrier with ΔE_C= +0.47eV affects the performance of the cell. By adding Br to the $CsSnI_3$ leads to increase the band gap by shifting the conduction band upwards which enhances the matching energy level with ETL and the ΔE_C become small enough to facilitate the transfer of electrons toward the front side of the cell with the increasing of activation energy as well V_{oc} become higher. The performance of our fist model using $CsSnIBr_2$ is still low which match with the experimental funding in some studies, and that may due to the low defect density in the absorber layer and also at the selective layers

2.2.2 The effect of defect density of the absorber layer on the performance of cells

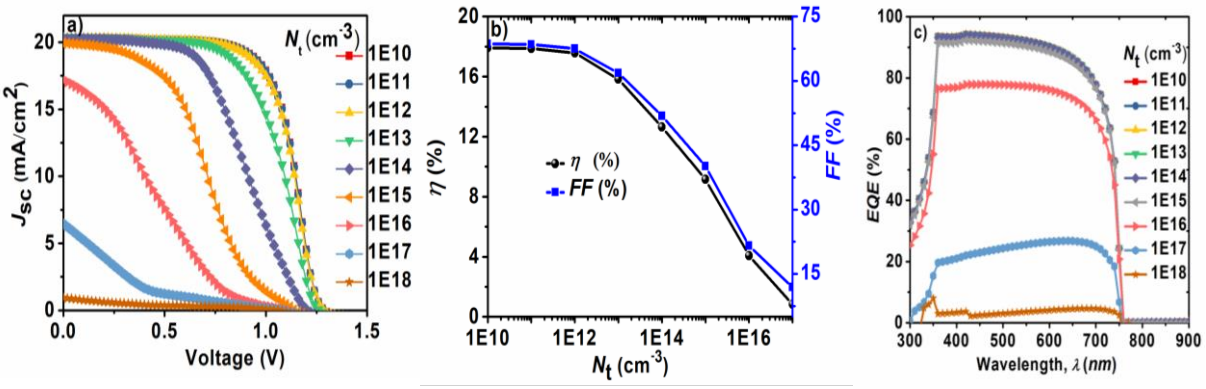

Figure 64 : Influence of defect density in absorber layer on a) J-V curve, (b) efficiency and fill factor and c) the external quantum efficiency

To explain the low performance of $CsSnI_{3-x}Br_x$ based PSCs, as mentioned in the above section, we have chosen the $CsSnIBr_2$ as an absorber layer, which has a favorable energy level alignment with SnO_2 as ETL. Also, we assume that the defects in inorganic Sn-based perovskite will have a significant effect on the performance of inorganic lead-free PSCs; thus, the impact of defect density(N_t) will be studied in the subsequent section.

Figure 65 represents the influence of defect density in the absorber layer on the photovoltaic properties of Sn-based inorganic PSCs. It can be deduced that the high defect density leads to a drop in the performance of the devices. We noted that the performance remains unchanged when the values of N_t become <1E12 cm$^{-3,}$ but if it is higher than this value, then the performance drops dramatically. High crystallinity refers to the optimal quality of the perovskite layer is a crucial element to enhance the performance in Sn-based inorganic PSCs. [242–245]The improvement in film quality as a result of decreased value of N_t can be seen in the EQE curve, as shown in Figure 65-c. Absorption of light in a thin film can also be affected by the defect density into the absorber layer, and we noted that EQE increases rapidly with a decrease of the perovskite defect density and acquire saturation when N_t < 1E12cm^{-3}. For our further studies, we took N_t =1E12 cm^{-3} as an optimum value of defect density of $CsSnIBr_2$ absorber.

2.2.3 Influence of interface defect density at $CsSnIBr_2$/HTL

The quality and nature of the interface are paramount to fabricate efficient solar cells, here we have varied the N_t from 10^{17} cm^{-3} to 10^{12} cm^{-3} at the $CsSnIBr_2$/HTL interface as seen in Figure 65 a-b-c. We noted an abrupt drop in the performance when N_t >10^{15}cm^{-3} and remains nearly unchanged if N_t <10^{15}cm^{-3}, this enhancement was obtained due to the reduction in defect density at $CsSnIBr_2$/HTL interface. The value of contact resistance is higher when high defect density is present, which also led to a lower fill factor. However, the J_{SC} changed insignificantly as a function of defect density, which can be manifested from the EQE graph Figure 65 -b.

Thus, we have chosen 10^{15} cm^{-3} as an optimum value for $CsSnIBr_2$/HTL interface which could delivers a PCE =18.17 %, V_{oc} = 1.29 V, J_{sc} =20.29 mA/cm^2 and FF = 69.29 %.

2.2.4 Influence of interface defect density at ETL/$CsSnIBr_2$

We continue our simulation studies with the optimization of the ETL/$CsSnIBr_2$ interface, which can further contribute to improve the performance of PSCs, as shown in Figure 65 d-e-f. If we decrease the value of N_t, the performance increases linearly, and reaches to the maximum to achieve an optimum value of N_t, beyond that value, it becomes saturates. From figure 65 e, we can set N_t =10^{14} cm^{-3} as an optimal value for ETL/$CsSnIBr_2$ interface, and using this value, a PCE of 20.35 %, with a V_{oc} of 1.35V, J_{sc} = 20.30 mA/cm^2 and FF = 74.17 % can be derived. It can be deducted that the defect density of ETL/$CsSnIBr_2$ has a strong effect on the performance due to solar irradiation passes through this interface first, thus at this interface, photo-generated carrier concentration are higher than $CsSnIBr_2$/HTL interface. The high defects density will create more recombination sites and traps, resulting in a higher recombination rate and vice versa. The investigation of the EQE as a function of defect density of the ETL/$CsSnIBr_2$ interface further supports our interpretation, a decrease of N_t leads to enhanced light absorption in the panchromatic region of 300-700 nm, contributing to the enhanced quantum efficiency.

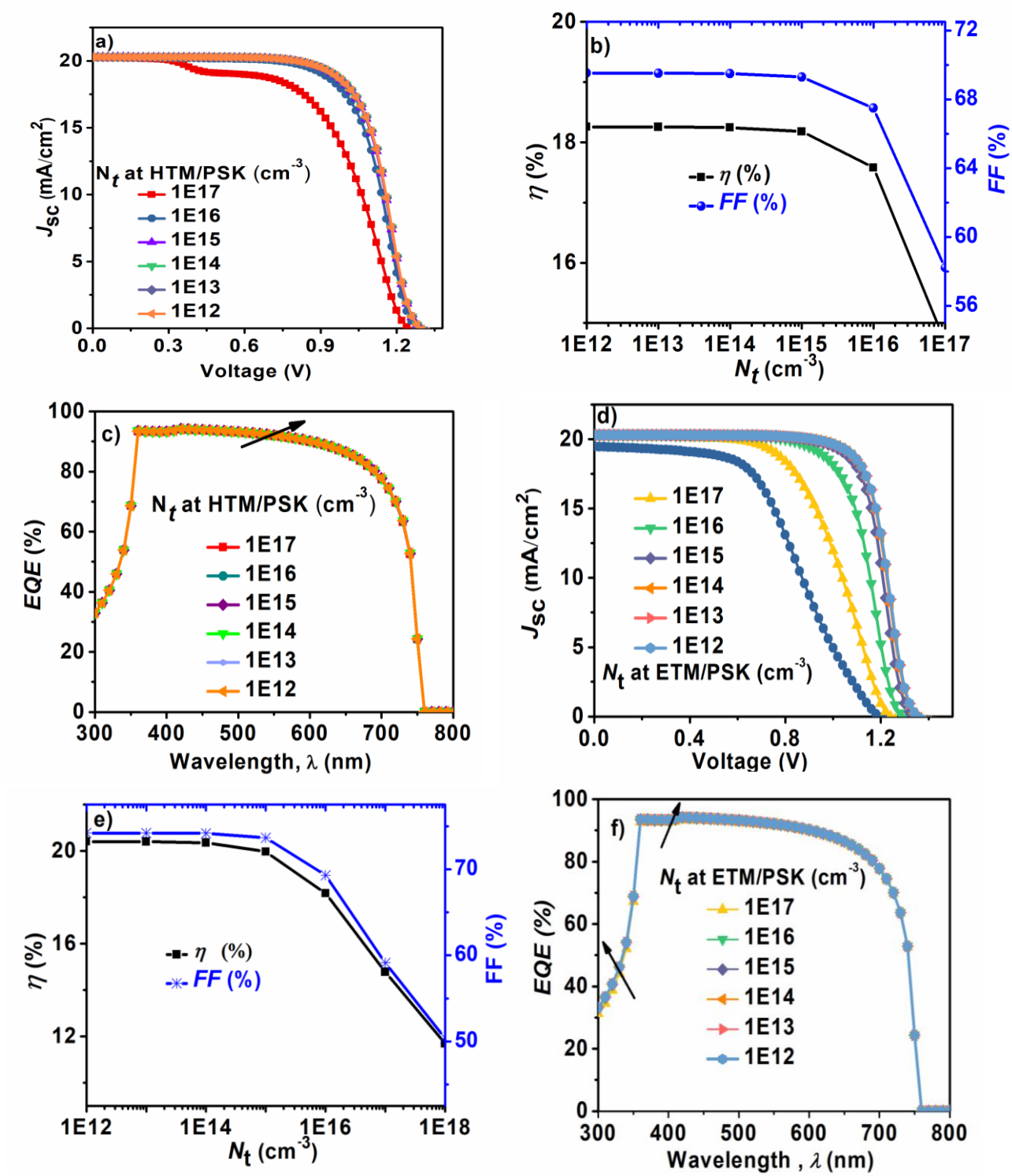

Figure 65 : Influence of defect density at $CsSnIBr_2$/HTM on a) J-V curve, (b) efficiency and fill factor and c) the external quantum efficiency and Influence of defect density at ETM/ $CsSnIBr_2$ on d) J-V curve, e) efficiency and fill factor and f) the external quantum efficiency

2.2.5 Diffusion length of the optimum device based on $CsSnIBr_2$

FTO/SnO_2/$CsSnIBr_2$/spiro-OMeTAD/Au optimized through studying the impact of defect density in $CsSnIBr_2$ and at its interfaces. The diffusion length can be

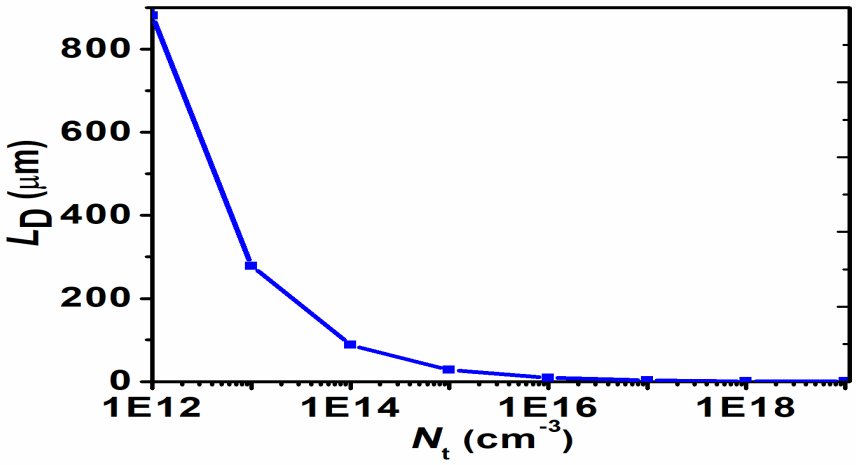

Figure 66 : *Carrier diffusion length as a function of defect density in our modelled inorganic $CsSnIBr_2$ based PSC.*

calculated by using the equation (43),(44), and (45). Figure 66 shows the diffusion length of charge carriers as a function of defect density, which can provide us a clear view about the range of the Diffusion length that should be in the case of the absorber layer and at the interfaces. By using the optimum values of defect densities derived from our optimization , 10^{12} cm^{-3} , 10^{15} cm^{-3} and 10^{14} cm^{-3} for $CsSnIBr_2$, $CsSnIBr_2$/HTL and ETL/ $CsSnIBr_2$ respectively. We can estimate a value of 278 μm as the diffusion length for the charge carriers in the absorber layer, and 27.84 μm, 88.06 μm in case of $CsSnIBr_2$/HTL and ETL/$CsSnIBr_2$ interface layers respectively. Assuming these optimum values, can theoretically deliver a PCE =20.32 %, V_{oc} =1.35 V, J_{sc} = 20.30mA/cm^2 and FF 74.17 %.

Table 14: The performance of the optimized FTO/SnO_2/IDL1/$CsSnIBr_2$/IDL2/HTLs/Au compared to the Shockley-Queisser-limit.

	PCE (%)	**V_{oc} (V)**	**J_{sc} mA/cm²**	**FF (%)**
Experimental work[225]	0.12	0.311	1.32	41
First model	0.28	1.07	1.69	15.34
Optimized model	20.32	1.35	20.30	74.17
Shockley-Queisser-limit[240]	29.90	1.37	24.05	90.77

Table 14 summarized the experimental studies that have reported, compared to our first model and the optimized model. The optimized results we found is clearly can boost the performance of Lead- free inorganic PSCs to be close to the Shockley-Queisser-

limit[240], trough new methods of fabrication such as syntheses of based materials in Pyrex-tube as reported with mixed inorganic Sn-Ge which can enhance the quality (crystallinity) of light harvest layer with low defect density,[246] also the passivation mechanism could be a helpful strategy to minimize the trap density at the interfaces of selective layers.

Conclusions

To summarize, using one-dimensional computational SCAPS software, a device structure of FTO/SnO_2/$CsPbI_2Br$/HTLs/Au was designed by selecting different organic, polymeric and inorganic types hole transport materials such as Spiro-OMeTAD, PTAA, and CuSCN, and the defect density of absorber layer was investigated suggesting a significant influence on the performance of PSCs. Tuning the valence band maximum of Spiro-OMeTAD and PTAA demonstrated competitive performance as compared to CuSCN by optimizing the VBO to be -0.41 eV and the barrier height with -0.15 eV with Shockley contact. Lead-free inorganic PSCs based on $CsSnI_{3-x}Br_x$ was also investigated. The addition of Br to substitute I in $CsSnI_3$ allows for better energy level alignment with the ETL. The quality of the absorber layer and its interface is paramount to design efficient inorganic Pb-Free PSCs that can be controlled by optimizing defect density. We put forward the design of high performance Pb-Free PSCs having the structure of FTO/SnO_2/$CsSnIBr_2$/Spiro-OMeTAD/Au, with $N_t=10^{12}$ cm^{-3} for absorber layer, and $N_t=10^{15}$ cm^{-3} in case of $CsSnIBr_2$/HTL and $N_t=10^{14}$ cm^{-3} for ETL/$CsSnIBr_2$ yielding a PCE of 20.32%. Our computational approach can pave the way to boost the performance of inorganic Pb and Pb-Free PSCs by considering suggested parameters.

.

Chapter 7: Experimental investigations of Electron transport layer, perovskite materials, and inorganic perovskite solar cells

This chapter will focus on the experimental work that has been done during this study, such as the fabrication of the selective layer, perovskite film, and the inorganic perovskite solar cell.

1 Doped SnO_2 as Electron transport layer

Regarding the work that has been done in the previous chapter regarding the conduction band offset using SnO_2 as ETL, this part of this chapter will focus on doping SnO_2 to enhance its optical proprieties as a first stage to apply it in perovskite solar cell.

We choose alkaline carbonate Cs2CO3 as a modifier for SnO_2, the preparation of layers was dived on two methods to select the best from them, the first one is mixed SnO_2:Cs_2CO_3 , the second method is bilayer SnO_2/ Cs_2CO_3.

1.1 Mixed SnO_2:Cs_2CO_3

1.1.1 Solution preparation

The SnO_2 colloidal dispersion solution (15 wt. %) was diluted by deionized water to 2.67 wt.%.The Cs_2CO_3 solutions were prepared by dissolving 0.25,0.5, 1, 1.5, and 2 mg Cs_2CO_3 in five numbered clear glass vials, respectively. Then 1 ml of deionized water was added to each bottle to form three-five Cs_2CO_3 solutions of different concentrations,0.25,0.5, 1, 1.5, and 2 mg/ml. Those vials were kept for three hours under steering conditions. To make SnO_2: Cs_2CO_3 solution, equal volume (V: V) was mixed from each vial to the SnO_2 solution.

1.1.2 SnO_2: Cs_2CO_3 film preparation

The SnO_2: Cs_2CO_3 film was prepared by spin coating the mixed solution SnO_2: Cs_2CO_3 on the cleaned substrates (4000 rpm,30 s), then these samples were annealed at different temperature 100 °C, 120 °C, 150 °C.

1.2 Bilayer SnO_2/Cs_2CO_3

1.2.1 SnO_2 film preparation

The SnO_2 film was prepared by spin-coating SnO_2 precursor solution on the cleaned substrates (5000 rpm, 30 s), then these samples were annealed at 150 °C.

1.2.2 SnO_2/Cs_2CO_3 film preparation

The SnO_2 film from the previous preparation put it to cool down, then Cs_2CO_3 was spin-coated on the top of SnO_2, then transferred to the hotplate for annealing processes at 100 °C for 10 min.

1.3 Results and discussion

1.3.1 Optical properties

It is clear from Figure *67* of optical transmittance that Cs_2CO_3 as a dopant of SnO_2 leads to increase the transmittance of SnO_2 regarding the amount of Cs_2CO_3 that added, here we can analyze that 0.25 mg/ml is the best concentration among all the concentration test for both methods.

The optical proprieties of ETLs have a significant role in the performance of PSCs. Usually, to maximize the penetration of the photons towards the active layer, the transparency of ETL is required to be over 85 % [247] in the visible wavelength, i.e., if the number of photons comes to the absorber layer, the performance will be better. It clear that both methods SnO_2/Cs_2CO_3 or SnO_2: Cs_2CO_3 lead to an increase in the transparency of SnO_2 to reach the critical value of 85 %. For that, the coming parts in this chapter will focus on using 0.25 mg /ml as the concentration of Cs_2CO_3 using second method SnO_2:Cs_2CO_3

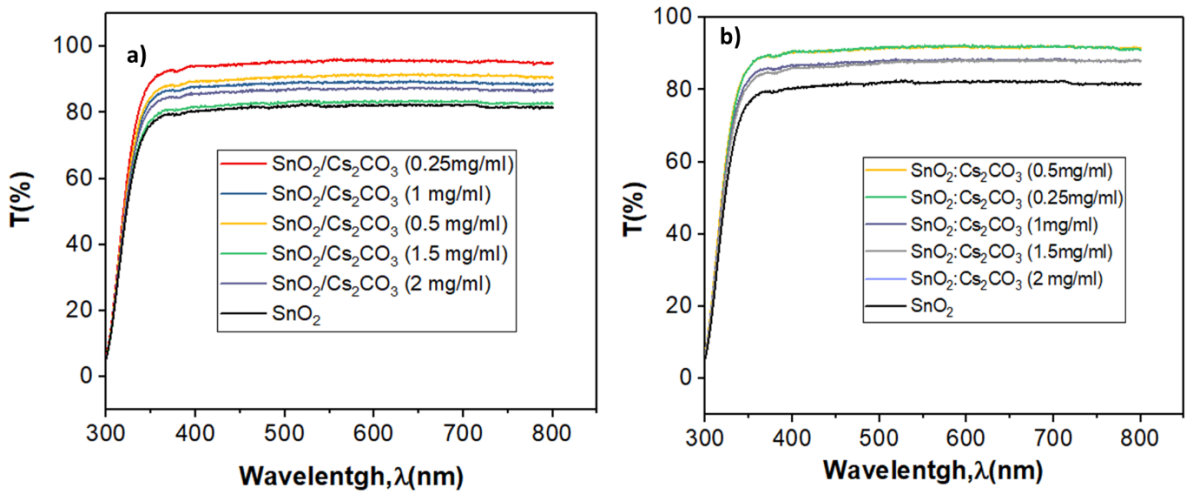

Figure 67: Optical transmittance of SnO_2 and (a) SnO_2/Cs_2CO_3 and (b) SnO_2:Cs_2CO_3

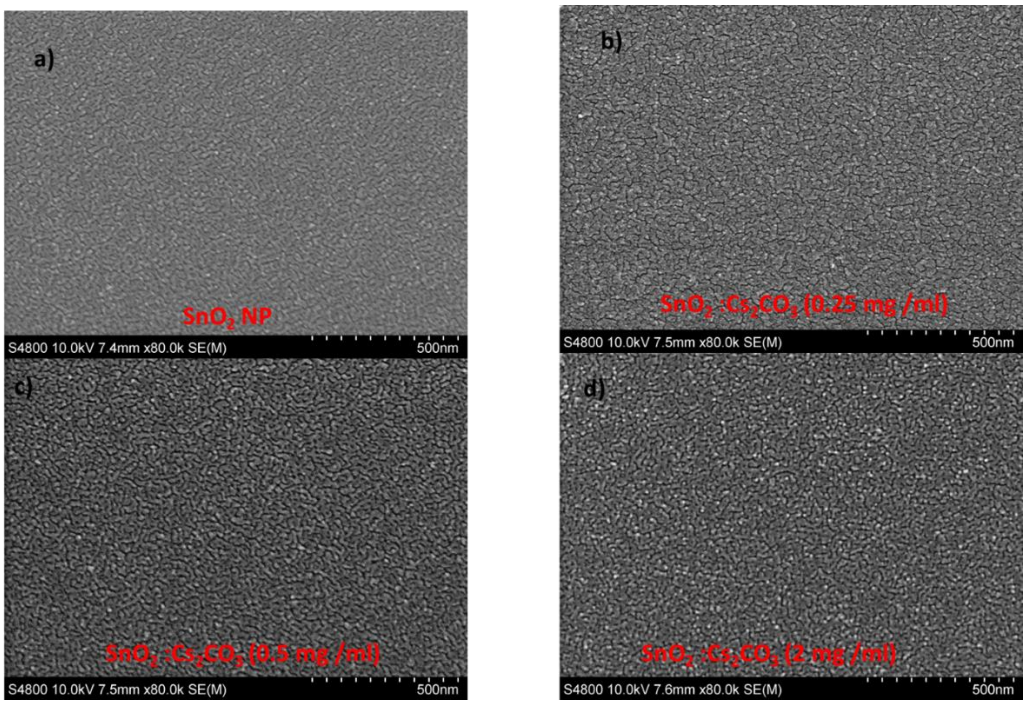

Figure 68 :Top view of SEM for .(a) SnO_2 , (b-d) different concentration of Cs_2CO_3 mixed with SnO_2

Regarding the morphology of SnO_2 compared with different amounts of Cs_2CO_3 doped SnO_2, as illustrated in Figure 68, we can analyses the quality of the surface decreased when the concentration of Cs_2CO_3 increased. 0.25 mg /ml as the concentration of Cs_2CO_3 May exhibit the best performance in the application of PSCs.

1.3.2 The effect of post-annealing temperature on optical proprieties of SnO_2: Cs_2CO_3 (0.25 mg /ml)

Figure 69 represents the T_{auc} plot band gap of SnO_2 using 150 °C as annealing temperature, and also the T_{auc} plot band gap of SnO_2: Cs_2CO_3 with different annealing temperature (110 °C,120 °C, 150 °C). The band gap of the film is calculated by using the equation below,

$$(\alpha hv)^2 = A(hv - E_g) \quad (51)$$

As shown in Figure 69, the bandgap of SnO_2 using 150°C post-annealing temperature is 3.75 eV. The incorporation of Cs_2CO_3 (0.25 mg /ml) leads to a decrease in the band gap of SnO_2 to 3.66 eV, which means the level energy of the film also is changed. The rate of decline in the band gap can be controlled by changing the post-annealing temperature as demonstrated in figure 69 b-c-d, well increasing the annealing temperature to 120 °C to give a bandgap of 3.75eV and 150 °C increase the band gap to 3.76 eV. We can agree that the annealing temperature of SnO_2: Cs_2CO_3 can manipulate the energy alignment to match better with other layers in case of the application SnO_2: Cs_2CO_3 as ETL for PSCs, and can answer the question have opened in the previous chapter about the spike and spoke for conduction band between ETL/perovskite layer.

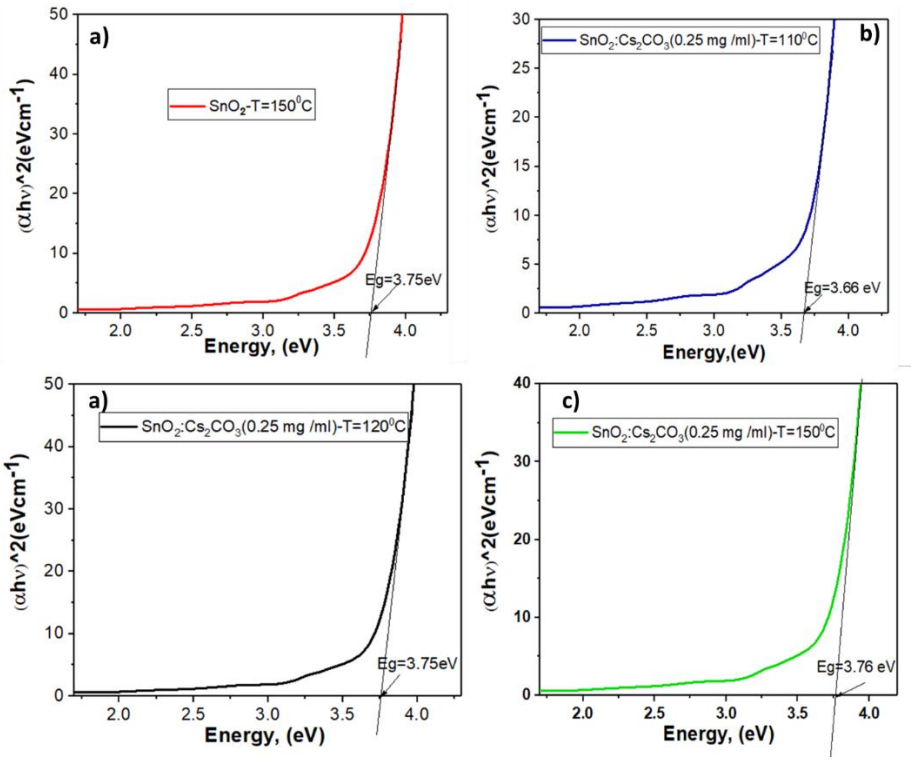

Figure 69: the Tauc plot band gap of (a) SnO2. (b-c-d) SnO_2: Cs_2CO_3 with annealing temperature 110,120 and 150 respectively

As shown in Figure *69*, the band gap of SnO_2 using 150°C post-annealing temperature is 3.75 eV. The incorporation of Cs_2CO_3 (0.25 mg /ml) leads to a decrease in the band gap of SnO_2 to 3.66 eV, which means the level energy of the film also is changed. The rate of decline in the band gap can be controlled by changing the post-annealing temperature as demonstrated in Figure *69* b-c-d, well increasing the annealing temperature to 120 °C gives a band gap of 3.75eV and 150 °C increase the band gap to 3.76 eV. We can agree that the annealing temperature of SnO_2:Cs_2CO_3 can manipulate the energy alignment to match better with other layers in case of the application SnO_2:Cs_2CO_3 as ETL for PSCs, and can answer the question have opened in the previous chapter about the spike and spoke for conduction band between ETL/perovskite layer.

2 Organic-inorganic perovskite materials

2.1 Solution preparation

2.1.1 $MAPbI_3$

The solvent engineering method was adapted to make $MAPbI_3$, MAI (1.2M), and PbI_2 (1M) was dissolved in DMSO and stirred overnight with 60 °C. The precursor solution spin-coated on the cleaned substrate by two-step method (firs step 1000 rpm for 10 s, second step 4000 rpm for 30 s), and 100 ul of C.B. dropped on the film in the last 10 s during the second step.

2.1.2 $(FAPbI_3)_{0.85}(MAPbBr_3)_{0.15}$

$(FAPbI_3)_{0.85}(MAPbBr_3)_{0.15}$ was deposited from a precursor solution containing FAI (1 M), PbI_2 (1.2 M), MABr (0.2 M), and $PbBr_2$ (0.2 M) in anhydrous DMF:DMSO 4:1 (v:v). The

perovskite solution was spin-coated in a two-step process at 1000 and 4000 rpm for 10 and 30 s, respectively. During the second step, 100 µL of chlorobenzene was used as an antisolvent and poured on the substrate 15 s before the end of the deposition process. The substrates were then annealed at 100 °C for 1 h in a glovebox.

2.1.3 $CsPbI_2Br$

$CsPbI_2Br$ was prepared by dissolving PbI_2(1 mmol) and CsBr (1mmol), in anhydrous DMSO (1mL) and stirred at 60 °C for one hour, then CsI(0.8 mmol) was added and stirred at 60 °C for another one hour, then the perovskite solution was spin-coated by two steps onto at 1500 rpm and 5000 rpm for 10 s and 30 s respectively. During the last 10 s the substrate was treated by isopropanol and transferred to hot plat using 50 °C and 150 °C for 2 min and 10 min, respectively.

2.2 Results and discussion

Colossal attention has taken the hybrid halide perovskite $MAPbI_3$ with its incredible efficiency, and $(FAPbI3)_{0.85}(MAPbBr3)_{0.15}$ is also going in the same trend as PCE exceeding 20 %. However, due to the hygroscopicity and thermally unstable the organic cation MA^+, make $MAPbI_3$ thermal volatile and sensitive to the moisture even $(FAPbI3)_{0.85}(MAPbBr3)_{0.15}$ exhibit a few improvements in case of thermal stability. Still, inorganic perovskite materials such as $CsPbI_2Br$ needs more investigation as one of the alternative inorganic perovskite light harvest that can resist the heat and moisture. Here we will try to prepare $CsPbI_2Br$ under temperature <150 °C and compare its optical proprieties with $MAPbI_3$ and $(FAPbI3)_{0.85}(MAPbBr3)_{0.15}$

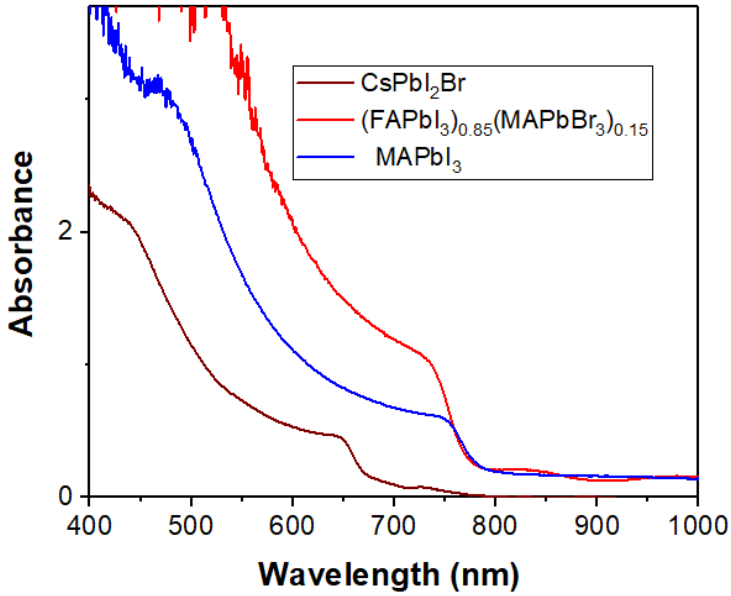

Figure 70: The UV-vis absorption spectral of $MAPbI_3$, $(FAPbI3)_{0.85}(MAPbBr3)_{0.15}$ and $CsPbI_2Br$

As plotted in the Figure *71*-b, we can notice that the band gap of $CsPbI_2Br$ about 1.90 eV is high compared to $MAPbI_3$ (1.53 eV) or mixed perovskite (1.56 eV) due to the amount of Bromide (Br) that incorporated in $CsPbI_3$.The proposed method of preparation $CsPbI_2Br$ in this work is to successfully protect the stability performance, as shown in Figure 71-a, under low

temperature, which is helpful to address the application in PSCs such as standard or flexible cells.

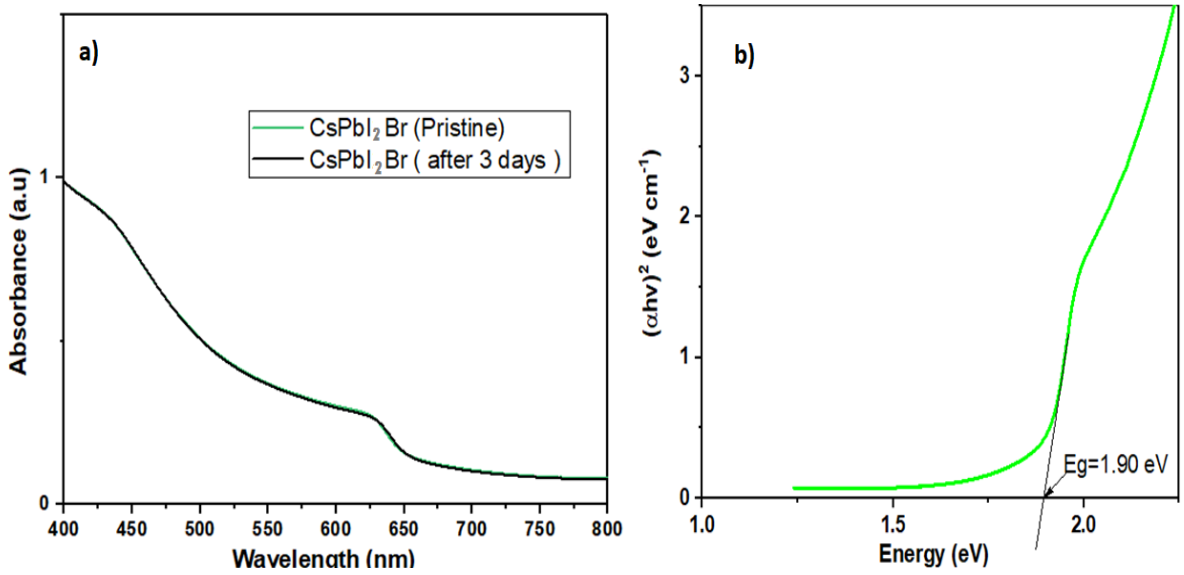

Figure 71 : (a) The stability of UV-vis absorption spectral for $CsPbI_2Br$. b)The Tauc plot band gap of $CsPbI_2Br$

The morphology structure of perovskite layer was studied by X-ray pattern as illustrated in fig *Figure 72-a*, we can notice that the grow of perovskite layer oriented with (200) and (100) direction which confirm the cubic phase as reported previously [248] demonstrated the success of our deposition method, and also we can analyze from *Figure 72-b,* the surface morphology of $CsPbI_2Br$ as prepared

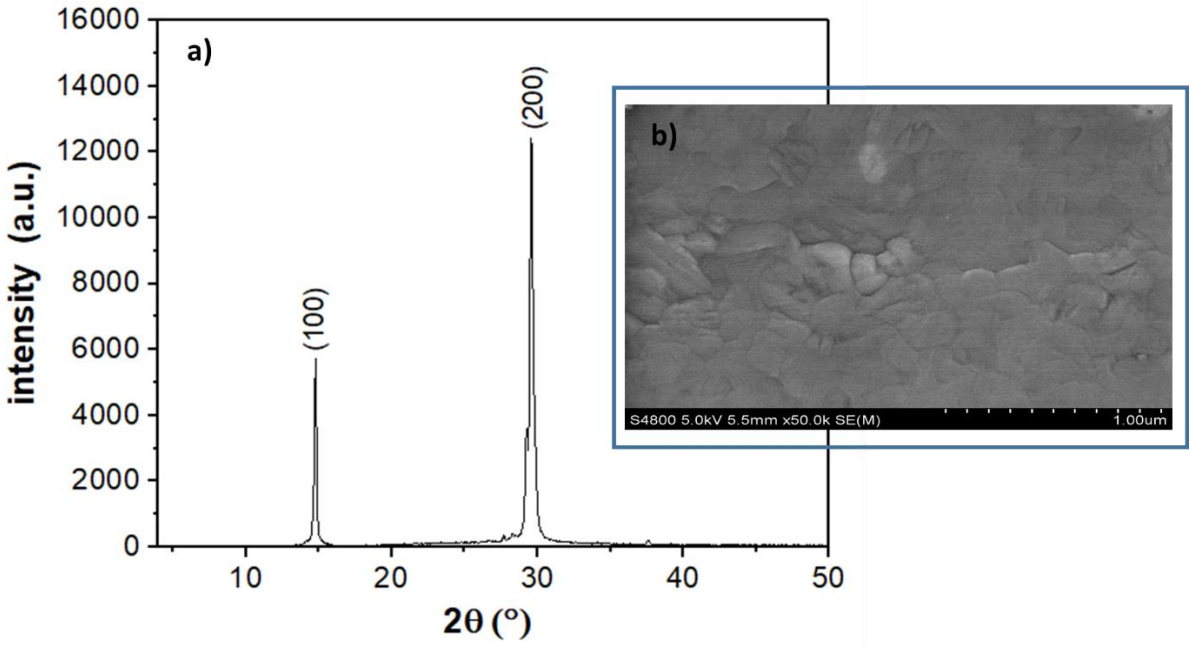

Figure 72 : (a) XRD patterns of the thin film with structural evolution. (b) Top-down SEM image of $CsPbI_2Br$

3 Fabrication and Numerical Simulation of All-inorganic P-i-N PSCs

3.1 Device fabrication

The ITO glass was cleaned by sequential ultrasonic treatment in detergent, deionized water, acetone, and isopropanol, and then treated in an ultraviolet-ozone chamber for 15 min. Then PTAA was spin-coated on ITO substrate. $CsPbI_2Br$ was prepared by dissolving PbI_2(1 mmol) and CsBr (1mmol), in anhydrous DMSO (1mL) and stirred at 60 °C for one hour, then CsI(0.8 mmol) was added and stirred at 60 °C for another one hour the perovskite solution was then spin-coated by two steps onto ITO/PCBM at 1500 rpm and 5000 rpm for 10 s and 30 s respectively. During the last 10 s the substrate was treated by isopropanol and transferred to hot plat using 50 °C and 150 °C for 2 min and 10 min, respectively. The PCBM solution in (CB). Was spin-coated on the perovskite film. Finally, the Ag as back contact was evaporated.

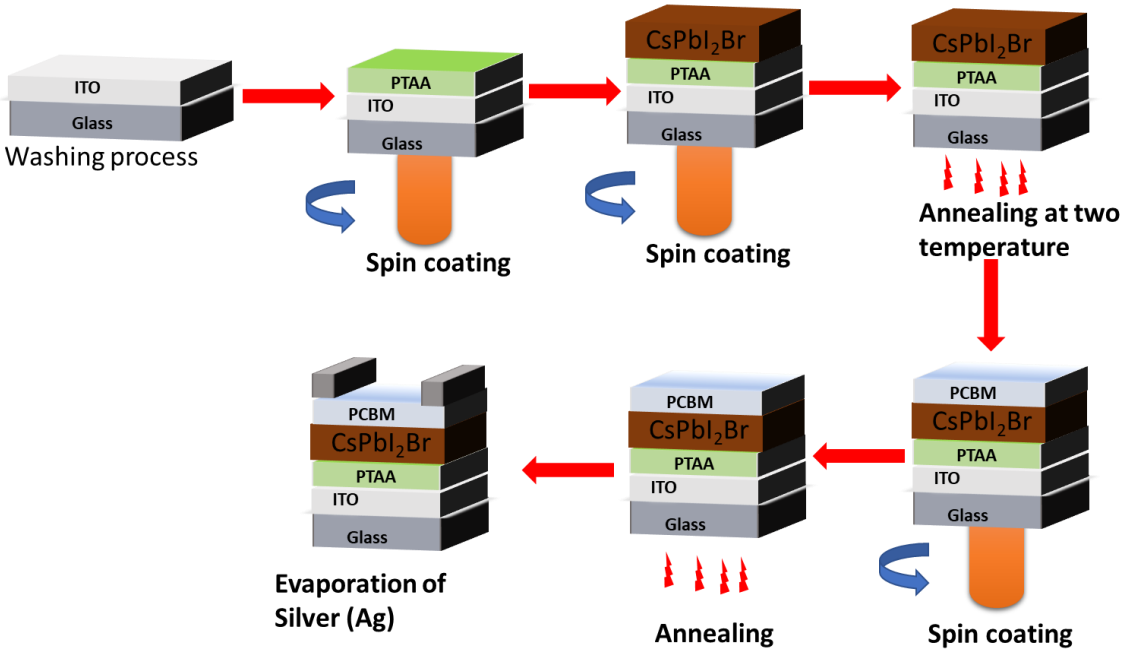

Figure 73: Schematic view of the process fabrication of P-i-N PSCs based on $CsPbI_2Br$

3.2 Device simulation

The Solar cell capacitance simulator (SCAPS) version. 3.3.07 [167] was used as a simulation platform, with the parameters sketched in Table *15*:

Based on the Poisson equation(39), and the continuity equations for electrons(40) and holes (41)

$$\frac{d}{dx}\left(\varepsilon(x)\frac{d\Psi}{dx}\right) = q[\,p(x) - n(x) + N_D^+(x) - N_A^-(x) + p_t(x) - n_t(x)\,] \quad (39)$$

$$\frac{1}{j}\frac{\mathrm{d}J_p}{\mathrm{d}x} + R_p(x) - G(x) = 0 \quad (40)$$

$$-\frac{1}{j}\frac{\mathrm{d}J_n}{\mathrm{d}x} + R_n(x) - G(x) = 0 \qquad (41)$$

Here, ε the permittivity and q the charge of electron, Ψ is the electrostatic potential and *n* the free electrons, *p* free holes, n_t trapped electrons, p_t trapped holes, N_{D+} the ionized donor-like doping and N_{A-} the ionized acceptor-like doping concentrations, Rn(x), Rp(x) are electrons and holes recombination rate, G(x) is the generation rate, J_n and J_p are respectively, the electron and hole current densities.

Here, N_A and N_D denote acceptor and donor densities, ε_r is relative permittivity, χ is electron affinity, E_g is the band gap energy, μ_n and μ_p are mobilities of electron and hole, and N_t is defect density.

Computational studies were performed on a planar PSCs with an architecture of ITO/PTAA/interface layer 1(IL1) /$CsPbI_2Br$ /interface layer2(IL2)/PCBM/Ag. AM 1.5G solar illumination of 100 mW/cm^2 was used for simulative studies.

Table 15: Parameters Used in the SCAPS Simulation of Pb based inorganic PSCs

Parameter	**PTAA**	**IL1**	**$CsPbI_2Br$**	**IL2**	**PCBM**
thickness (nm)	150	10	500	10	90
E_g (eV)	2.95 [229]	1.86 [228]	1.86 [228]	1.86 [228]	2
X	2.3 [229]	3.8 [228]	3.8 [228]	3.8 [228]	4
Ɛr	3.5 [230]	8.6	8.6	8.6	3.9
***N*c (1/cm^3)**	2.2E18	2.2E18	2.2E18	2.2E18	2.2E18
***N*v (1/cm^3)**	1.8E19	1.8E19	1.8E19	1.8E19	1.8E19
μ_n(cm^2/Vs)	1E-4 [193]	200 [231]	200 [231]	200 [231]	1E-2
μ_p (cm^2/Vs)	1E-4	200	200	200	1E-2
N_A (1/cm^3)	1E18	--	--	--	-
$N_{.D.}$ (1/cm^3)	_	1E15	1E15	1E15	1E16
N_t(1/cm^3)	1E15	3.64E16	3.64E15[213]	3.64E16	1E15

3.3 Results and discussion

The results of experimental ITO/PTAA/PKS/PCBM/Ag showed in Figure 74-a ,demonstrated an efficiency of 6.67 % , V_{oc} of 0 .99 V , J_{sc} =12.64 mA/cm2 and FF=53.11 %. The stability of these results after seven days with storage in the glovebox are almost the same values, which can demonstrate the power of **our method to make low-temperature all-inorganic $CsPbI_2Br$ PSCs.**

In the line to figure out the physic parameters that may be responsible for low performance in our cell, we perform a simulation study for the same cell is made in the experimental part as illustrated in Figure 74-b illustrate the first simulation results are near to the experimental values which mean that can use this model to make drift-diffusion simulation to boost and address the problems of these kinds of PSCs by optimizing macroscopic parameters and applying new adequate selective layers.

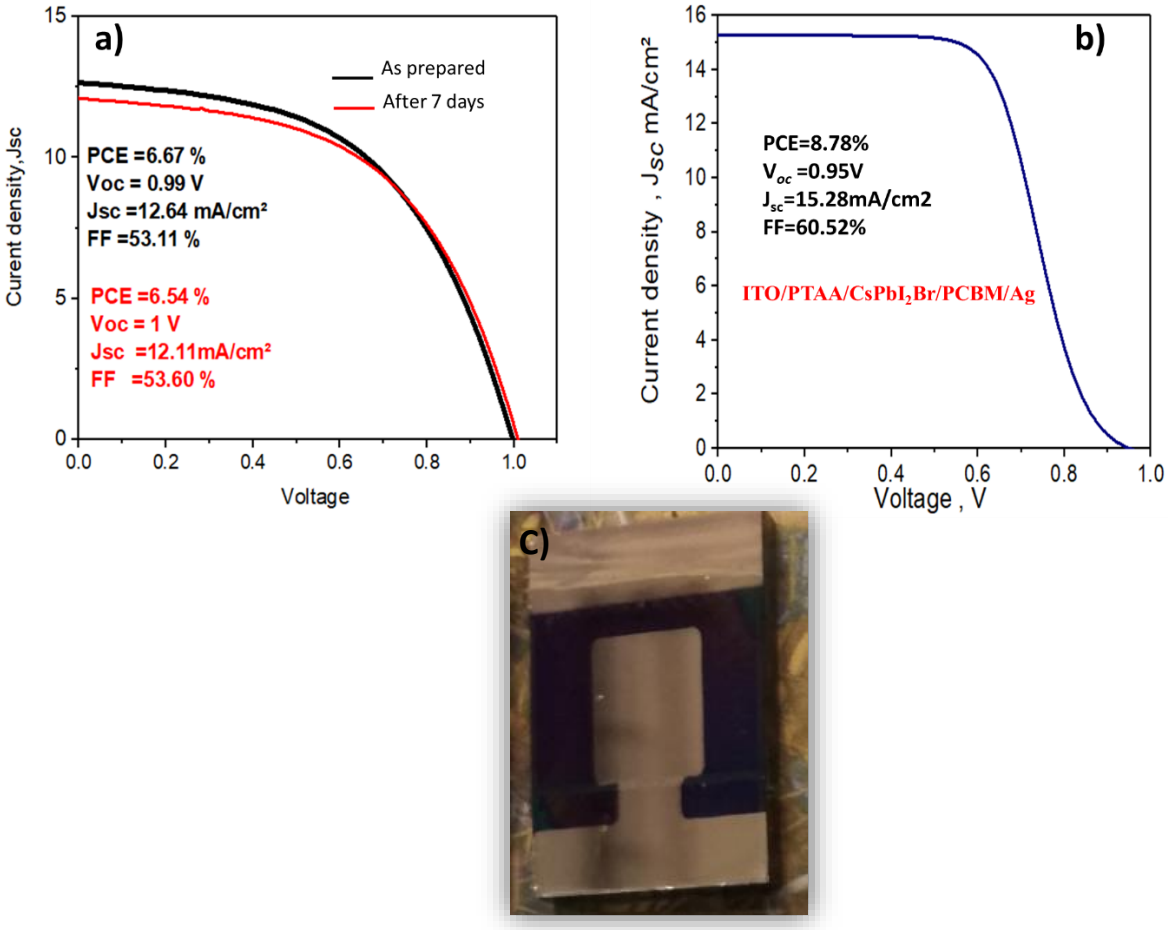

Figure 74: (a) J-V curve of the experimental cell as prepared and after seven days. (b) J-V curve of Simulated PSCs. (c) Experimental fabrication of PSCs

Conclusion

This chapter showed the benefit of doping ETLs such as SnO_2 to change its optoelectronic properties for better matching in PSCs . The preparation of $CsPbI_2B$ under low temperatures could be an effective strategy to boost the performance of p-i-n inorganic PSCs for its application in tandem PSCs. Using the drift-diffusion model may lead to figure out the macroscopic parameters are responsible for the low performance, as discussed in the previous chapters in the case of organic-inorganic PSCs.

Conclusion and Recommendations

i. Conclusion

At the close of chapters 1-3, a vivid description of perovskite solar cells is made by a general introduction, basic physic of semiconductor, structure of perovskite materials, work principal, and divers structures of perovskite solar cell were discussed. Also, the types of electron transport layer and hole transport layers have taken place. Finally, the work methodology based on Numerical simulation using SCAPS-tool and the preparation methods of perovskite solar cells were explained.

In chapter 4, the performance analysis of $MAPbI_3$ based perovskite solar cells employing diverse charge selective contacts: Simulation study is investigated by SCAPS software. The performance of perovskite solar cells based on $MAPbI_3$ can be close to the theoretical limit by adjusting low-temperature electron transport layer and stable hole transport layer using low cost back contact metal, and the optimized perovskite solar cell can reach an efficiency of 26.74%.

Chapter 5 discussed the energy level engineering of charge selective contact and halide perovskite by modulating band offset: Mechanistic insights. The advantage of engineering the band offset analyzed using $(FAPbI_3)_{0.85}(MAPbBr_3)_{0.15}$ as a light harvest, the optimized cell can obtain 26.56 %.

Chapter 6 carried out on the unraveling of the theoretical window for high-performance inorganic perovskite solar cells. For the first time, the inorganic perovskite solar cell based on $CsPbI_2Br$ and Pb-free $CsSnI_{3-x}Br_x$ have simulated through SCAPS software. Inspiring performance obtained of this alternative inorganic solar cell by optimizing many parameters such as the defect density in bulk absorber material or at the interface of layers. 17.77 % and 20.35% was reached using our optimized cells for $CsPbI_2Br$ and $CsSnIBr_2$ respectively.

Finally, in chapter 7, the proposed fabrication of SnO_2: Cs_2CO_3 as an alternative electron transport layer for perovskite solar cells is made following low-temperature deposition. Diverse perovskite materials are fabricated, such as $MAPbI_3$, $(FAPbI_3)_{0.85}(MAPbBr_3)_{0.15}$, $CsPbI_2Br$ through solvent engineering method. The fabrication of P-i-N perovskite solar cells based on $CsPbI_2Br$ is made in parallel with its numerical simulation using SCAPS software.

The physical device model approach is an ‘’anatomy’’ of perovskite solar cell to zoom deeply on the macroscopic parameters that pretended the perovskite solar cell to reach the Shockley-Queisser-Limit efficiency by the inexpensive way in terms of cost and time. This research study is a lamp to light the road of the experimental community for efficient, versatile structural in organic-inorganic perovskite solar cells combining Drift-Diffusion simulation and experimental studies.

ii. Recommendations

As the outset of this thesis, we can draw a few recommendations that will be helpful for our future work:

- As numerically demonstrated in chapter 4, a new inorganic whole transport layer based on Cu, such as CuSCN, $CuSbS_2$, and Cu_2O, should be made to increase the stability of PSCs.
- As discussed in chapter 5, the misalignment of level energy at ETL/perovskite is a crucial parameter to increase the efficiency of PSCs. A logical next step should be a focus on designing new materials to full this matter.
- New approach preparation of $CsPbI_2Br$ should figure out to stabilize this alternative inorganic material, using new element doping to make $CsPb_{1-x}M_xI_2Br$ through Density functional theory (DFT), Drift-diffusion simulation and experimental studies could be a suitable combination to answer the issue of efficiency and stability of this type of PSCs.
- Eco-friendly PSCs based on Pb-free light harvest is a mandatory line to make the balance between the efficiency, protection of the environment, and stability.
- Boost the efficiency of P-i-N based inorganic PSCs is a helpful way to understand the macroscopic parameters that lower the performance of this type of PSCs, which will be our next work.

References

[1] B. Obama, The irreversible momentum of clean energy, Science. 355 (2017) 126–129. doi:10.1126/science.aam6284.

[2] Pdxs. Dissertations, T. Dissertations, J. Keith Walton, Thin Film Group II-VI Solar Cells Based on Band-Offsets, (2010). doi:10.15760/etd.435.

[3] J.H. Scaff, H.C. Theuerer, E.E. Schumacher, P-type and N-type Silicon and the Formation of the Photovoltaic Barrier in Silicon Indots, JOM. 1 (1949) 383–388. doi:10.1007/bf03377436.

[4] M.A. Green, Tracking solar cell conversion efficiency, Nature Reviews Physics. 2 (2020) 172–173. doi:10.1038/s42254-020-0163-y.

[5] NREL, Best Research-Cell Efficiencies: Rev. 04-06-2020, (2020). https://www.nrel.gov/pv/cell-efficiency.HTLl.

[6] A. Abrusci, S.D. Stranks, P. Docampo, H.L. Yip, A.K.Y. Jen, H.J. Snaith, High-performance perovskite-polymer hybrid solar cells via electronic coupling with fullerene monolayers, Nano Letters. 13 (2013) 3124–3128. doi:10.1021/nl401044q.

[7] D.B. Mitzi, S. Wang, C.A. Feild, C.A. Chess, A.M. Guloy, Conducting layered organic-inorganic halides containing 〈110〉-oriented perovskite sheets, Science. 267 (1995) 1473–1476. doi:10.1126/science.267.5203.1473.

[8] H. Kim, C. Lee, J. Im, K. Lee, T.M.-S. reports, undefined 2012, Lead iodide perovskite sensitized all-solid-state submicron thin film mesoscopic solar cell with efficiency exceeding 9%, Nature.Com. (n.d.). https://www.nature.com/articles/srep00591?page=4 (accessed May 16, 2020).

[9] A. Kojima, K. Teshima, Y. Shirai, T. Miyasaka, Organometal halide perovskites as visible-light sensitizers for photovoltaic cells, Journal of the American Chemical Society. 131 (2009) 6050–6051.

[10] T. Liu, K. Chen, Q. Hu, R. Zhu, Q. Gong, Inverted Perovskite Solar Cells: Progresses and Perspectives, Advanced Energy Materials. 6 (2016). doi:10.1002/aenm.201600457.

[11] F. Guo, S. Qiu, J. Hu, H. Wang, B. Cai, J. Li, X. Yuan, X. Liu, K. Forberich, C.J. Brabec, Y. Mai, A Generalized Crystallization Protocol for Scalable Deposition of High-Quality Perovskite Thin Films for Photovoltaic Applications, Advanced Science. 6 (2019) 1901067. doi:10.1002/advs.201901067.

[12] M. Saliba, T. Matsui, K. Domanski, J.Y. Seo, A. Ummadisingu, S.M. Zakeeruddin, J.P. Correa-Baena, W.R. Tress, A. Abate, A. Hagfeldt, M. Grätzel, Incorporation of rubidium cations into perovskite solar cells improves photovoltaic performance, Science. 354 (2016) 206–209. doi:10.1126/science.aah5557.

[13] G. Grancini, C. Roldán-Carmona, I. Zimmermann, E. Mosconi, X. Lee, D. Martineau, S. Narbey, F. Oswald, F. De Angelis, M. Graetzel, M.K. Nazeeruddin, One-Year stable perovskite solar cells by 2D/3D interface engineering, Nature Communications. 8 (2017) 1–8. doi:10.1038/ncomms15684.

[14] Q. An, Q. Sun, A. Weu, D. Becker-Koch, F. Paulus, S. Arndt, F. Stuck, A.S.K. Hashmi, N. Tessler, Y. Vaynzof, Enhancing the Open-Circuit Voltage of Perovskite Solar Cells

by up to 120 mV Using Π-Extended Phosphoniumfluorene Electrolytes as Hole Blocking Layers, Advanced Energy Materials. 9 (2019). doi:10.1002/aenm.201901257.

[15] M. Stolterfoht, C.M. Wolff, J.A. Márquez, S. Zhang, C.J. Hages, D. Rothhardt, S. Albrecht, P.L. Burn, P. Meredith, T. Unold, D. Neher, Visualization and suppression of interfacial recombination for high-efficiency large-area pin perovskite solar cells, Nature Energy. 3 (2018) 847–854. doi:10.1038/s41560-018-0219-8.

[16] T. Minemoto, M. Murata, Theoretical analysis on effect of band offsets in perovskite solar cells, Solar Energy Materials and Solar Cells. 133 (2015) 8–14. doi:10.1016/j.solmat.2014.10.036.

[17] D. Li, L. Song, Y. Chen, W. Huang, Modeling Thin Film Solar Cells: From Organic to Perovskite, Advanced Science. 7 (2020) 1901397. doi:10.1002/advs.201901397.

[18] J.P. Correa-Baena, M. Saliba, T. Buonassisi, M. Grätzel, A. Abate, W. Tress, A. Hagfeldt, Promises and challenges of perovskite solar cells, Science. 358 (2017) 739–744. doi:10.1126/science.aam6323.

[19] D.A. Neamen, Semiconductor Physics and Devices Basic Principles Fourth Edition, 2012. www.mhhe.com (accessed May 25, 2020).

[20] L. Bruno, 済無No Title No Title, 2019. doi:10.1017/CBO9781107415324.004.

[21] A. Einstein, Über einen die Erzeugung und Verwandlung des Lichtes betreffenden heuristischen Gesichtspunkt, Annalen Der Physik. 322 (1905) 132–148. doi:10.1002/andp.19053220607.

[22] W. Shockley, W.T. Read, Statistics of the recombinations of holes and electrons, Physical Review. 87 (1952) 835–842. doi:10.1103/PhysRev.87.835.

[23] R.N. Hall, Electron-hole recombination in germanium [21], Physical Review. 87 (1952) 387. doi:10.1103/PhysRev.87.387.

[24] V.M. Goldschmidt, Die Gesetze der Krystallochemie, Die Naturwissenschaften. 14 (1926) 477–485. doi:10.1007/BF01507527.

[25] W. Travis, E.N.K. Glover, H. Bronstein, D.O. Scanlon, R.G. Palgrave, On the application of the tolerance factor to inorganic and hybrid halide perovskites: A revised system, Chemical Science. 7 (2016) 4548–4556. doi:10.1039/c5sc04845a.

[26] Z. Li, M. Yang, J.S. Park, S.H. Wei, J.J. Berry, K. Zhu, Stabilizing Perovskite Structures by Tuning Tolerance Factor: Formation of Formamidinium and Cesium Lead Iodide Solid-State Alloys, Chemistry of Materials. 28 (2016) 284–292. doi:10.1021/acs.chemmater.5b04107.

[27] V.G.- Naturwissenschaften, undefined 1926, The laws of crystal chemistry, (n.d.).

[28] Z.H. Bakr, Q. Wali, A. Fakharuddin, L. Schmidt-Mende, T.M. Brown, R. Jose, Advances in hole transport materials engineering for stable and efficient perovskite solar cells, Nano Energy. 34 (2017) 271–305. doi:10.1016/j.nanoen.2017.02.025.

[29] W.S. Yang, J.H. Noh, N.J. Jeon, Y.C. Kim, S. Ryu, J. Seo, S. Il Seok, High-performance photovoltaic perovskite layers fabricated through intramolecular exchange, Science. 348 (2015) 1234–1237. doi:10.1126/science.aaa9272.

[30] N.J. Jeon, J.H. Noh, W.S. Yang, Y.C. Kim, S. Ryu, J. Seo, S. Il Seok, Compositional engineering of perovskite materials for high-performance solar cells, Nature. 517 (2015) 476–480. doi:10.1038/nature14133.

[31] X. Zheng, B. Chen, J. Dai, Y. Fang, Y. Bai, Y. Lin, H. Wei, X.C. Zeng, J. Huang, Defect passivation in hybrid perovskite solar cells using quaternary ammonium halide anions and cations, Nature Energy. 2 (2017) 1–9. doi:10.1038/nenergy.2017.102.

[32] Q. Tai, J. Cao, T. Wang, F. Yan, Recent advances toward efficient and stable tin-based perovskite solar cells, EcoMat. 1 (2019). doi:10.1002/eom2.12004.

[33] S.F. Hoefler, G. Trimmel, T. Rath, Progress on lead-free metal halide perovskites for photovoltaic applications: a review, Monatshefte Fur Chemie. 148 (2017) 795–826. doi:10.1007/s00706-017-1933-9.

[34] N. Pellet, P. Gao, G. Gregori, T.-Y. Yang, M.K. Nazeeruddin, J. Maier, M. Grätzel, Mixed-Organic-Cation Perovskite Photovoltaics for Enhanced Solar-Light Harvesting, Angewandte Chemie International Edition. 53 (2014) 3151–3157. doi:10.1002/anie.201309361.

[35] Y. Ogomi, A. Morita, S. Tsukamoto, T. Saitho, N. Fujikawa, Q. Shen, T. Toyoda, K. Yoshino, S.S. Pandey, T. Ma, S. Hayase, CH3NH3SnxPb(1-x)I3 perovskite solar cells covering up to 1060 nm, Journal of Physical Chemistry Letters. 5 (2014) 1004–1011. doi:10.1021/jz5002117.

[36] L. Protesescu, S. Yakunin, M.I. Bodnarchuk, F. Krieg, R. Caputo, C.H. Hendon, R.X. Yang, A. Walsh, M. V. Kovalenko, Nanocrystals of Cesium Lead Halide Perovskites (CsPbX3, X = Cl, Br, and I): Novel Optoelectronic Materials Showing Bright Emission with Wide Color Gamut, Nano Letters. 15 (2015) 3692–3696. doi:10.1021/nl5048779.

[37] B. Conings, J. Drijkoningen, N. Gauquelin, A. Babayigit, J. D'Haen, L. D'Olieslaeger, A. Ethirajan, J. Verbeeck, J. Manca, E. Mosconi, F. De Angelis, H.G. Boyen, Intrinsic Thermal Instability of Methylammonium Lead Trihalide Perovskite, Advanced Energy Materials. 5 (2015). doi:10.1002/aenm.201500477.

[38] G.E. Eperon, S.D. Stranks, C. Menelaou, M.B. Johnston, L.M. Herz, H.J. Snaith, Formamidinium lead trihalide: A broadly tunable perovskite for efficient planar heterojunction solar cells, Energy and Environmental Science. 7 (2014) 982–988. doi:10.1039/c3ee43822h.

[39] J.H. Noh, S.H. Im, J.H. Heo, T.N. Mandal, S. Il Seok, Chemical management for colorful, efficient, and stable inorganic-organic hybrid nanostructured solar cells, Nano Letters. 13 (2013) 1764–1769. doi:10.1021/nl400349b.

[40] N.J. Jeon, H. Noh, W.S. Yang, Y.C. Kim, S. Ryu, J. Seo, S. Il Seok, Compositional engineering of perovskite materials for high-performance solar cells, Nature.Com. (2014). doi:10.1038/nature14133.

[41] Y. Reyna, M. Salado, S. Kazim, A. Pérez-Tomas, S. Ahmad, M. Lira-Cantu, Performance and stability of mixed FAPbI3(0.85)MAPbBr3(0.15) halide perovskite solar cells under outdoor conditions and the effect of low light irradiation, Nano Energy. 30 (2016) 570–579. doi:10.1016/j.nanoen.2016.10.053.

[42] H. Tang, H. Berger, P.E. Schmid, F. Lévy, G. Burri, Photoluminescence in TiO2 anatase single crystals, Solid State Communications. 87 (1993) 847–850. doi:10.1016/0038-1098(93)90427-O.

[43] J. Pascual, J. Camassel, H. Mathieu, Fine structure in the intrinsic absorption edge of TiO2, Physical Review B. 18 (1978) 5606–5614. doi:10.1103/PhysRevB.18.5606.

[44] L.Q. Jiang, Y. Qiu, L. Lin, L. Jiang, Y. Yu, Modeling and analysis of HTL-free perovskite solar cells based on ZnO electron transport layer New solar materials View project Perovskites View project Modeling and analysis of HTL-free perovskite solar cells based on ZnO electron transport layer, (2017). doi:10.1016/j.spmi.2017.02.028.

[45] D. Bi, G. Boschloo, S. Schwarzmüller, L. Yang, E.M.J. Johansson, A. Hagfeldt, Efficient and stable CH 3 NH 3 PbI 3-sensitized ZnO nanorod array solid-state solar cells, (n.d.). doi:10.1039/c3nr01542d.

[46] K. Mahmood, B.S. Swain, A. Amassian, 16.1% Efficient Hysteresis-Free Mesostructured Perovskite Solar Cells Based on Synergistically Improved ZnO Nanorod Arrays, Advanced Energy Materials. 5 (2015). doi:10.1002/aenm.201500568.

[47] W.Q. Wu, D. Chen, R.A. Caruso, Y.B. Cheng, Recent progress in hybrid perovskite solar cells based on n-type materials, Journal of Materials Chemistry A. 5 (2017) 10092–10109. doi:10.1039/c7ta02376f.

[48] B. Thomas, B. Skariah, Spray deposited Mg-doped SnO2 thin film LPG sensor: XPS and EDX analysis in relation to deposition temperature and doping, Journal of Alloys and Compounds. 625 (2015) 231–240. doi:10.1016/j.jallcom.2014.11.092.

[49] W. Ke, G. Fang, Q. Liu, L. Xiong, P. Qin, H. Tao, J. Wang, H. Lei, B. Li, J. Wan, G. Yang, Y. Yan, Low-Temperature Solution-Processed Tin Oxide as an Alternative Electron Transporting Layer for Efficient Perovskite Solar Cells, Journal of the American Chemical Society. 137 (2015) 6730–6733. doi:10.1021/jacs.5b01994.

[50] Q. Dong, Y. Shi, K. Wang, Y. Li, S. Wang, H. Zhang, Y. Xing, Y. Du, X. Bai, T. Ma, Insight into perovskite solar cells based on SnO<inf>2</inf> compact electron-selective layer, Journal of Physical Chemistry C. 119 (2015) 10212–10217. doi:10.1021/acs.jpcc.5b00541.

[51] N.J. Jeon, H. Na, E.H. Jung, T.Y. Yang, Y.G. Lee, G. Kim, H.W. Shin, S. Il Seok, J. Lee, J. Seo, A fluorene-terminated hole-transporting material for highly efficient and stable perovskite solar cells, Nature Energy. 3 (2018) 682–689. doi:10.1038/s41560-018-0200-6.

[52] A. Bera, Fast Crystallization and improved Stability of Perovskite Solar Cells with Zn 2 SnO 4 Electron Transporting Layer: Interface Matters Item Type Article Citation Fast Crystallization and improved Stability of Perovskite Solar Cells with Zn 2 SnO 4 Electron Transporting Layer: Interface Matters 2015 ACS Applied Materials & Interfaces, (n.d.). doi:10.1021/acsami.5b09182.

[53] S. Mali, C. Shim, H. Kim, C.H.-J. of M.C. A, undefined 2016, Reduced graphene oxide (rGO) grafted zinc stannate (Zn 2 SnO 4) nanofiber scaffolds for highly efficient mixed-halide perovskite solar cells, Pubs.Rsc.Org. (n.d.). https://pubs.rsc.org/en/content/articleHTLl/2016/ta/c6ta04726b (accessed October 31, 2019).

[54] P. Docampo, J. Ball, M. Darwich, G.E.-… communications, undefined 2013, Efficient organometal trihalide perovskite planar-heterojunction solar cells on flexible polymer substrates, Nature.Com. (n.d.). https://www.nature.com/articles/ncomms3761 (accessed November 12, 2019).

[55] H. Yoon, S. Kang, J. Lee, M.C.-E.& E. Science, undefined 2016, Hysteresis-free low-temperature-processed planar perovskite solar cells with 19.1% efficiency, Pubs.Rsc.Org. (n.d.). https://pubs.rsc.org/en/content/articleHTLl/2016/ee/c6ee01037g (accessed November 12, 2019).

[56] J. Huang, Z. Gu, L. Zuo, T. Ye, H.C.-S. Energy, undefined 2016, Morphology control of planar heterojunction perovskite solar cells with fluorinated PDI films as organic electron transport layer, Elsevier. (n.d.). https://www.sciencedirect.com/science/article/pii/S0038092X16300421 (accessed November 12, 2019).

[57] Y. Qing, New Generation Perovskite Solar Cells with Solution-Processed Amino-substituted Perylene Diimide Derivative as Electron-Transport Layer, Journal of Materials Chemistry A. 22 (2016) 8724–8733. doi:10.1039/C6TA03119F.

[58] Y. Shao, Y. Yuan, J. Huang, Correlation of energy disorder and open-circuit voltage in hybrid perovskite solar cells, Nature Energy. 1 (2016). doi:10.1038/nenergy.2015.1.

[59] Y. Bai, Q. Dong, Y. Shao, Y. Deng, Q. Wang, L. Shen, D. Wang, W. Wei, J. Huang, Enhancing stability and efficiency of perovskite solar cells with crosslinkable silane-functionalized and doped fullerene, Nature Communications. 7 (2016). doi:10.1038/ncomms12806.

[60] H.-S. Kim, C.-R. Lee, J.-H. Im, K.-B. Lee, T. Moehl, A. Marchioro, S.-J. Moon, R. Humphry-Baker, J.-H. Yum, J.E. Moser, M. Grätzel, N.-G. Park, Lead Iodide Perovskite Sensitized All-Solid-State Submicron Thin Film Mesoscopic Solar Cell with Efficiency Exceeding 9%, Scientific Reports. 2 (2012) 591. doi:10.1038/srep00591.

[61] T. Leijtens, J. Lim, J. Teuscher, T. Park, H.J. Snaith, Charge Density Dependent Mobility of Organic Hole-Transporters and Mesoporous TiO_2 Determined by Transient Mobility Spectroscopy: Implications to Dye-Sensitized and Organic Solar Cells, Advanced Materials. 25 (2013) 3227–3233. doi:10.1002/adma.201300947.

[62] M.T. Dang, L. Hirsch, G. Wantz, P3HT:PCBM, Best Seller in Polymer Photovoltaic Research, Advanced Materials. 23 (2011) 3597–3602. doi:10.1002/adma.201100792.

[63] S.N. Habisreutinger, T. Leijtens, G.E. Eperon, S.D. Stranks, R.J. Nicholas, H.J. Snaith, Carbon Nanotube/Polymer Composites as a Highly Stable Hole Collection Layer in Perovskite Solar Cells, Nano Letters. 14 (2014) 5561–5568. doi:10.1021/nl501982b.

[64] H.A. Abbas, R. Kottokkaran, B. Ganapathy, M. Samiee, L. Zhang, A. Kitahara, M. Noack, V.L. Dalal, High efficiency sequentially vapor grown n-i-p $CH_3NH_3PbI_3$ perovskite solar cells with undoped P3HT as p-type heterojunction layer, APL Materials. 3 (2015) 016105. doi:10.1063/1.4905932.

[65] G. Namkoong, P. Boland, K. Lee, J. Dean, Design of organic tandem solar cells using PCPDTBT:PC61BM and P3HT:PC71BM, Journal of Applied Physics. 107 (2010) 124515. doi:10.1063/1.3448271.

[66] J.H. Heo, S.H. Im, J.H. Noh, T.N. Mandal, C.-S. Lim, J.A. Chang, Y.H. Lee, H. Kim, A. Sarkar, M.K. Nazeeruddin, M. Grätzel, S. Il Seok, Efficient inorganic–organic hybrid heterojunction solar cells containing perovskite compound and polymeric hole conductors, Nature Photonics. 7 (2013) 486–491. doi:10.1038/nphoton.2013.80.

[67] J. You, Z. Hong, Y. (Michael) Yang, Q. Chen, M. Cai, T.-B. Song, C.-C. Chen, S. Lu, Y. Liu, H. Zhou, Y. Yang, Low-Temperature Solution-Processed Perovskite Solar Cells with High Efficiency and Flexibility, ACS Nano. 8 (2014) 1674–1680. doi:10.1021/nn406020d.

[68] H. Luo, X. Lin, X. Hou, L. Pan, S. Huang, X. Chen, Efficient and Air-Stable Planar Perovskite Solar Cells Formed on Graphene-Oxide-Modified PEDOT:PSS Hole Transport Layer, Nano-Micro Letters. 9 (2017) 39. doi:10.1007/s40820-017-0140-x.

[69] P. Qin, N. Tetreault, M.I. Dar, P. Gao, K.L. McCall, S.R. Rutter, S.D. Ogier, N.D. Forrest, J.S. Bissett, M.J. Simms, A.J. Page, R. Fisher, M. Grätzel, M.K. Nazeeruddin, A Novel Oligomer as a Hole Transporting Material for Efficient Perovskite Solar Cells, Advanced Energy Materials. 5 (2015) 1400980. doi:10.1002/aenm.201400980.

[70] K. Do, H. Choi, K. Lim, H. Jo, J.W. Cho, M.K. Nazeeruddin, J. Ko, Star-shaped hole transporting materials with a triazine unit for efficient perovskite solar cells, Chem. Commun. 50 (2014) 10971–10974. doi:10.1039/C4CC04550E.

[71] H.-H. Chou, Y.-H. Chiang, M.-H. Li, P.-S. Shen, H.-J. Wei, C.-L. Mai, P. Chen, C.-Y. Yeh, Zinc Porphyrin–Ethynylaniline Conjugates as Novel Hole-Transporting Materials for Perovskite Solar Cells with Power Conversion Efficiency of 16.6%, ACS Energy Letters. 1 (2016) 956–962. doi:10.1021/acsenergylett.6b00432.

[72] K. Do, H. Choi, K. Lim, H. Jo, … J.C.-C., undefined 2014, Star-shaped hole transporting materials with a triazine unit for efficient perovskite solar cells, Pubs.Rsc.Org. (n.d.). https://pubs.rsc.org/en/content/articleHTLl/2014/cc/c4cc04550e (accessed September 19, 2019).

[73] M. Irwin, D. Buchholz, … A.H.-P. of the, undefined 2008, p-Type semiconducting nickel oxide as an efficiency-enhancing anode interfacial layer in polymer bulk-heterojunction solar cells, National Acad Sciences. (n.d.). https://www.pnas.org/content/105/8/2783.short (accessed September 24, 2019).

[74] W. Chen, Y. Wu, J. Liu, C. Qin, X. Yang, … A.I.-E.&, undefined 2015, Hybrid interfacial layer leads to solid performance improvement of inverted perovskite solar cells, Pubs.Rsc.Org. (n.d.). https://pubs.rsc.org/en/content/articleHTLl/2015/ee/c4ee02833c (accessed September 24, 2019).

[75] J.H. Park, J. Seo, S. Park, S.S. Shin, Y.C. Kim, N.J. Jeon, H.-W. Shin, T.K. Ahn, J.H. Noh, S.C. Yoon, C.S. Hwang, S. Il Seok, Efficient $CH_3NH_3PbI_3$ Perovskite Solar Cells Employing Nanostructured p-Type NiO Electrode Formed by a Pulsed Laser Deposition, Advanced Materials. 27 (2015) 4013–4019. doi:10.1002/adma.201500523.

[76] E. Fortunato, P. Barquinha, R. Martins, Oxide Semiconductor Thin-Film Transistors: A Review of Recent Advances, Advanced Materials. 24 (2012) 2945–2986. doi:10.1002/adma.201103228.

[77] J.A. Christians, R.C.M. Fung, P. V. Kamat, An inorganic hole conductor for Organo-lead halide perovskite solar cells. improved hole conductivity with copper iodide, Journal of the American Chemical Society. 136 (2014) 758–764. doi:10.1021/ja411014k.

[78] P. Qin, Q. He, D. Ouyang, G. Fang, … W.C.-S.C., undefined 2017, Transition metal oxides as hole-transporting materials in organic semiconductor and hybrid perovskite based solar cells, Springer. (n.d.). https://idp.springer.com/authorize/casa?redirect_uri=https://link.springer.com/article/10.1007/s11426-016-9023-

5&casa_token=UGY3s8I8aHgAAAAA:LYkIv5ocIVzNd5lSutX0tp8Om0KAZwzDLc9k4FRmFmKtJDrfKIpeoN7Emg_pkEdNmqM7TrKPxiB16IKt (accessed September 28, 2019).

[79] W. Yu, F. Li, H. Wang, E. Alarousu, Y. Chen, B. Lin, L.W.- Nanoscale, undefined 2016, Ultrathin Cu 2 O as an efficient inorganic hole transporting material for perovskite solar cells, Pubs.Rsc.Org. (n.d.). https://pubs.rsc.org/en/content/articleHTLl/2016/nr/c5nr07758c (accessed September 28, 2019).

[80] Z.-K. Yu, W.-F. Fu, W.-Q. Liu, Z.-Q. Zhang, Y.-J. Liu, J.-L. Yan, T. Ye, W.-T. Yang, H.-Y. Li, H.-Z. Chen, Solution-processed CuOx as an efficient hole-extraction layer for inverted planar heterojunction perovskite solar cells, Chinese Chemical Letters. 28 (2017) 13–18. doi:10.1016/J.CCLET.2016.06.021.

[81] C. Zuo, L. Ding, Solution-Processed Cu $_2$ O and CuO as Hole Transport Materials for Efficient Perovskite Solar Cells, Small. 11 (2015) 5528–5532. doi:10.1002/smll.201501330.

[82] C. Kumar, G. Sfyri, D. Raptis, E. Stathatos, P.L.-R. Advances, undefined 2015, Perovskite solar cell with low cost Cu-phthalocyanine as hole transporting material, Pubs.Rsc.Org. (n.d.). https://pubs.rsc.org/en/content/articleHTLl/2015/ra/c4ra14321c (accessed September 28, 2019).

[83] F. Zhang, X. Yang, M. Cheng, W. Wang, L.S.-N. Energy, undefined 2016, Boosting the efficiency and the stability of low cost perovskite solar cells by using CuPc nanorods as hole transport material and carbon as counter electrode, Elsevier. (n.d.). https://www.sciencedirect.com/science/article/pii/S221128551500470X (accessed September 28, 2019).

[84] B. Ezealigo, A. Nwanya, A. Simo, R.B.-… J. of Chemistry, undefined 2017, A study on solution deposited CuSCN thin films: Structural, electrochemical, optical properties, Elsevier. (n.d.). https://www.sciencedirect.com/science/article/pii/S1878535217300801 (accessed September 28, 2019).

[85] P. Qin, S. Tanaka, S. Ito, N. Tetreault, K. Manabe, H. Nishino, M.K. Nazeeruddin, M. Grätzel, Inorganic hole conductor-based lead halide perovskite solar cells with 12.4% conversion efficiency, Nature Communications. 5 (2014) 3834. doi:10.1038/ncomms4834.

[86] M. Jung, Y.C. Kim, N.J. Jeon, W.S. Yang, J. Seo, J.H. Noh, S. Il Seok, Thermal Stability of CuSCN Hole Conductor-Based Perovskite Solar Cells, ChemSusChem. 9 (2016) 2592–2596. doi:10.1002/cssc.201600957.

[87] Q.-D. Ou, C. Li, Q.-K. Wang, Y.-Q. Li, J.-X. Tang, Recent Advances in Energetics of Metal Halide Perovskite Interfaces, Advanced Materials Interfaces. 4 (2017) 1600694. doi:10.1002/admi.201600694.

[88] B. Kim, T. Kim, M. Choi, H. Shim, J.K.-O. Electronics, undefined 2015, Fully vacuum–processed perovskite solar cells with high open circuit voltage using MoO3/NPB as hole extraction layers, Elsevier. (n.d.). https://www.sciencedirect.com/science/article/pii/S1566119914005485 (accessed September 30, 2019).

[89] F. Hou, Z. Su, F. Jin, X. Yan, L. Wang, H. Zhao, J.Z.- Nanoscale, undefined 2015, Efficient and stable planar heterojunction perovskite solar cells with an MoO 3/PEDOT:

PSS hole transporting layer, Pubs.Rsc.Org. (n.d.). https://pubs.rsc.org/en/content/articleHTLl/2015/nr/c5nr01864a (accessed September 30, 2019).

[90] E. Della Gaspera, Y. Peng, Q. Hou, L. Spiccia, U.B.-N. Energy, undefined 2015, Ultra-thin high efficiency semitransparent perovskite solar cells, Elsevier. (n.d.). https://www.sciencedirect.com/science/article/pii/S2211285515000877 (accessed September 30, 2019).

[91] H. Sun, X. Hou, Q. Wei, H. Liu, K. Yang, … W.W.-C., undefined 2016, Low-temperature solution-processed p-type vanadium oxide for perovskite solar cells, Pubs.Rsc.Org. (n.d.). https://pubs.rsc.org/en/content/articleHTLl/2016/cc/c6cc03740b (accessed September 30, 2019).

[92] H. Peng, W. Sun, Y. Li, S. Ye, H. Rao, W. Yan, H. Zhou, Z. Bian, C. Huang, Solution processed inorganic V2O x as interfacial function materials for inverted planar-heterojunction perovskite solar cells with enhanced efficiency, Nano Research. 9 (2016) 2960–2971. doi:10.1007/s12274-016-1181-z.

[93] D. Wang, N.K. Elumalai, M.A. Mahmud, M. Wright, M.B. Upama, K.H. Chan, C. Xu, F. Haque, G. Conibeer, A. Uddin, V2O5 -PEDOT: PSS bilayer as hole transport layer for highly efficient and stable perovskite solar cells, Organic Electronics. 53 (2018) 66–73. doi:10.1016/J.ORGEL.2017.10.034.

[94] Z. Li, Stable Perovskite Solar Cells Based on WO_3 Nanocrystals as Hole Transport Layer, Chemistry Letters. 44 (2015) 1140–1141. doi:10.1246/cl.150445.

[95] Z.L.-C. Letters, undefined 2015, Stable Perovskite Solar Cells Based on WO3 Nanocrystals as Hole Transport Layer, Journal.Csj.Jp. (n.d.). https://www.journal.csj.jp/doi/abs/10.1246/cl.150445 (accessed October 4, 2019).

[96] Z. Tseng, L. Chen, C. Chiang, S. Chang, C.C.-S. Energy, undefined 2016, Efficient inverted-type perovskite solar cells using UV-ozone treated MoOx and WOx as hole transporting layers, Elsevier. (n.d.). https://www.sciencedirect.com/science/article/pii/S0038092X16304698 (accessed October 4, 2019).

[97] Y. Yang, J. Xiao, H. Wei, L. Zhu, D. Li, Y. Luo, H. Wu, Q. Meng, An all-carbon counter electrode for highly efficient hole-conductor-free organo-metal perovskite solar cells, RSC Adv. 4 (2014) 52825–52830. doi:10.1039/C4RA09519G.

[98] Z. Wei, H. Chen, K. Yan, X. Zheng, S.Y.-J. of Materials, undefined 2015, Hysteresis-free multi-walled carbon nanotube-based perovskite solar cells with a high fill factor, Pubs.Rsc.Org. (n.d.). https://pubs.rsc.org/en/content/articleHTLl/2015/ta/c5ta07714a (accessed October 5, 2019).

[99] H. Zhou, Y. Shi, Q. Dong, H. Zhang, Y. Xing, K. Wang, Y. Du, T. Ma, Hole-Conductor-Free, Metal-Electrode-Free TiO_2 /$CH_3NH_3PbI_3$ Heterojunction Solar Cells Based on a Low-Temperature Carbon Electrode, The Journal of Physical Chemistry Letters. 5 (2014) 3241–3246. doi:10.1021/jz5017069.

[100] L. Zhang, T. Liu, L. Liu, M. Hu, Y. Yang, … A.M.-J. of M., undefined 2015, The effect of carbon counter electrodes on fully printable mesoscopic perovskite solar cells, Pubs.Rsc.Org. (n.d.). https://pubs.rsc.org/en/content/articleHTLl/2015/ta/c4ta04647a (accessed October 7, 2019).

[101] L. Liu, A. Mei, T. Liu, P. Jiang, Y. Sheng, L. Zhang, H. Han, Fully Printable Mesoscopic Perovskite Solar Cells with Organic Silane Self-Assembled Monolayer, Journal of the American Chemical Society. 137 (2015) 1790–1793. doi:10.1021/ja5125594.

[102] Z. Wei, H. Chen, K. Yan, S. Yang, Inkjet Printing and Instant Chemical Transformation of a $CH_3NH_3PbI_3$/Nanocarbon Electrode and Interface for Planar Perovskite Solar Cells, Angewandte Chemie International Edition. 53 (2014) 13239–13243. doi:10.1002/anie.201408638.

[103] M.J. Jaison, T.N. Narayanan, T. Prem Kumar, V.K. Pillai, A single-step room-temperature electrochemical synthesis of nitrogen-doped graphene nanoribbons from carbon nanotubes, Journal of Materials Chemistry A. 3 (2015) 18222–18228. doi:10.1039/C5TA03869C.

[104] J.-S. Yeo, R. Kang, S. Lee, Y.-J. Jeon, N. Myoung, C.-L. Lee, D.-Y. Kim, J.-M. Yun, Y.-H. Seo, S.-S. Kim, S.-I. Na, Highly efficient and stable planar perovskite solar cells with reduced graphene oxide nanosheets as electrode interlayer, Nano Energy. 12 (2015) 96–104. doi:10.1016/J.NANOEN.2014.12.022.

[105] Y. Wang, X. Zhang, Q. Jiang, H. Liu, D. Wang, J. Meng, J. You, Z. Yin, Interface Engineering of High-Performance Perovskite Photodetectors Based on PVP/SnO 2 Electron Transport Layer, ACS Applied Materials and Interfaces. 10 (2018) 6505–6512. doi:10.1021/acsami.7b18511.

[106] S.S. Mali, J. V Patil, H. Arandiyan, C.K. Hong, Reduced methylammonium, triple-cation Rb0.05(FAPbI3)0.95(MAPbBr3)0.05 perovskite solar cells based on TiO2/SnO2 bilayered electron transporting layer approaching stabilized 21% efficiency: Role of antisolvent, Journal of Materials Chemistry A. (2019) 17516–17528. doi:10.1039/c9ta05422g.

[107] Q. Jiang, L. Zhang, H. Wang, X. Yang, J. Meng, H. Liu, Z. Yin, J. Wu, X. Zhang, J. You, Enhanced electron extraction using SnO2 for high-efficiency planar-structure HC(NH2)2 PbI3-based perovskite solar cells, Nature Energy. 2 (2017) 1–22. doi:10.1038/nenergy.2016.177.

[108] K. Ranabhat, L. Patrikeev, A.A. evna Revina, K. Andrianov, V. Lapshinsky, E. Sofronova, An introduction to solar cell technology, Journal of Applied Engineering Science. 14 (2016) 481–491. doi:10.5937/jaes14-10879.

[109] M.O. Reese, A.R. Marshall, G. Rumbles, CHAPTER 1: Reliably Measuring the Performance of Emerging Photovoltaic Solar Cells, in: RSC Nanoscience and Nanotechnology, Royal Society of Chemistry, 2018: pp. 1–32. doi:10.1039/9781782626749-00001.

[110] S. Kazim, M.K. Nazeeruddin, M. Grätzel, S. Ahmad, Perovskite as light harvester: A game changer in photovoltaics, Angewandte Chemie - International Edition. 53 (2014) 2812–2824. doi:10.1002/anie.201308719.

[111] G.E. Eperon, S.D. Stranks, C. Menelaou, M.B. Johnston, L.M. Herz, H.J. Snaith, Formamidinium lead trihalide: a broadly tunable perovskite for efficient planar heterojunction solar cells, Energy & Environmental Science. 7 (2014) 982–988.

[112] T.M. Koh, K. Fu, Y. Fang, S. Chen, T.C. Sum, N. Mathews, S.G. Mhaisalkar, P.P. Boix, T. Baikie, Formamidinium-containing metal-halide: an alternative material for near-IR absorption perovskite solar cells, The Journal of Physical Chemistry C. 118 (2013) 16458–16462.

[113] M. Salado, S. Kazim, M.K. Nazeeruddin, S. Ahmad, Appraisement of Crystal Expansion in CH 3 NH 3 PbI 3 on Doping: Improved Photovoltaic Properties, ChemSusChem. (2019) 1–8. doi:10.1002/cssc.201803043.

[114] Q. Lin, A. Armin, R.C.R. Nagiri, P.L. Burn, P. Meredith, Electro-optics of perovskite solar cells, Nature Photonics. 9 (2015) 106.

[115] Q. Sun, X. Gong, H. Li, S. Liu, X. Zhao, Y. Shen, M. Wang, Direct formation of I3- ions in organic cation solution for efficient perovskite solar cells, Solar Energy Materials and Solar Cells. 185 (2018) 111–116. doi:10.1016/j.solmat.2018.05.017.

[116] M. Wang, Z. Zang, B. Yang, X. Hu, K. Sun, L. Sun, Performance improvement of perovskite solar cells through enhanced hole extraction: The role of iodide concentration gradient, Solar Energy Materials and Solar Cells. 185 (2018) 117–123. doi:10.1016/j.solmat.2018.05.025.

[117] M. Salado, L. Calió, L. Contreras-Bernal, J. Idígoras, J.A. Anta, S. Ahmad, S. Kazim, Understanding the influence of interface morphology on the performance of perovskite solar cells, Materials. 11 (2018) 1–13. doi:10.3390/ma11071073.

[118] M. Salado, M. Oliva-Ramirez, S. Kazim, A.R. González-Elipe, S. Ahmad, 1-dimensional TiO2 nano-forests as photoanodes for efficient and stable perovskite solar cells fabrication, Nano Energy. 35 (2017) 215–222. doi:10.1016/j.nanoen.2017.03.034.

[119] J. Burschka, N. Pellet, S.-J. Moon, R. Humphry-Baker, P. Gao, M.K. Nazeeruddin, M. Grätzel, Sequential deposition as a route to high-performance perovskite-sensitized solar cells, Nature. 499 (2013) 316.

[120] X. Guo, H. Dong, W. Li, N. Li, L. Wang, Multifunctional MgO layer in perovskite solar cells, ChemPhysChem. 16 (2015) 1727–1732.

[121] T. Leijtens, G.E. Eperon, S. Pathak, A. Abate, M.M. Lee, H.J. Snaith, Overcoming ultraviolet light instability of sensitized TiO 2 with meso-superstructured organometal tri-halide perovskite solar cells, Nature Communications. 4 (2013) 2885.

[122] D. Liu, T.L. Kelly, Perovskite solar cells with a planar heterojunction structure prepared using room-temperature solution processing techniques, Nature Photonics. 8 (2014) 133.

[123] W. Ke, G. Fang, Q. Liu, L. Xiong, P. Qin, H. Tao, J. Wang, H. Lei, B. Li, J. Wan, Low-temperature solution-processed tin oxide as an alternative electron transporting layer for efficient perovskite solar cells, Journal of the American Chemical Society. 137 (2015) 6730–6733.

[124] J.P.C. Baena, L. Steier, W. Tress, M. Saliba, S. Neutzner, T. Matsui, F. Giordano, T.J. Jacobsson, A.R.S. Kandada, S.M. Zakeeruddin, Highly efficient planar perovskite solar cells through band alignment engineering, Energy & Environmental Science. 8 (2015) 2928–2934.

[125] E.H. Anaraki, A. Kermanpur, L. Steier, K. Domanski, T. Matsui, W. Tress, M. Saliba, A. Abate, M. Grätzel, A. Hagfeldt, Highly efficient and stable planar perovskite solar cells by solution-processed tin oxide, Energy & Environmental Science. 9 (2016) 3128–3134.

[126] E. Salmani, A. Laghrissi, R. Lamouri, M. Rouchdi, M. Dehmani, H. Ez-Zahraouy, N. Hassanain, A. Mzerd, A. Benyoussef, Theoretical study of electronic, magnetic and optical properties of TM (V, Cr, Mn and Fe) doped SnO2: ab-initio and Monte Carlo

simulation, Optical and Quantum Electronics. 50 (2018) 1–11. doi:10.1007/s11082-018-1355-x.

[127] J. Gong, S.B. Darling, F. You, Perovskite photovoltaics: life-cycle assessment of energy and environmental impacts, Energy & Environmental Science. 8 (2015) 1953–1968.

[128] L. Calió, S. Kazim, M. Grätzel, S. Ahmad, Hole-Transport Materials for Perovskite Solar Cells, Angewandte Chemie - International Edition. 55 (2016) 14522–14545. doi:10.1002/anie.201601757.

[129] L. Calió, S. Kazim, M. Grätzel, S. Ahmad, Lochtransportmaterialien für Perowskit-Solarzellen, Angewandte Chemie. 128 (2016) 14740–14764. doi:10.1002/ange.201601757.

[130] S. Cogal, L. Calio, G. Celik Cogal, M. Salado, S. Kazim, L. Oksuz, S. Ahmad, A. Uygun Oksuz, RF plasma-enhanced graphene–polymer composites as hole transport materials for perovskite solar cells, Polymer Bulletin. 75 (2018) 4531–4545. doi:10.1007/s00289-018-2275-4.

[131] L. Calió, C. Momblona, L. Gil-Escrig, S. Kazim, M. Sessolo, Á. Sastre-Santos, H.J. Bolink, S. Ahmad, Vacuum deposited perovskite solar cells employing dopant-free triazatruxene as the hole transport material, Solar Energy Materials and Solar Cells. 163 (2017) 237–241. doi:10.1016/j.solmat.2017.01.037.

[132] Y. Di, Q. Zeng, C. Huang, D. Tang, K. Sun, C. Yan, Y. Wang, S. Ke, L. Jiang, X. Hao, Y. Lai, F. Liu, Thermal-evaporated selenium as a hole-transporting material for planar perovskite solar cells, Solar Energy Materials and Solar Cells. 185 (2018) 130–135. doi:10.1016/j.solmat.2018.05.022.

[133] C. Garza, S. Shaji, A. Arato, E. Perez Tijerina, G. Alan Castillo, T.K. Das Roy, B. Krishnan, P-Type CuSbS2 thin films by thermal diffusion of copper into Sb2S3, Solar Energy Materials and Solar Cells. 95 (2011) 2001–2005. doi:10.1016/j.solmat.2010.06.011.

[134] J. Zhou, G.Q. Bian, Q.Y. Zhu, Y. Zhang, C.Y. Li, J. Dai, Solvothermal crystal growth of CuSbQ2 (Q=S, Se) and the correlation between macroscopic morphology and microscopic structure, Journal of Solid State Chemistry. 182 (2009) 259–264. doi:10.1016/j.jssc.2008.10.025.

[135] W. Yu, F. Li, H. Wang, E. Alarousu, Y. Chen, B. Lin, L. Wang, M.N. Hedhili, Y. Li, K. Wu, X. Wang, O.F. Mohammed, T. Wu, Ultrathin Cu 2 O as an efficient inorganic hole transporting material for perovskite solar cells, Nanoscale. 8 (2016) 6173–6179. doi:10.1039/c5nr07758c.

[136] M.I. Hossain, F.H. Alharbi, N. Tabet, Copper oxide as inorganic hole transport material for lead halide perovskite based solar cells, Solar Energy. 120 (2015) 370–380. doi:10.1016/J.SOLENER.2015.07.040.

[137] P. Qin, S. Tanaka, S. Ito, N. Tetreault, K. Manabe, H. Nishino, M.K. Nazeeruddin, M. Grätzel, Inorganic hole conductor-based lead halide perovskite solar cells with 12.4% conversion efficiency, Nature Communications. 5 (2014) 1–6. doi:10.1038/ncomms4834.

[138] P. Ahirrao, S. Gosavi, … S.S.-A. of P., undefined 2011, Wide band gap nanocrystalline CuSCN thin films deposited by modified chemical method, Researchgate.Net. (n.d.).

https://www.researchgate.net/profile/R_Patil5/publication/266461469_Wide_band_gap_nanocrystalline_CuSCN_thin_films_deposited_by_modified_chemical_method/links/5652bbf508aefe619b18d9ca.pdf (accessed February 11, 2019).

[139] F. Anwar, R. Mahbub, S. Satter, S.U.-I.J. of, undefined 2017, Effect of Different HTL Layers and Electrical Parameters on ZnO Nanorod-Based Lead-Free Perovskite Solar Cell for High-Efficiency Performance, Hindawi.Com. (n.d.). https://www.hindawi.com/journals/ijp/2017/9846310/abs/ (accessed February 11, 2019).

[140] A. Baumann, J. Lorrmann, C. Deibel, V. Dyakonov, Bipolar charge transport in poly(3-hexyl thiophene)/methanofullerene blends: A ratio dependent study, Applied Physics Letters. 93 (2008) 252104. doi:10.1063/1.3055608.

[141] F. Behrouznejad, S. Shahbazi, … N.T.-J. of M., undefined 2016, A study on utilizing different metals as the back contact of CH 3 NH 3 PbI 3 perovskite solar cells, Pubs.Rsc.Org. (n.d.). http://pubs.rsc.org/en/content/articleHTLl/2016/ta/c6ta05938d (accessed February 11, 2019).

[142] E.J. Juarez-Perez, M. Wußler, F. Fabregat-Santiago, K. Lakus-Wollny, E. Mankel, T. Mayer, W. Jaegermann, I. Mora-Sero, Role of the selective contacts in the performance of lead halide perovskite solar cells, Journal of Physical Chemistry Letters. 5 (2014) 680–685. doi:10.1021/jz500059v.

[143] A. Hussain, R. Ahmed, N. Ali, F. Butt, … A.S.-S. and, undefined 2016, Post annealing effects on structural, optical and electrical properties of CuSbS2 thin films fabricated by combinatorial thermal evaporation technique, Elsevier. (n.d.). https://www.sciencedirect.com/science/article/pii/S074960361530241X (accessed February 11, 2019).

[144] K. Mahmood, S. Sarwar, M.T. Mehran, Current status of electron transport layers in perovskite solar cells: materials and properties, (2017). doi:10.1039/c7ra00002b.

[145] W.A. Laban, L. Etgar, Depleted hole conductor-free lead halide iodide heterojunction solar cells, Energy & Environmental Science. 6 (2013) 3249–3253.

[146] H. Zhou, Q. Chen, G. Li, S. Luo, T. -b. Song, H.-S. Duan, Z. Hong, J. You, Y. Liu, Y. Yang, Interface engineering of highly efficient perovskite solar cells, Science. 345 (2014) 542–546. doi:10.1126/science.1254050.

[147] C.R. Brown, V.R. Whiteside, D. Poplavskyy, K. Hossain, M.S. Dhoubhadel, I.R. Sellers, Flexible Cu(In,Ga)Se 2 Solar Cells for Outer Planetary Missions: Investigation under Low-Intensity Low-Temperature Conditions, IEEE Journal of Photovoltaics. 9 (2019) 552–558. doi:10.1109/JPHOTOV.2018.2889179.

[148] C.C. Stoumpos, C.D. Malliakas, M.G. Kanatzidis, Semiconducting tin and lead iodide perovskites with organic cations: Phase transitions, high mobilities, and near-infrared photoluminescent properties, Inorganic Chemistry. 52 (2013) 9019–9038. doi:10.1021/ic401215x.

[149] R. Teimouri, R.M.-S. and Microstructures, U. 2018, Potential application of CuSbS2 as the hole transport material in perovskite solar cell: A simulation study, Superlattices and Microstructures. 118 (2018) 116–122. doi:10.1016/j.spmi.2018.03.079.

[150] M. Wang, C. Grätzel, S.-J. Moon, R. Humphry-Baker, N. Rossier-Iten, S.M. Zakeeruddin, M. Grätzel, Surface Design in Solid-State Dye Sensitized Solar Cells: Effects of

Zwitterionic Co-adsorbents on Photovoltaic Performance, Advanced Functional Materials. 19 (2009) 2163–2172. doi:10.1002/adfm.200900246.

[151] X. Wei, X. Wang, H. Jiang, Y. Huang, A. Han, Q. Gao, J. Bian, Z. Liu, Numerical simulation and experimental validation of inverted planar perovskite solar cells based on NiOxhole transport layer, Superlattices and Microstructures. 112 (2017) 383–393. doi:10.1016/j.spmi.2017.09.048.

[152] A.F. Khan, M. Mehmood, M. Aslam, M. Ashraf, Characteristics of electron beam evaporated nanocrystalline SnO 2 thin films annealed in air, Applied Surface Science. 256 (2010) 2252–2258. doi:10.1016/j.apsusc.2009.10.047.

[153] G. Martínez-Denegri, S. Colodrero, M. Kramarenko, J. Martorell, All-Nanoparticle SnO_2 /TiO_2 Electron-Transporting Layers Processed at Low Temperature for Efficient Thin-Film Perovskite Solar Cells, ACS Applied Energy Materials. (2018) acsaem.8b01118. doi:10.1021/acsaem.8b01118.

[154] P. Pinpithak, H.-W. Chen, A. Kulkarni, Y. Sanehira, M. Ikegami, T. Miyasaka, Low-temperature and Ambient Air Processes of Amorphous SnO_x -based Mixed Halide Perovskite Planar Solar Cell, Chemistry Letters. 46 (2017) 382–384. doi:10.1246/cl.161060.

[155] B. Roose, J.-P.C. Baena, K.C. Gödel, M. Graetzel, A. Hagfeldt, U. Steiner, A. Abate, Mesoporous SnO2 electron selective contact enables UV-stable perovskite solar cells, Nano Energy. 30 (2016) 517–522. doi:10.1016/J.NANOEN.2016.10.055.

[156] K. Adhikari, S. Gurung, … B.B. status solidi, undefined 2016, Comparative study on MAPbI3 based solar cells using different electron transporting materials, Wiley Online Library. (n.d.). https://onlinelibrary.wiley.com/doi/abs/10.1002/pssc.201510078 (accessed February 11, 2019).

[157] E. Anaraki, A. Kermanpur, … L.S.-E.&, undefined 2016, Highly efficient and stable planar perovskite solar cells by solution-processed tin oxide, Pubs.Rsc.Org. (n.d.). http://pubs.rsc.org/en/content/articleHTLl/2016/ee/c6ee02390h (accessed February 11, 2019).

[158] L. Xiong, Y. Guo, J. Wen, H. Liu, G. Yang, P. Qin, G. Fang, Review on the Application of SnO2 in Perovskite Solar Cells, Advanced Functional Materials. 28 (2018) 1–18. doi:10.1002/adfm.201802757.

[159] Y.J. Huang, H.C. Chen, H.K. Lin, K.H. Wei, Doping ZnO Electron Transport Layers with MoS2 Nanosheets Enhances the Efficiency of Polymer Solar Cells, ACS Applied Materials and Interfaces. 10 (2018) 20196–20204. doi:10.1021/acsami.8b06413.

[160] T. Kirchartz, T. Agostinelli, M. Campoy-Quiles, W. Gong, J. Nelson, Understanding the Thickness-Dependent Performance of Organic Bulk Heterojunction Solar Cells: The Influence of Mobility, Lifetime, and Space Charge, The Journal of Physical Chemistry Letters. 3 (2012) 3470–3475. doi:10.1021/jz301639y.

[161] M.A. Green, Accuracy of analytical expressions for solar cell fill factors, Solar Cells. 7 (1982) 337–340. doi:10.1016/0379-6787(82)90057-6.

[162] K.R. Adhikari, S. Gurung, B.K. Bhattarai, B.M. Soucase, Comparative study on $MAPbI_3$ based solar cells using different electron transporting materials, Physica Status Solidi (C). 13 (2016) 13–17. doi:10.1002/pssc.201510078.

[163] V.A. Trukhanov, V. V Bruevich, D.Y. Paraschuk, Effect of doping on performance of organic solar cells, PHYSICAL REVIEW B. 84 (2011) 205318.

doi:10.1103/PhysRevB.84.205318.

[164] V.E. Madhavan, I. Zimmermann, C. Roldán-Carmona, G. Grancini, M. Buffiere, A. Belaidi, M.K. Nazeeruddin, Copper Thiocyanate Inorganic Hole-Transporting Material for High-Efficiency Perovskite Solar Cells, ACS Energy Letters. 1 (2016) 1112–1117. doi:10.1021/acsenergylett.6b00501.

[165] G.W. Kim, D. V. Shinde, T. Park, Thickness of the hole transport layer in perovskite solar cells: Performance versus reproducibility, RSC Advances. 5 (2015) 99356–99360. doi:10.1039/c5ra18648j.

[166] [6]Best-Research-Cell-Efficiencies.20191106.Pdf, (n.d.).

[167] Y. Raoui, H. Ez-Zahraouy, N. Tahiri, O. El Bounagui, S. Ahmad, S. Kazim, Performance analysis of MAPbI3 based perovskite solar cells employing diverse charge selective contacts: Simulation study, Solar Energy. 193 (2019) 948–955. doi:10.1016/j.solener.2019.10.009.

[168] H.S. Kim, C.R. Lee, J.H. Im, K.B. Lee, T. Moehl, A. Marchioro, S.J. Moon, R. Humphry-Baker, J.H. Yum, J.E. Moser, M. Grätzel, N.G. Park, Lead iodide perovskite sensitized all-solid-state submicron thin film mesoscopic solar cell with efficiency exceeding 9%, Scientific Reports. 2 (2012) 1–7. doi:10.1038/srep00591.

[169] M. Liu, M.B. Johnston, H.J. Snaith, Efficient planar heterojunction perovskite solar cells by vapour deposition, Nature. 501 (2013) 395–398. doi:10.1038/nature12509.

[170] Y.H. Hu, Novel Meso-Superstructured Solar Cells with a High Efficiency Exceeding 12%, Advanced Materials. 26 (2014) 2102–2104. doi:10.1002/adma.201304732.

[171] M. Salado, L. Calio, R. Berger, S. Kazim, S. Ahmad, Influence of the mixed organic cation ratio in lead iodide based perovskite on the performance of solar cells, Physical Chemistry Chemical Physics. 18 (2016) 27148–27157. doi:10.1039/c6cp03851d.

[172] Y. Chen, Q. Meng, L. Zhang, C. Han, H. Gao, Y. Zhang, H. Yan, SnO2-based electron transporting layer materials for perovskite solar cells: A review of recent progress, Journal of Energy Chemistry. 35 (2019) 144–167. doi:10.1016/j.jechem.2018.11.011.

[173] G. Yang, P. Qin, G. Fang, G. Li, Tin oxide (SnO2) as effective electron selective layer material in hybrid organic–inorganic metal halide perovskite solar cells, Journal of Energy Chemistry. 27 (2018) 962–970. doi:10.1016/j.jechem.2018.03.018.

[174] Q. Dong, Y. Shi, C. Zhang, Y. Wu, L. Wang, Energetically favored formation of SnO2nanocrystals as electron transfer layer in perovskite solar cells with high efficiency exceeding 19%, Nano Energy. 40 (2017) 336–344. doi:10.1016/j.nanoen.2017.08.041.

[175] C.C. Stoumpos, D. Cao, Lead-Free Solid-State Organic-Inorganic Halide Perovskite Solar Cells, (2014). doi:10.1038/nphoton.2014.82.

[176] V.S. Nair, F. Yan, S.N. Vijayaraghavan, J. Wall, L. Li, G. Xing, Q. Zhang, Low Temperature Processed Highly Efficient Hole-Transport-Layer Free Carbon-based Planar Perovskite Solar Cells with SnO2 Quantum Dot Electron-Transport-Layer Thin film perovskite solar cells View project Low-temperature processed highly efficient hole transport layer free carbon-based planar perovskite solar cells with SnO 2 quantum dot electron transport layer, (2020). doi:10.1016/j.mtphys.2020.100204.

[177] G. Yang, C. Chen, F. Yao, Z. Chen, Q. Zhang, X. Zheng, J. Ma, H. Lei, P. Qin,

L. Xiong, W. Ke, G. Li, Y. Yan, G. Fang, Effective Carrier-Concentration Tuning of SnO_2 Quantum Dot Electron-Selective Layers for High-Performance Planar Perovskite Solar Cells, Advanced Materials. 30 (2018) 1706023. doi:10.1002/adma.201706023.

[178] G. Wu, J. Zhou, R. Meng, B. Xue, H. Zhou, Z. Tang, Y. Zhang, Air-stable formamidinium/methylammonium mixed lead iodide perovskite integral microcrystals with low trap density and high photo-responsivity, Physical Chemistry Chemical Physics : PCCP. 21 (2019) 3106–3113. doi:10.1039/c8cp07271j.

[179] Q. Jiang, L. Zhang, H. Wang, X. Yang, J. Meng, H.L.-N. Energy, undefined 2017, Enhanced electron extraction using SnO2 for high-efficiency planar-structure HC(NH2)2PbI3-based perovskite solar cells, Nature.Com. (n.d.). https://www.nature.com/articles/nenergy2016177 (accessed September 4, 2019).

[180] F. Hernandez-Ramirez, J.D. Prades, A. Tarancon, S. Barth, O. Casals, R. Jimenez-Diaz, E. Pellicer, J. Rodriguez, J.R. Morante, M.A. Juli, S. Mathur, A. Romano-Rodriguez, Insight into the Role of Oxygen Diffusion in the Sensing Mechanisms of SnO_2 Nanowires, Advanced Functional Materials. 18 (2008) 2990–2994. doi:10.1002/adfm.200701191.

[181] T.S. Sherkar, C. Momblona, L. Gil-Escrig, J. Ávila, M. Sessolo, H.J. Bolink, L.J.A. Koster, Recombination in Perovskite Solar Cells: Significance of Grain Boundaries, Interface Traps, and Defect Ions, ACS Energy Letters. 2 (2017) 1214–1222. doi:10.1021/acsenergylett.7b00236.

[182] C. Ding, Y. Zhang, F. Liu, Y. Kitabatake, S. Hayase, T. Toyoda, K. Yoshino, T. Minemoto, K. Katayama, Q. Shen, Effect of the conduction band offset on interfacial recombination behavior of the planar perovskite solar cells, Nano Energy. 53 (2018) 17–26. doi:10.1016/j.nanoen.2018.08.031.

[183] A.A.B. Baloch, S.P. Aly, M.I. Hossain, F. El-Mellouhi, N. Tabet, F.H. Alharbi, Full space device optimization for solar cells, Scientific Reports. 7 (2017) 1–14. doi:10.1038/s41598-017-12158-0.

[184] H.S. Rao, B.X. Chen, W.G. Li, Y.F. Xu, H.Y. Chen, D. Bin Kuang, C.Y. Su, Improving the Extraction of Photogenerated Electrons with SnO2 Nanocolloids for Efficient Planar Perovskite Solar Cells, Advanced Functional Materials. 25 (2015) 7200–7207. doi:10.1002/adfm.201501264.

[185] T. Leijtens, G.E. Eperon, S. Pathak, A. Abate, M.M. Lee, H.J. Snaith, Overcoming ultraviolet light instability of sensitized TiO2 with meso-superstructured organometal tri-halide perovskite solar cells, Nature Communications. 4 (2013) 1–8. doi:10.1038/ncomms3885.

[186] Y. Reyna, M. Salado, S. Kazim, A.P.-T.-N. Energy, undefined 2016, Performance and stability of mixed FAPbI3 (0.85) MAPbBr3 (0.15) halide perovskite solar cells under outdoor conditions and the effect of low light irradiation, Elsevier. (n.d.). https://www.sciencedirect.com/science/article/pii/S2211285516304700 (accessed September 4, 2019).

[187] Y. Li, W. Yan, Y. Li, S. Wang, W. Wang, Z. Bian, L. Xiao, Direct Observation of Long Electron-Hole Diffusion Distance_Supplementary, Scientific Reports. 5 (2015) 14485. doi:10.1038/srep14485.

[188] M. Burgelman, P. Nollet, S.D.-T.S. Films, undefined 2000, Modelling

polycrystalline semiconductor solar cells, Elsevier. (n.d.). https://www.sciencedirect.com/science/article/pii/S0040609099008251 (accessed September 4, 2019).

[189] T.J. Barr, R.N. Sampaio, B.N. DiMarco, E.M. James, G.J. Meyer, Phantom Electrons in Mesoporous Nanocrystalline SnO_2 Thin Films with Cation-Dependent Reduction Onsets, Chemistry of Materials. 29 (2017) 3919–3927. doi:10.1021/acs.chemmater.6b05470.

[190] K.T. Cho, S. Paek, G. Grancini, C. Roldán-Carmona, P. Gao, Y. Lee, M.K. Nazeeruddin, Highly efficient perovskite solar cells with a compositionally engineered perovskite/hole transporting material interface, Energy and Environmental Science. 10 (2017) 621–627. doi:10.1039/c6ee03182j.

[191] M.C. Wu, S.H. Chan, K.M. Lee, S.H. Chen, M.H. Jao, Y.F. Chen, W.F. Su, Enhancing the efficiency of perovskite solar cells using mesoscopic zinc-doped TiO 2 as the electron extraction layer through band alignment, Journal of Materials Chemistry A. 6 (2018) 16920–16931. doi:10.1039/c8ta05291c.

[192] Y. Huang, L. Li, Z. Liu, H. Jiao, Y. He, X. Wang, R. Zhu, D. Wang, J. Sun, Q. Chen, H. Zhou, The intrinsic properties of FA(1-:X)MAxPbI3 perovskite single crystals, Journal of Materials Chemistry A. 5 (2017) 8537–8544. doi:10.1039/c7ta01441d.

[193] H.J. Snaith, C. Ducati, SnO_2 -Based Dye-Sensitized Hybrid Solar Cells Exhibiting Near Unity Absorbed Photon-to-Electron Conversion Efficiency, Nano Letters. 10 (2010) 1259–1265. doi:10.1021/nl903809r.

[194] D. Yang, R. Yang, K. Wang, C. Wu, X. Zhu, J. Feng, X. Ren, G. Fang, S. Priya, S. (Frank) Liu, High efficiency planar-type perovskite solar cells with negligible hysteresis using EDTA-complexed SnO 2, Nature Communications. 9 (2018). doi:10.1038/s41467-018-05760-x.

[195] C.-S. Jiang, M. Yang, Y. Zhou, B. To, S.U. Nanayakkara, J.M. Luther, W. Zhou, J.J. Berry, J. van de Lagemaat, N.P. Padture, K. Zhu, M.M. Al-Jassim, Carrier separation and transport in perovskite solar cells studied by nanometre-scale profiling of electrical potential, Nature Communications. 6 (2015) 8397. doi:10.1038/ncomms9397.

[196] F. Lan, M. Jiang, Q. Tao, G.L.-I.J. of Photovoltaics, undefined 2017, Revealing the working mechanisms of planar perovskite solar cells with cross-sectional surface potential profiling, Ieeexplore.Ieee.Org. (n.d.). https://ieeexplore.ieee.org/abstract/document/8094226/ (accessed September 4, 2019).

[197] R.A.-E.S. of S. Heterojunctions, undefined 1988, Experiments on ge-gaas heterojunctions, Springer. (n.d.). https://link.springer.com/chapter/10.1007/978-94-009-3073-5_2 (accessed September 4, 2019).

[198] T.H. Lai, S.W. Tsang, J.R. Manders, S. Chen, F. So, Properties of interlayer for organic photovoltaics, Materials Today. 16 (2013) 424–432. doi:10.1016/j.mattod.2013.10.001.

[199] K. Tvingstedt, C. Deibel, Temperature Dependence of Ideality Factors in Organic Solar Cells and the Relation to Radiative Efficiency, Advanced Energy Materials. 6 (2016) 1502230. doi:10.1002/aenm.201502230.

[200] J. Xie, K. Huang, X. Yu, Z. Yang, K. Xiao, Y. Qiang, X. Zhu, L. Xu, P. Wang, C. Cui, D. Yang, Enhanced Electronic Properties of SnO2 via Electron Transfer from Graphene

Quantum Dots for Efficient Perovskite Solar Cells, ACS Nano. 11 (2017) 9176–9182. doi:10.1021/acsnano.7b04070.

[201] S.C. Yoon, S.H. Eom, S.-H. Lee, V.-H. Tran, S.-K. Kim, Enhancing device performance of inverted organic solar cells with SnO2/Cs2CO3 as dual electron transport layers, Organic Electronics. 68 (2019) 85–95. doi:10.1016/j.orgel.2019.02.006.

[202] J.-P. Correa-Baena, M. Saliba, T. Buonassisi, M. Grätzel, A. Abate, W. Tress, A. Hagfeldt, Promises and challenges of perovskite solar cells., Science (New York, N.Y.). 358 (2017) 739–744. doi:10.1126/science.aam6323.

[203] G. Bai, Z. Wu, J. Li, T. Bu, W. Li, W. Li, F. Huang, Q. Zhang, Y.B. Cheng, J. Zhong, High performance perovskite sub-module with sputtered SnO 2 electron transport layer, Solar Energy. 183 (2019) 306–314. doi:10.1016/j.solener.2019.03.026.

[204] M.A. Green, A. Ho-Baillie, H.J. Snaith, The emergence of perovskite solar cells, Nature Photonics. 8 (2014) 506–514. doi:10.1038/nphoton.2014.134.

[205] M. Kulbak, S. Gupta, N. Kedem, I. Levine, T. Bendikov, G. Hodes, D. Cahen, Cesium Enhances Long-Term Stability of Lead Bromide Perovskite-Based Solar Cells, Journal of Physical Chemistry Letters. 7 (2016) 167–172. doi:10.1021/acs.jpclett.5b02597.

[206] A. Marronnier, G. Roma, S. Boyer-Richard, L. Pedesseau, J.M. Jancu, Y. Bonnassieux, C. Katan, C.C. Stoumpos, M.G. Kanatzidis, J. Even, Anharmonicity and Disorder in the Black Phases of Cesium Lead Iodide Used for Stable Inorganic Perovskite Solar Cells, ACS Nano. 12 (2018) 3477–3486. doi:10.1021/acsnano.8b00267.

[207] R.J. Sutton, G.E. Eperon, L. Miranda, E.S. Parrott, B.A. Kamino, J.B. Patel, M.T. Hörantner, M.B. Johnston, A.A. Haghighirad, D.T. Moore, H.J. Snaith, Bandgap-Tunable Cesium Lead Halide Perovskites with High Thermal Stability for Efficient Solar Cells, Advanced Energy Materials. 6 (2016) 1502458. doi:10.1002/aenm.201502458.

[208] W. Chen, H. Chen, G. Xu, R. Xue, S. Wang, Y. Li, Y. Li, Precise Control of Crystal Growth for Highly Efficient CsPbI 2 Br Perovskite Solar Cells, Joule. 3 (2019) 191–204. doi:10.1016/j.joule.2018.10.011.

[209] H. Rao, S. Ye, F. Gu, Z. Zhao, Z. Liu, Z. Bian, C. Huang, Morphology Controlling of All-Inorganic Perovskite at Low Temperature for Efficient Rigid and Flexible Solar Cells, Advanced Energy Materials. 8 (2018) 1800758. doi:10.1002/aenm.201800758.

[210] W. Chen, H. Chen, G. Xu, R. Xue, S. Wang, Y. Li, Y. Li, Precise Control of Crystal Growth for Highly Efficient CsPbI 2 Br Perovskite Solar Cells, Joule. 3 (2019) 191–204. doi:10.1016/j.joule.2018.10.011.

[211] L. Yan, Q. Xue, M. Liu, Z. Zhu, J. Tian, Z. Li, Z. Chen, Z. Chen, H. Yan, H.-L. Yip, Y. Cao, Interface Engineering for All-Inorganic CsPbI $_2$ Br Perovskite Solar Cells with Efficiency over 14%, Advanced Materials. 30 (2018) 1802509. doi:10.1002/adma.201802509.

[212] Q. Zeng, X. Zhang, C. Liu, T. Feng, Z. Chen, W. Zhang, W. Zheng, H. Zhang, B. Yang, Inorganic CsPbI 2 Br Perovskite Solar Cells: The Progress and Perspective , Solar RRL. 3 (2019) 1800239. doi:10.1002/solr.201800239.

[213] G. Yin, H. Zhao, H. Jiang, S. Yuan, T. Niu, K. Zhao, Z. Liu, S. (Frank) Liu, Precursor Engineering for All-Inorganic CsPbI 2 Br Perovskite Solar Cells with 14.78% Efficiency, Advanced Functional Materials. 28 (2018) 1803269. doi:10.1002/adfm.201803269.

[214] Y. Han, H. Zhao, C. Duan, S. Yang, Z. Yang, Z. Liu, S. (Frank) Liu, Controlled n-Doping in Air-Stable CsPbI 2 Br Perovskite Solar Cells with a Record Efficiency of 16.79%, Advanced Functional Materials. (2020) 1909972. doi:10.1002/adfm.201909972.

[215] B. Saparov, J.P. Sun, W. Meng, Z. Xiao, H.S. Duan, O. Gunawan, D. Shin, I.G. Hill, Y. Yan, D.B. Mitzi, Thin-Film Deposition and Characterization of a Sn-Deficient Perovskite Derivative Cs2SnI6, Chemistry of Materials. 28 (2016) 2315–2322. doi:10.1021/acs.chemmater.6b00433.

[216] W.J. Yin, T. Shi, Y. Yan, Superior photovoltaic properties of lead halide perovskites: Insights from first-principles theory, Journal of Physical Chemistry C. 119 (2015) 5253–5264. doi:10.1021/jp512077m.

[217] W.J. Yin, T. Shi, Y. Yan, Unique properties of halide perovskites as possible origins of the superior solar cell performance, Advanced Materials. 26 (2014) 4653–4658. doi:10.1002/adma.201306281.

[218] A.E. Shalan, S. Kazim, S. Ahmad, Lead-Free Perovskites: Metals Substitution towards Environmentally Benign Solar Cell Fabrication, ChemSusChem. 12 (2019) 4116–4139. doi:10.1002/cssc.201901296.

[219] C.C. Stoumpos, C.D. Malliakas, M.G. Kanatzidis, Semiconducting Tin and Lead Iodide Perovskites with Organic Cations: Phase Transitions, High Mobilities, and Near-Infrared Photoluminescent Properties, Inorg. Chem. 52 (2013). doi:10.1021/ic401215x.

[220] R. Wang, M. Mujahid, Y. Duan, Z.-K. Wang, J. Xue, Y. Yang, A Review of Perovskites Solar Cell Stability, Advanced Functional Materials. (2019) 1808843. doi:10.1002/adfm.201808843.

[221] Z. Chen, J.J. Wang, Y. Ren, C. Yu, K. Shum, Schottky solar cells based on CsSnI3thin-films, Applied Physics Letters. 101 (2012). doi:10.1063/1.4748888.

[222] I. Chung, J.H. Song, J. Im, J. Androulakis, C.D. Malliakas, H. Li, A.J. Freeman, J.T. Kenney, M.G. Kanatzidis, CsSnI 3: Semiconductor or metal? High electrical conductivity and strong near-infrared photoluminescence from a single material. High hole mobility and phase-transitions, Journal of the American Chemical Society. 134 (2012) 8579–8587. doi:10.1021/ja301539s.

[223] K.P. Marshall, M. Walker, R.I. Walton, R.A. Hatton, Elucidating the role of the hole-extracting electrode on the stability and efficiency of inverted CsSnI3/C60 perovskite photovoltaics, Journal of Materials Chemistry A. 5 (2017) 21836–21845. doi:10.1039/c7ta05967a.

[224] M.H. Kumar, S. Dharani, W.L. Leong, P.P. Boix, R.R. Prabhakar, T. Baikie, C. Shi, H. Ding, R. Ramesh, M. Asta, M. Graetzel, S.G. Mhaisalkar, N. Mathews, Lead-free halide perovskite solar cells with high photocurrents realized through vacancy modulation, Advanced Materials. 26 (2014) 7122–7127. doi:10.1002/adma.201401991.

[225] D. Sabba, H.K. Mulmudi, R.R. Prabhakar, T. Krishnamoorthy, T. Baikie, P.P. Boix, S. Mhaisalkar, N. Mathews, Impact of anionic Br-substitution on open circuit voltage in lead free perovskite (CsSnI3-xBrx) solar cells, Journal of Physical Chemistry C. 119 (2015) 1763–1767. doi:10.1021/jp5126624.

[226] Y. Raoui, H. Ez-zahraouy, S. Kazim, S. Ahmad, Energy level engineering of charge selective contact and halide perovskite by modulating band offset : Mechanistic insights,

(n.d.) 1–17.

[227] marcus-cmc/Shockley-Queisser-limit: Calculation and visualization tools for theoretical solar cell efficiencies based on the Shockley Queisser limit with options to change temperature, light intensity, and radiative efficiency, (n.d.). https://github.com/marcus-cmc/Shockley-Queisser-limit (accessed June 26, 2020).

[228] J. Zhuang, Y. Wei, Y. Luan, N. Chen, P. Mao, S. Cao, J. Wang, Band engineering at the interface of all-inorganic CsPbI2Br solar cells, Nanoscale. 11 (2019) 14553–14560. doi:10.1039/c9nr03638e.

[229] J. Wang, W. Fu, S. Jariwala, I. Sinha, A.K.Y. Jen, D.S. Ginger, Reducing Surface Recombination Velocities at the Electrical Contacts Will Improve Perovskite Photovoltaics, ACS Energy Letters. 4 (2019) 222–227. doi:10.1021/acsenergylett.8b02058.

[230] K. Masumura, I. Nakanishi, K. Van Thi Khuat, K. Kinashi, W. Sakai, N. Tsutsumi, Optimal composition of the poly(triarylamine)-based polymer composite to maximize photorefractive performance, Scientific Reports. 9 (2019) 1–9. doi:10.1038/s41598-018-36980-2.

[231] X. Meng, Z. Wang, W. Qian, Z. Zhu, … T.Z.-T. journal of, undefined 2018, Excess Cesium Iodide Induces Spinodal Decomposition of CsPbI2Br Perovskite Films, ACS Publications. (n.d.). https://pubs.acs.org/doi/abs/10.1021/acs.jpclett.8b03742 (accessed October 8, 2019).

[232] H. Zai, D. Zhang, L. Li, C. Zhu, S. Ma, Y. Zhao, Z. Zhao, C. Chen, H. Zhou, Y. Li, Q. Chen, Low-temperature-processed inorganic perovskite solar cells via solvent engineering with enhanced mass transport, Journal of Materials Chemistry A. 6 (2018) 23602–23609. doi:10.1039/C8TA09859J.

[233] S. Selberherr, S. Selberherr, The Physical Parameters, in: Analysis and Simulation of Semiconductor Devices, Springer Vienna, Vienna, 1984: pp. 80–126. doi:10.1007/978-3-7091-8752-4_4.

[234] S. Heo, G. Seo, Y. Lee, D. Lee, M. Seol, J. Lee, J.B. Park, K. Kim, D.J. Yun, Y.S. Kim, J.K. Shin, T.K. Ahn, M.K. Nazeeruddin, Deep level trapped defect analysis in CH3NH3PbI3 perovskite solar cells by deep level transient spectroscopy, Energy and Environmental Science. 10 (2017) 1128–1133. doi:10.1039/c7ee00303j.

[235] J.M. Ball, A. Petrozza, Defects in perovskite-halides and their effects in solar cells, Nature Energy. 1 (2016) 1–13. doi:10.1038/nenergy.2016.149.

[236] P. Boland, K. Lee, J. Dean, G. Namkoong, Design of organic tandem solar cells using low- and high-bandgap polymer:fullerene composites, Solar Energy Materials and Solar Cells. 94 (2010) 2170–2175. doi:10.1016/J.SOLMAT.2010.07.007.

[237] T. Minemoto, M. Murata, Device modeling of perovskite solar cells based on structural similarity with thin film inorganic semiconductor solar cells, Journal of Applied Physics. 116 (2014). doi:10.1063/1.4891982.

[238] J. Zhang, C. Yu, L. Wang, Y. Li, Y. Ren, K. Shum, Energy barrier at the N719-dye/CsSnI 3 interface for photogenerated holes in dye-sensitized solar cells, (2014). doi:10.1038/srep06954.

[239] L.Y. Huang, W.R.L. Lambrecht, Electronic band structure, phonons, and exciton binding energies of halide perovskites CsSnCl3, CsSnBr3, and CsSnI3, Physical Review B -

Condensed Matter and Materials Physics. 88 (2013) 1–12. doi:10.1103/PhysRevB.88.165203.

[240] S. Rühle, Tabulated values of the Shockley-Queisser limit for single junction solar cells, Solar Energy. 130 (2016) 139–147. doi:10.1016/j.solener.2016.02.015.

[241] S.A. Kulkarni, T. Baikie, P.P. Boix, N. Yantara, N. Mathews, S. Mhaisalkar, Band-gap tuning of lead halide perovskites using a sequential deposition process, Journal of Materials Chemistry A. 2 (2014) 9221–9225. doi:10.1039/c4ta00435c.

[242] S.Z. Haider, H. Anwar, Y. Jamil, M. Shahid, A comparative study of interface engineering with different hole transport materials for high-performance perovskite solar cells, Journal of Physics and Chemistry of Solids. 136 (2020) 109147. doi:10.1016/j.jpcs.2019.109147.

[243] P.W. Liang, C.Y. Liao, C.C. Chueh, F. Zuo, S.T. Williams, X.K. Xin, J. Lin, A.K.Y. Jen, Additive enhanced crystallization of solution-processed perovskite for highly efficient planar-heterojunction solar cells, Advanced Materials. 26 (2014) 3748–3754. doi:10.1002/adma.201400231.

[244] L. Li, Y. Chen, Z. Liu, Q. Chen, X. Wang, H. Zhou, The Additive Coordination Effect on Hybrids Perovskite Crystallization and High-Performance Solar Cell, Advanced Materials. 28 (2016) 9862–9868. doi:10.1002/adma.201603021.

[245] D. Bi, C. Yi, J. Luo, J.D. Décoppet, F. Zhang, S.M. Zakeeruddin, X. Li, A. Hagfeldt, M. Grätzel, Polymer-templated nucleation and crystal growth of perovskite films for solar cells with efficiency greater than 21%, Nature Energy. 1 (2016). doi:10.1038/nenergy.2016.142.

[246] M. Chen, M.-G. Ju, H.F. Garces, A.D. Carl, L.K. Ono, Z. Hawash, Y. Zhang, T. Shen, Y. Qi, R.L. Grimm, D. Pacifici, X.C. Zeng, Y. Zhou, N.P. Padture, Highly stable and efficient all-inorganic lead-free perovskite solar cells with native-oxide passivation, Nature Communications. 10 (2019) 16. doi:10.1038/s41467-018-07951-y.

[247] S.C. Lee, J.H. Lee, T.S. Oh, Y.H. Kim, Fabrication of tin oxide film by sol-gel method for photovoltaic solar cell system, Solar Energy Materials and Solar Cells. 75 (2003) 481–487. doi:10.1016/S0927-0248(02)00201-5.

[248] J. Wang, J. Zhang, Y. Zhou, H. Liu, Q. Xue, X. Li, C.C. Chueh, H.L. Yip, Z. Zhu, A.K.Y. Jen, Highly efficient all-inorganic perovskite solar cells with suppressed non-radiative recombination by a Lewis base, Nature Communications. 11 (2020) 1–9. doi:10.1038/s41467-019-13909-5.